DIRECT IMAGING OF SELF-ASSEMBLY BEHAVIORS OF COLLOIDS: FROM THE MICROSCALE PLATES TO THE NANOSCALE CUBES

BY

BINBIN LUO

DISSERTATION

Submitted in partial fulfillment of the requirements
for the degree of Doctor of Philosophy in Materials Science and Engineering
in the Graduate College of the
University of Illinois at Urbana-Champaign, 2020

Urbana, Illinois

Doctoral Committee:

Assistant Professor Qian Chen, Chair
Professor Paul V. Braun
Professor Jianjun Cheng
Professor Jian-Min Zuo
Professor Charles M. Schroeder

ABSTRACT

Microscale and nanoscale colloidal particle self-assembly is widely studied to establish the design rules towards ordered structures and used as atomic model systems for phase transition studies such as crystallization and growth. The well-established synthetic library enables the synthesis of colloidal particles with controllable size, morphology, and surface chemistry, which dictates their interactions for self-assembly. This dissertation focuses on studying a promising yet underexplored colloidal building block: anisometric colloids, and developing direct imaging tool of liquid-phase transmission electron microscopy (TEM) to visualize and quantify the less-explored nanoparticle self-assembly dynamics in solution. I begin by engineering highly directional interactions of micron-sized silver plates through colloidal synthesis and surface functionalization, to induce their co-assembly with patchy spheres into complex, 2D architectures. Utilizing a combination of direct optical microscopy imaging, theoretical modeling, and automated single particle tracking, I further demonstrate an unconventional crystallization pathway into 3D hierarchical lattices from polydisperse colloids. Then I focus on a foundationally new imaging tool known as liquid-phase TEM for in-situ imaging of otherwise inaccessible solution-phase nanoparticle self-assembly dynamics at nanometer resolution. I substantially advance this technique and reveal, for the first time, the nanoparticle assembly dynamics such as a layer-by-layer growth process into flat superlattices. This dissertation concludes by highlighting new opportunities from this technical improvement in navigating colloidal interactions to engineer the conformation, phase behaviors, and collective dynamics of colloids on the nanometer length scale. The generalized interaction engineering strategy from my research can serve as a general guideline for the design and fabrication of functional colloidal materials from the bottom-up.

ACKNOWLEDGEMENTS

The fulfillment of this dissertation would not be possible without the help and support from many people. First, I would like to acknowledge my Ph.D. advisor, Prof. Qian Chen, for her constant mentoring and help during my five-year Ph.D. study at UIUC. We worked together on designing the experiments, analysis of data, and preparation for publications. And most importantly, she taught me how to do independent research. I would also like to acknowledge Prof. Paul V. Braun, Prof. Jianjun Cheng, Prof. Jian-Min Zuo, Prof. Charles M. Schroeder for serving on my dissertation committee, and for always being supportive.

I was motivated for Ph.D. study when I was an undergraduate at University of Science and Technology of China (USTC), where I learned solid fundamental science in chemistry, physics, and mathematics. I especially thank Prof. Yujie Xiong, my undergraduate advisor, and Xueyu Zhao, my research mentor, and Dong Liu, Linfeng Yu, Jie Liu, Ailun Wang, a few of my best friends, for their guidance and encouragement in my undergraduate research. I would like to thank my collaborators in my Ph.D. research, especially Zihao Ou, Johnny W. Smith, Ahyoung Kim, Zixuan Wu, Chang Qian, Dr. Xiaohui Song, Ziwei Wang and Prof. Erik Luijten at Northwestern University, Kristin M Hutchins and Prof. Jeffrey S Moore. I have been learning so much and getting a lot of help from you. Many thanks to other Chen group members, Dr. Wenxiang Chen, Dr. Hyosung An, Dr. Shan Zhou, Cong Xu, Chang Liu, Lehan Yao, Junli Wu, Yuxiao Wu. It is always enjoyable to discuss my research with you. Special thanks to my friends at UIUC, especially Prof. Juyeong Kim, Yingfeng Yang, Yonghui Ma, Yiming Liu, Yiliang Wang, Derek Shin, Zixuan Wei, Songsong Li, Suoang Lu, Zhiyuan Han, and Ruixuan Zhou. And great thanks to all my teachers again!

Lastly, I would like to sincerely thank my parents, Ying Luo and Xiaoying Gong, my brother Lulu Luo, my sister Zixuan Luo, my girlfriend Zitong Song, and my other family members, for their endless love and support!

Dedicated to my parents, Ying Luo and Xiaoying Gong,

for their endless love and support.

TABLE OF CONTENTS

CHAPTER 1: INTRODUCTION

Self-assembly is the process by which individual building units arrange themselves into ordered structures.[1-5] Colloidal particles (micron-sized, nano-sized) can self-assemble into numerous superlattice structures and phases,[2, 4] a process typically driven by weak interparticle interactions (e.g., van der Waals, electrostatic, depletion, DNA hybridization, hydrogen bonding, hard-core interaction), or under external electric/magnetic fields.[2, 4-7] These Brownian objects can be prepared with excellent monodispersity and have a wide variety of sizes, shapes and compositions,[8, 9] through solution oxidation and reduction synthesis (e.g., Nobel metals), thermal decomposition (e.g., iron oxides), polymerization reactions (e.g., SiO_2, polystyrene), photolithography (SU-8),[10] etc. Their surfaces are usually coated with surface ligands either in synthesis or post-modification, and they can be dispersed in solvents (aqueous or organic). Typical surface ligands include hexadecyltrimethylammonium bromide (CTAB), citric acid, oleic acid, small-molecule thiols, polymers, etc.[4] In general, colloidal building blocks can be divided into two types defined by their sizes, micron-sized colloids and nanoparticles (NPs). For decades, one of the overarching objectives of self-assembly science has been to define the rules necessary to build functional, artificial materials with rich and adaptive phase behavior from the bottom-up. To this end, the computational and experimental efforts of chemists, physicists, materials scientists, and biologists alike have built a body of knowledge that spans both disciplines and length scales. Indeed, today control of self-assembly is extending even to supramolecular and molecular levels,[11] where crystal engineering and design of porous materials are becoming exciting areas of exploration.

Self-Assembly Using Micron-Sized Colloids. Micron-sized colloids can be viewed as large atoms. Their assembly behaviors can be imaged and tracked by optical microscopy, and hence they are excellent model systems for phase transition studies, such as crystallization, melting, and solid-solid transitions.[2] Phase transitions are ubiquitous in nature, and they play very important roles in determining materials' properties and related applications. Studying colloidal self-assembly at the microscale can provide very useful information for phase transitions. The micron-sized colloids can be made isotropic, to mimic isotropic atoms. They can also be made anisotropic, to introduce anisotropic interactions or directional bonding between them. Over the past two decades, colloidal assembly model systems have provided a lot of insights in understanding phase transitions, as well as generating ordered architectures.

NP Self-Assembly Studies. Moving to the nanoparticle self-assembly, however, there are many stones yet to be turned. While recent breakthroughs in NP synthesis have amassed a vast library of nanoscale building blocks, NP-NP interactions *in situ* remain poorly quantified, in large part due to technical and theoretical impediments. While increasingly many applications for self-assembled architectures are being demonstrated, it remains difficult to predict the pathways by which these structures form. Liquid-phase transmission electron microscopy (TEM) has the unique ability to resolve the motions and trajectories of single nanoparticles (NPs) in solution. This capability has made it a powerful addition to the arsenal of methods used to probe nanoscale self-assembly behavior. For example, while small-angle X-ray scattering (SAXS) can be used to resolve nanoscale structural evolution,[12, 13] it can only do so on the ensemble level. Conventional TEM and cryogenic EM have single NP resolution, but are limited to imaging dried or flash-frozen samples; continuous self-assembly dynamics cannot be elucidated directly.[14, 15] Even simulations can find challenges: it is computationally taxing to incorporate the large number of particles necessary to probe assembly processes,[16] and interaction potentials used in simulations are often derived from micron-scale colloidal behavior, which does not merely rescale to the nano-regime.[11] The paucity of experimental data on nanoscale dynamics complicates the validation of these models. With these and other motivations, since 2012, liquid-phase TEM has already been used to investigate self-assembly dynamics in a variety of systems, chiefly of spherical metallic NPs.[17-22] Recent studies start to work with anisotropic NPs, which have very different self-assembly behaviors.

Anisotropic NPs have intrinsically different self-assembly properties, largely because their interactions are highly directional.[1, 23] A quantitative approach to describing their dynamics, meanwhile, offers deeper insight into the nanoscale interactions governing assembly, and into how the kinetic pathways taken to a final structure can be manipulated. For example, can we control a kinetic pathway to bias one product among many possibilities? Can we map out the complete self-assembly free energy landscape, much like extensive efforts in protein folding? Understanding these dynamics "rules" will be a critical prerequisite to manipulating self-assembly of active soft matter, where building blocks are not static, but self-propelled and evolving.[24-28]

The Role of Anisotropy in Liquid-Phase NP Self-Assembly. Metallic NPs (PtFe,[20] Pt,[17, 29] Au,[18, 19, 21, 22, 30, 31] etc.) have been a practical starting point for liquid-phase TEM studies of self-assembly. For one, they exhibit high contrast against a liquid background, which makes it possible to achieve nanometer to atomic resolution.[32] Most metallic NPs are also highly stable under prolonged electron beam exposure, which is required to capture continuous assembly dynamics. In particular, although NPs have diffusion coefficients in bulk water on the order of 10^6 – 10^8 nm^2/s (per the Stokes-Einstein relation, for NPs between 100 and a few nanometers in size), NP motions in liquid-phase TEM chambers can be three to six orders of magnitude slower, likely because of an increase in solvent viscosity during imaging or the involvement of NP-substrate attractions.[19, 33, 34] While these effects bring the time scale of NP motions up to the temporal resolution of conventional liquid-phase TEM instrumentation, when coupled with the fact that self-assembly requires millions of collisions to occur within a concentrated NP suspension, the consequence is that self-assembly time scales range from minutes to hours. During time spans of this length, NPs otherwise susceptible to sustained electron beam exposure can restructure or decompose, depending on the beam dose.

Most of the aforementioned studies have investigated the self-assembly of spherical metallic NPs, since high quality, monodisperse samples are typically easy to make. Anisotropic NPs, on the other hand, require more sophisticated synthesis methods,[4, 35] and their self-assembly has only recently been investigated under liquid-phase TEM. These NPs are distinguished from spheres by their intrinsically directional interactions, either because of their shape and symmetry,[1, 23, 36] or because of their heterogeneous surface ligand coverage[37] arising from the different binding energies[38] and curvatures[39] across a NP's surface. These directional interactions have the potential to mimic the surface heterogeneity of biomolecules, a feature which, in nature, leads to assemblies with novel symmetries, hierarchies, and multiplex functions.[40]

The representative NP building blocks and structures observed in liquid-phase TEM self-assembly are summarized in **Figure 1.1**. Closely packed structures of spherical NPs typically form when the electron beam agitates and gradually evaporates the solvent, whereupon convection sweeps NPs together.[17, 29] Loosely packed, one-dimensional (1D) chains,[18, 21, 22] which rarely result from solvent-drying, are formed when the solvent is preserved throughout self-assembly and when, consequently, liquid-mediated NP-NP interactions serve as the major driving force for assembly. The directionality of liquid-mediated NP-NP interactions is highly dependent on NP shape. For example, when Sutter *et al*. used liquid-phase TEM to study the assembly of CdSe/CdS octapods (**Figure 1.1**), they observed that these particles assembled into chains, much like assemblies of spherical NPs in liquid.[41] However, the anisotropy of the octapods restricts the number and orientation of attachments which are involved in chain formation; the branching of octapods leads to a “pod-to-pod” particle connection, which can only occur in specific orientations.

For NPs which have interactions of more pronounced directionality such as Au nanoprisms, these NPs experience a van der Waals attraction in the face-to-face orientation which is hundreds of times larger than in the side-by-side configuration.[30] This directionality promotes assembly into 1D lamellar superlattices in a liquid environment (**Figure 1.1**), with a characteristic lattice constant (*i.e*. the center-to-center spacing between adjacent prisms) determined by a balance between van der Waals attraction and electrostatic repulsion between charged ligand coatings. The assemblies of Au nanorods observed in liquid-phase TEM, which are otherwise not seen directly, are less expected.[31] In solvent evaporation-driven self-assembly, Au nanorods often assemble side-by-side into bundles when concentrated by drying.[42] In liquid, however, Au nanorods diffuse freely throughout the assembly process, whereby they sample the assembly free-energy landscape with statistics governed by rod-rod interactions.[31, 43] Nanorods coated with charged ligands eventually assemble tip-to-tip (**Figure 1.1**), a configuration relevant for plasmonic coupling of the electromagnetic fields concentrated at individual rod tips. This tip-selective attachment was attributed to the non-uniform rod shape and, consequently, different interaction microenvironments associated with different modes of approach. In particular, given the appropriate liquid conditions, two nanorods approaching side-by-side experience a stronger electrostatic repulsion than those nearing tip-to-tip, since the highly curved tip surface has a lower density of charges. Rods orient to minimize the repulsions encountered as they approach one another, whereupon short-range van der Waals attraction “locks” them into 1D chains.

In general, shape anisotropy strongly impacts the directionality of NP-NP interactions in solution and, as such, is a powerful tool for engineering new architectures and new self-assembly dynamics. Moreover, systematic studies on diverse anisotropic shapes will provide insight not just into NP self-assembly, but also into addressing fundamental questions in other fields, such as historic geometric puzzles concerning 3D anisotropy and space tessellation.[44] For example, tetrahedral particles have been shown in computer simulations to pack into exotic 3D structures, including chiral chains and quasi-crystals.[45] It will be intriguing to image such symmetry-breaking processes from the bottom-up in real-time.

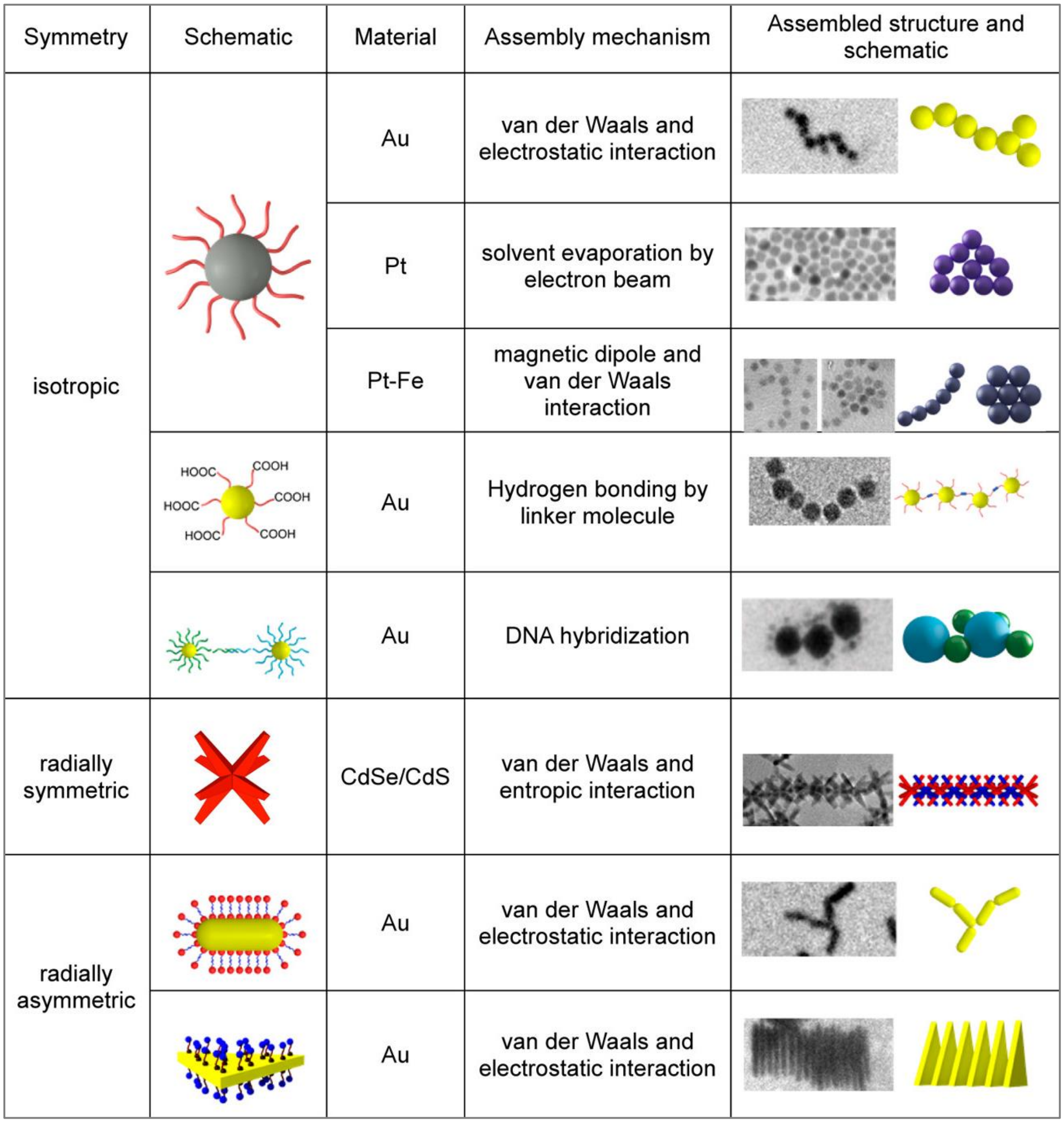

Symmetry	Schematic	Material	Assembly mechanism	Assembled structure and schematic
isotropic		Au	van der Waals and electrostatic interaction	
		Pt	solvent evaporation by electron beam	
		Pt-Fe	magnetic dipole and van der Waals interaction	
		Au	Hydrogen bonding by linker molecule	
		Au	DNA hybridization	
radially symmetric		CdSe/CdS	van der Waals and entropic interaction	
radially asymmetric		Au	van der Waals and electrostatic interaction	
		Au	van der Waals and electrostatic interaction	

Figure 1.1. Overview of building blocks and structures observed in liquid-phase TEM self-assembly studies. Most work has considered spherical metallic NPs (Au, Pt, PtFe), while anisotropic particles have only recently been studied. (Reprinted with permission from [5]. Copyright © 2017, American Chemical Society.)

Scope of This Work

Colloidal Particle Synthesis and Surface Modification. To obtain the colloidal particle building blocks, I followed the existing literature with slight modifications to synthesize the colloidal particles in solution.[46, 47] By adjusting the type and amount of precursor and reducing agents, capping agents, growth time and speed, and surface modification, these colloidal particles have excellent tunability in their shape (concave and convex polyhedra), size (a few nanometers to a few micrometers), composition (metal, oxides, semiconductors), and surface chemistry (carboxylate-thiols,[30] block copolymers[48]), which determine their interactions and dynamic assembly behaviors in solution.[4, 6] The carboxylate-thiols and polymers on the colloidal particle surface introduce electrostatic repulsion and/or steric repulsion between colloids, stabilizing those colloids and minimizing aggregations in solution. After synthesis, those colloidal particles are characterized by UV-Vis spectrophotometer, zeta-sizer, scanning electron microscopy (SEM), and TEM to obtain the shape, size, and surface charge information of the colloidal particles.

Optical/Electron Microscopy Imaging. State-of-the-art *in situ* characterization techniques, mainly optical microscopy[2] and liquid-phase TEM,[5] are used in my investigations. Optical microscopy provides a general platform for micro-scale dynamics studies. The combination of micro-scale colloids and optical microscopy imaging has already demonstrated great success in understanding phase transition behaviors such as crystallization, melting, glass transition, gelation, etc.[2] Moving to the nanoscale, this “seeing is believing” principle is not convenient. TEM is the typical instrument to characterize the nano-sized objects, which requires a high vacuum operation condition. This high vacuum condition is incompatible with the liquid sample. As a result, the nanoscale dynamics in solution has been missing for a long time. To solve this problem, I used a foundationally new imaging tool known as liquid-phase TEM (**Figure 1.2**). This technique has the long-anticipated merit of extending phenomenological studies down to nanometer and even atomic scales, where dynamics is even richer yet less explored. To avoid exposure of the liquid sample in the high vacuum, the liquid sample is sandwiched in between two membranes. The membranes need to be strong enough to hold the liquid under the high vacuum, preventing its evaporation. At the same time, they need to be thin enough to be electron transparent. The most-commonly used membranes are the graphene and silicon nitride.[49] In addition to imaging static liquid sample, this technique also allows us to apply electrical bias, change temperature, flow liquid during imaging at nanometer and millisecond resolutions. The experimentally measured interaction and dynamics can serve as input parameters for simulation and further predict new assembly structures and new reconfigurable nanomaterials.

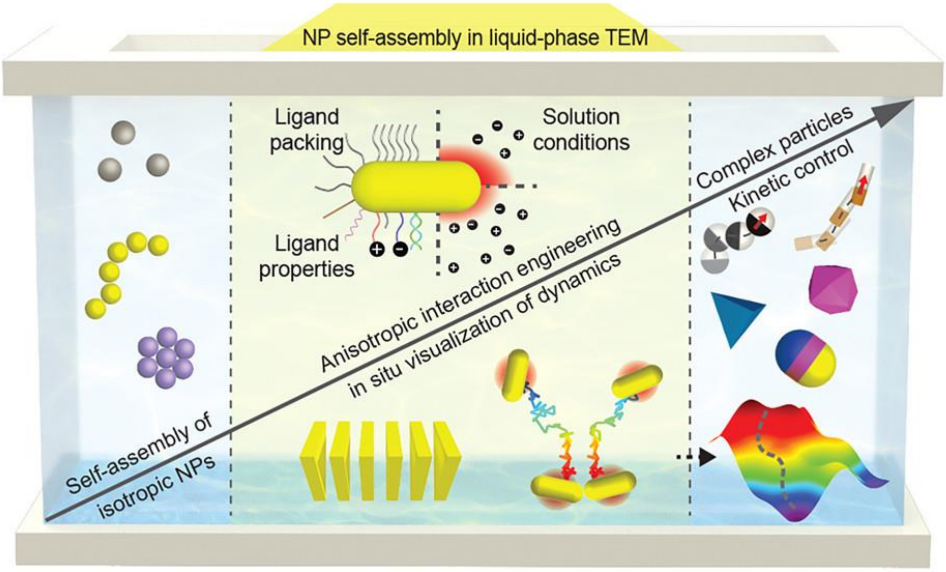

Figure 1.2. NP self-assembly in Liquid-phase TEM. (Reprinted with permission from [5]. Copyright © 2017, American Chemical Society.)

Interaction Modeling and Quantitative Analysis. To understand the colloidal interactions quantitatively, interaction modeling is conducted using both the analytical form and the coarse-grained model.[50] The interaction includes van der Waals attraction, electrostatic repulsion/attraction, depletion attraction, steric repulsion, etc. To convert the images/movies obtained from direct imaging into quantitative numbers, we track the colloidal particles in the movies and then quantify their motions/dynamics to extract the physical rules governing their phase behaviors.

Colloidal Co-Assembly Inspired by Polymer Chemistry.[51] A major goal in self-assembly research is to emulate nature's singular control over the shape, size, and chemistry of building blocks, so that diverse artificial structures can be designed from the bottom-up.[52-55] The field has come tremendously far in achieving this goal, but not all of biology's tricks involve convoluted chemistry or delicately balanced interactions. In **Chapter 2**, I present our findings that another of life's less-explored but equally robust self-assembly strategies—namely, using anisometric nanoparticles—can also confer many advantageous self-assembly capabilities. In particular, we show that highly anisometric silver nanoplates can be employed to "polymerize" a wide variety of highly adaptive structures, from one-dimensional chains with tunable stiffness to flexible two-dimensional pores that contract on command. More broadly, by using molecular polymerization-based design principles, we show that particles with tunable functionality (in this case, bifunctional anisometric nanoplates with monofunctional "chain-stopping" or multifunctional "branching" patchy spheres) together create non-conventional adaptive assemblies with controllable structure. The connection we made between dynamic nanoparticle assemblies and polymerization can serve as a general guideline for future bottom-up design of nanomaterials with readily tunable morphology and physical properties, or perhaps as the basis for controlled, synthetic analogues to one- and two-dimensional structures found in nature.

Order from Polydisperse Microscale Plates.[50] Colloids are generally divided into two types defined by their sizes: micron-scale colloids serving as optically accessible analogs to atomic phase transitions,[2] and nanoparticles as structural and functional modules for their quantum-confined properties.[4] In **Chapter 3**, I focus on the promising yet largely underexplored third type, anisometric colloids which integrate micrometer and nanometer dimensions into the same particle. In the context of colloidal assembly, this integration introduces the following novel behaviors in our prototypical anisometric plate system, all of which are not accessible to micron- or nanoscale colloids: 1) Spontaneous assembly into three-dimensional (3D) structures without the need for particle–solvent density matching typically required for micron-sized colloids. The nanoscale thickness enables free particle movements in 3D against gravity, while the micron-scale basal plane enables direct imaging for understanding. 2) Monodisperse secondary building blocks (meta-rods) assembled from polydisperse anisometric plates following a novel size-focusing effect due to plate rotation and consequent orientational disorder. 3) The monodisperse meta-rods further order into 3D hierarchical lattices. The final symmetry hinges on the effective shape of meta-rods, where different polymorphs can be triggered to interconvert. Combining optical microscopy imaging and theoretical modeling, we elucidate the above observations as an intricate balance utilizing advantages of micron-scale (visibility under optical microscopy, strong directional attraction, etc.) and nanoscale (large fluctuation height, sensitivity to tip truncation, etc.) dimensions. Our approach and conceptual framework shown here can aid designing a rich family of unexplored assembly structures and functions from synthetic or biological anisometric building blocks. The 3D lattice we attained in this specific system can be further exploited for non-equilibrium field-driven assembly with architecture-dependent property coupling in the nanoscale dimension, towards complex, hybrid colloidal materials.

Direct Imaging of Layer-By-Layer Growth in Nanoparticle Lattices. In **Chapter 4**, I focus on the problem of crystallization on the nanoscale. In atomic systems, one of the most important crystallization pathways is so-called layer-by-layer growth (highly desirable for, e.g., producing flat films).[56-60] Yet, even though micron-sized colloidal suspensions have been such a successful atomic model in other ways,[2] these systems have failed to exhibit the growth modes surmised to exist on the atomic scale. In our new experimental–computational work, we have been able to image the crystallization pathways of nanoparticle superlattices. The key enabling aspect is real-time and real-space imaging with single-particle resolution, made possible by pushing the limits of liquid-phase TEM through various innovations. For nanoparticles of various symmetries and shapes (cubes, concave polyhedral particles, spheres) we demonstrate, for the first time, that crystallization occurs through layer-by-layer growth. The implications of this are multiple. It is now possible to examine nanoscale crystallization pathways directly. Combining liquid-phase TEM, single-particle tracking, and simulations, we quantify and interpret crucial energetic and kinetic details that are responsible for the important and universal layer-by-layer growth mode. This provides mechanistic understanding essential for numerous applications, such as the surface engineering of nanoparticle superlattices. At the same time, the system studied can serve as a model that yields microscopic information relevant for atomic systems. Lastly, our work offers a paradigm shift in the study of nanoscale phase behaviors in biological and synthetic systems, where the interactions and energetics are fundamentally different from those of the prevalent micron-scale model systems.

Notes to Chapter 1

Part of this chapter is adapted with permission from the paper “Luo, B., Smith, J.W., Ou, Z. & Chen, Q. Quantifying the self-assembly behavior of anisotropic nanoparticles using liquid-phase transmission electron microscopy. *Acc. Chem. Res.* **50**, 1125-1133 (2017)”,[5] Copyright © 2017, American Chemical Society, and from the paper “Luo, B. et al. Polymerization-like co-assembly of silver nanoplates and patchy spheres. *ACS Nano* **11**, 7626-7633 (2017)”,[51] Copyright © 2017, American Chemical Society, and from the paper “Luo, B. et al. Hierarchical self-assembly of 3D lattices from polydisperse anisometric colloids. *Nat. Commun.* **10**, 1815 (2019)”,[50] Copyright © 2019, Springer Nature, and from the paper “Universal layer-by-layer growth mode in nanoparticle superlattices”, to be submitted.

CHAPTER 2: POLYMERIZATION-LIKE CO-ASSEMBLY OF SILVER NANOPLATES AND PATCHY SPHERES

Abstract

Highly anisometric nanoparticles have distinctive mechanical, electrical, and thermal properties and are therefore appealing candidates for use as self-assembly building blocks. Here we demonstrate that ultra-anisometric nanoplates, which have a nanoscale thickness but a micrometer-scale edge length, offer many materials design capabilities. In particular, we show that these nanoplates "copolymerize" in a predictable way with patchy spheres into one- and two-dimensional structures with tunable architectural properties. We find that, on the pathway to these structures, nanoplates assemble into chains following the kinetics of molecular step-growth polymerization. In the same mechanistic framework, patchy spheres (Janus and triblock particles) control the size distribution and morphology of assembled structures, by behaving as monofunctional chain stoppers or multifunctional branch points during nanoplate polymerization. In addition, both the lattice constant and the stiffness of the nanoplate assemblies can be manipulated after assembly. We see highly anisometric nanoplates as one representative of a broader class of dual length-scale nanoparticles, with the potential to enrich the library of structures and properties available to the nanoparticle self-assembly toolbox.

Introduction

Biological systems often employ nanoscale building blocks with strictly controlled chemistry or intricate surface patterning to engineer self-assembled structures with unique properties and adaptive functional behavior from the bottom-up.[52-55] However, not all of the tricks up nature's sleeve hinge on such sophisticated strategies; there are sometimes far simpler ways in which living systems will exploit features of a self-assembly building block to “build in” a particular set of desired properties. One such feature is anisometry. Consider, for example, the fibrous protein collagen. The staggered arrangement of highly anisometric tropocollagen units within this protein ultimately allows collagen to undergo multiple modes of tensile deformation and thereby exhibit exceptional elastic energy absorption.[61, 62] Even though many individual tropocollagen units are required to form this functional staggered array, by choosing a highly anisometric building block (*i.e.* one that is both very thin and very long), collagen can do so without completely compromising bending flexibility in the final structure. Similarly remarkable properties enabled by anisometry can be found in synthetic nanofiber assemblies as well; in carbon nanotube[63-66] and ultrathin metal nanowire[66-69] systems, a high degree of anisometry engenders not just superlative mechanical behavior, but also remarkable electrical and optical properties in assembled structures.

Here we present materials engineering capabilities offered by anisometry in a different but similarly intriguing context: the self-assembly of ultra-anisometric silver nanoplates. For example, as is the case for nanoparticle systems in general, these nanoplates have one dimension which is comparable to the range of interparticle interactions[6, 7] (for example, a typical thickness of ~30 nm). Thus, a balance between van der Waals attraction and electrostatic repulsion leads to assembly with “loose” packing[30] (**Figures 2.1 and 2.2**). Such loose packing allows one to tune properties like the size and lattice constant of assembled structures—which are parameters relevant to plasmonic coupling applications[13, 70-72]—simply by adjusting the ionic strength of the surrounding solution. At the same time, these anisometric nanoplates have a micrometer-scale edge length. This characteristic facilitates imaging the nanoplate self-assembly trajectory not only *in situ* and starting from the level of single nanoparticles, but also in a straightforward way: using optical microscopy. Typically, imaging the solution-phase self-assembly dynamics of nanoparticles which are nanoscopic in all dimensions is not as simple.[30, 31] We take advantage of the real-time particle trajectories resolved by optical microscopy to show that nanoplates assemble *via* a mechanism fundamentally analogous to molecular step-growth polymerization,[73] and also to quantify how ionic strength tunes chain stiffness and fluctuation dynamics.[74-79] The micrometer-scale dimension of the nanoplates also enables controlled “copolymerization” with micrometer-sized patchy spheres.[80, 81] With respect to nanoplates, these patchy colloids have a functionality (*i.e.* number of “binding” sites) dictated by the solution ionic strength (**Figure 2.2**) and therefore behave as monofunctional “stoppers” or multifunctional “linkers” in nanoplate polymerization. This additional degree of control over interparticle interactions grants access to more diverse bonding motifs and a wide variety of open structures beyond simple one-dimensional (1D) chains. Reconfigurable assemblies which are formed include flexible pores that contract on command, potentially relevant to caging or filtration applications,[82-85] and other two-dimensional (2D) networks with many possible connectivities.

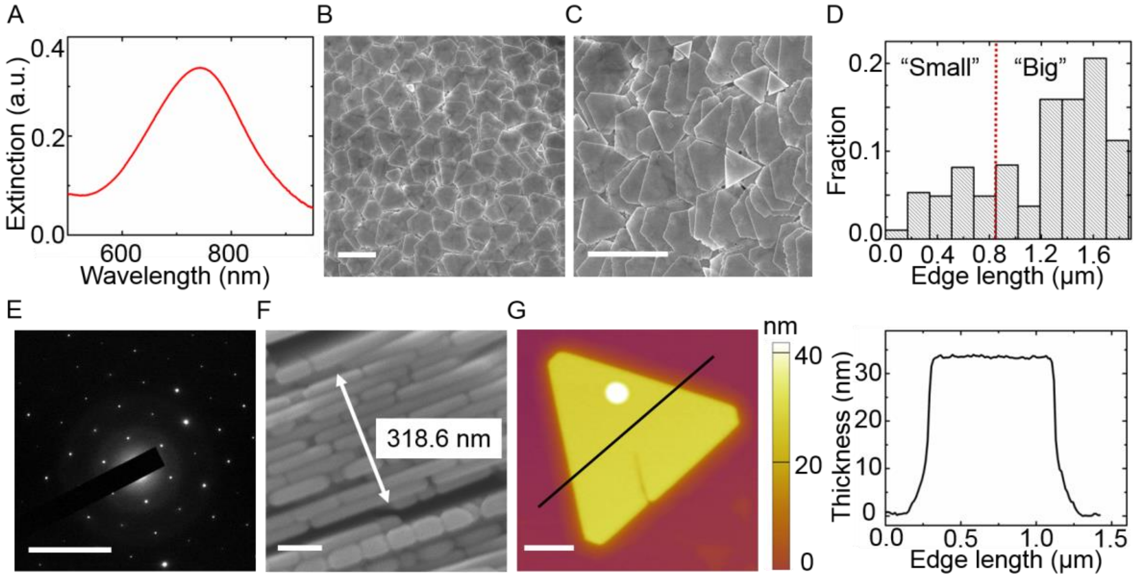

Figure 2.1. Characterization of silver nanoplates (edge length: 1.44 ± 0.26 μm, considering only the big assembling nanoplates). (A) A typical UV–vis spectrum measured from a solution of as-synthesized silver seeds. (B) Low- and (C) high-magnification SEM images of silver nanoplates. (D) The size distribution of silver nanoplates measured from SEM images using ImageJ. Here we set nanoplates with edge length smaller than 60% of the big nanoplates as small nanoplates (edge length smaller than 0.85 μm, see the dotted red line). As such, the small nanoplates have a size distribution of 0.51 ± 0.20 μm (namely 22% to 49% the size of the big nanoplates). The fraction of small nanoplates is about 32% compared with big nanoplates. (E) The SAED pattern of a representative silver nanoplate indicates that they are single crystalline. (F) The nanoplate thickness measured from an SEM image of standing stacked silver nanoplates. The measured thickness is 29 ± 4 nm, based on thickness measurements of 11 nanoplates in this image. This thickness value was used for interaction calculations. (G) AFM image (left) and (right) the corresponding thickness profile (across the black line in the left-hand image) of a representative silver nanoplate. Scale bars are: 2 μm in (B) and (C), 10 nm^{-1} in (E), 100 nm in (F), 300 nm in (G). (Reprinted with permission from [51]. Copyright © 2017, American Chemical Society.)

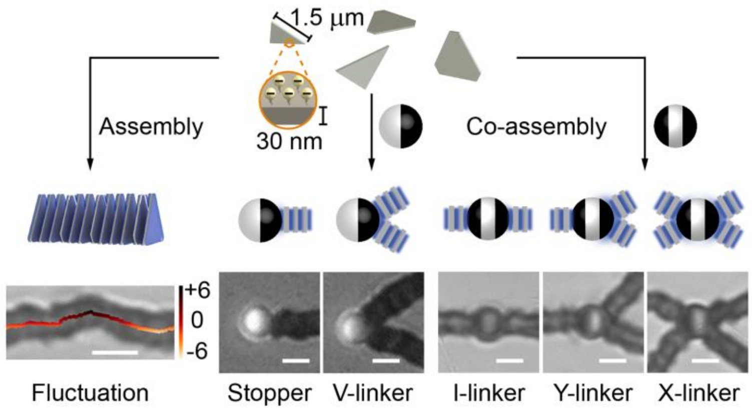

Figure 2.2. The self-assembly of anisometric silver nanoplates and their co-assembly with patchy spheres. (Top) Well-dispersed nanoplates and a zoomed-in view showing typical nanoplate dimensions and the negatively charged carboxylate-thiol surface ligands (not to scale). (Bottom) Left: A schematic and an optical microscopy image of a fluctuating 1D chain assembled from nanoplates. The skeleton overlaid with the optical microscopy image is color-coded according to the extent of transverse displacement. The unit of the color bar is the pixel size (1/58.04 nm). Right: Schematics and optical microscopy images of chain bond motifs with Janus and triblock particles. The blue shading highlights the area of net attraction. Scale bars: 2 µm. (Reprinted with permission from [51]. Copyright © 2017, American Chemical Society.)

Results and Discussion

We began by studying the self-assembly behavior of ultra-anisometric silver nanoplates. To obtain these self-assembly building blocks, we adopted a modified seeded-growth nanoparticle synthesis method.[47] In particular, while preparing the silver seeds, we used an excess of citrate ligands, rather than the usual poly(vinylpyrrolidone) ligands, to stabilize the seeds without the risk of aggregation due to polymer bridging.[6] In addition, after growing the seeds into nanoplates of a desired edge length (for example, ~1.5 µm for this self-assembly study, but nanoplates from 1 to 2.5 µm can be synthesized by varying the growth conditions, see **Figure 2.3 and Table 2.1**), we exchanged the citrate ligands with carboxylate-thiols,[86] which bind more strongly to silver atoms. These thiol ligands fully deprotonate in aqueous solution at pH = 7 (**Figure 2.4**), so nanoplates have a negative surface charge (zeta potential $\zeta = -41.9 \pm 6.8$ mV in deionized water) that stabilizes them in solution. Selected area electron diffraction (SAED) patterns and atomic force microscopy (AFM) measurements confirm that the nanoplates synthesized are single crystalline and have smooth surfaces (**Figure 2.1**).

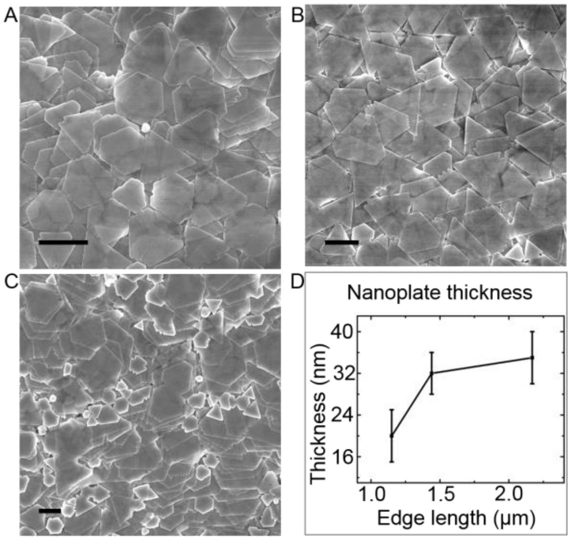

Figure 2.3. SEM images and thickness of silver nanoplates of different edge lengths. (A)–(C): SEM images of silver nanoplates of different edge lengths. (A) Edge length: 1.09 ± 0.14 μm, (B) 1.46 ± 0.22 μm and (C) 2.17 ± 0.33 μm. The edge length measurement does not include the much smaller particles in the system, as these very small particles are typically not involved in assembly. Scale bars: 1 μm. (D) Thickness of silver nanoplates of different edge lengths measured by AFM. The error bars shown in (D) are determined from averaging different particles in the same batch. (Reprinted with permission from [51]. Copyright © 2017, American Chemical Society.)

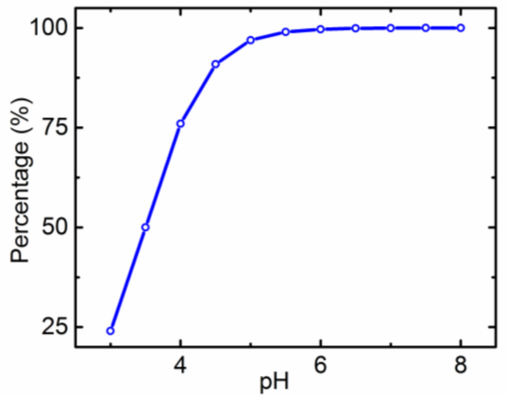

Figure 2.4. Calculated percentage of deprotonated carboxylate–thiol ligands on the silver nanoplate surface as a function of pH. A value of 3.5 was used for the pK_a of carboxylate–thiol ligands, based on information from the manufacturer. (Reprinted with permission from [51]. Copyright © 2017, American Chemical Society.)

Table 2.1. Synthesis conditions of silver nanoplates with different edge lengths.

Peak position of the seed solution (nm)	Peak intensity of the seed solution after dilution	Injection rate and time in each growth cycle	Shaking speed in growth cycle (rpm)	Growth cycle	Large nanoplate edge length (μm)
705	0.012	0.4 mL/min, 5 min	300	Cycle 4	1.15 ± 0.14
				Cycle 5	1.44 ± 0.26
731	0.012	0.4 mL/min, 5 min	600	Cycle 3	1.09 ± 0.14
749	0.012	0.2 mL/min, 10 min	1000*	Cycle 4	1.46 ± 0.22
				Cycle 5	2.17 ± 0.33

*During the first cycle, a shaking speed of 700 rpm was used to prevent large-volume seed solution spilling out from the glass vial due to high-speed shaking.

Nanoplates behave as bifunctional monomers and "polymerize" into 1D chains upon the addition of sodium chloride (**Figure 2.5**), which screens the electrostatic repulsion between nanoplates and therefore allows them to approach within the range of van der Waals attraction. The attraction strength is proportional to the nanoplate surface area involved in assembly and, therefore, predominantly favors the face-to-face assembly of nanoplates. In this way, a nanoplate effectively has two “binding” sites, or a functionality $f = 2$. After ~12 hours of growth, some chains grew up to 100 μm (**Figure 2.6**). The fact that individual nanoplates have large planar surfaces means that, while nanoplates within a chain can fluctuate transversely by sliding past one another, chains are unable to bend, in the sense that it is sterically difficult for neighboring nanoplates to deviate significantly from a parallel alignment. As such, these long chains behave like hard Onsager rods[87] (**Figure 2.6** and Fourier transform inset in **Figure 2.5**) that, when concentrated, orient into a nematic phase to maximize chain translational entropy. At a relatively low ionic strength, these long chains do not attach with each other laterally (for example, see the distance between individual long chains in **Figure 2.5**), indicating a weak interchain attraction in the lateral direction. The face-to-face assembly of nanoplates into chains is also reversible; a decrease in solution ionic strength leads to the disassembly of chains into individual nanoplates.

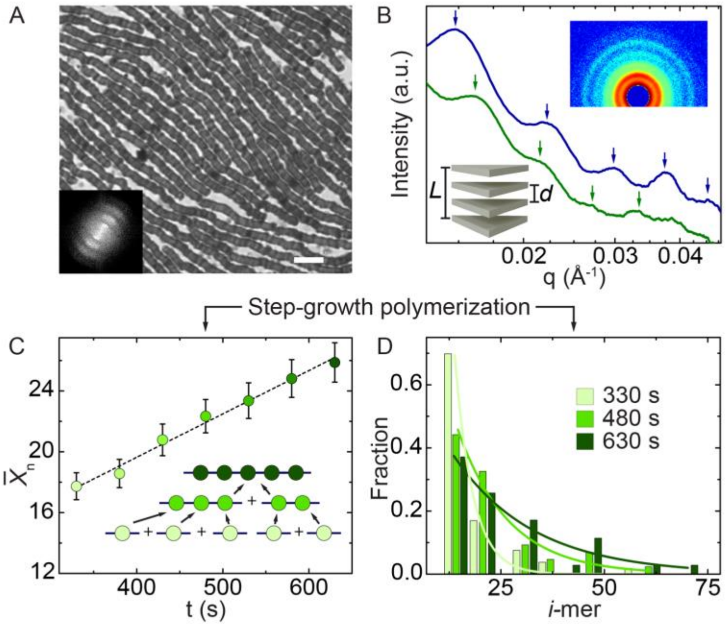

Figure 2.5. The assembly of 1D chains follows step-growth "polymerization". (A) An optical microscopy image of 1D chains assembled from concentrated nanoplates (edge length of the large nanoplate population: 1.44 ± 0.26 μm, thickness: 29 ± 4 nm). Ionic strength: 1.4 mM. The inset is a 2D Fourier transform of the same image indicating nematic phase-like alignment. Scale bar: 5 μm. (B) Small-angle X-ray scattering (SAXS) spectra of the chains in 1.4 mM (green) and 3.0 mM (blue) ionic strength conditions, with arrows indicating peak positions. Right inset: a representative 2D scattering image from SAXS. Left inset: a schematic of an assembled chain with center-to-center spacing d and chain length L labeled (not to scale). (C) The number-average degree of polymerization $\bar{X}_{\mathrm{n}}$ as a function of time t. The error bars are from measurement errors. A linear fit (black dotted line) has a coefficient of determination equal to 0.99. The inset is a schematic of step-growth polymerization. (D) The distribution of i-mers (*i.e.* chains containing i nanoplates) at different stages of chain growth follows a Flory–Schulz distribution. Each data point is binned over a range of i-mers, with a bin size of ~8.6. Fits to this distribution at different times are indicated by the colored curves. (Reprinted with permission from [51]. Copyright © 2017, American Chemical Society.)

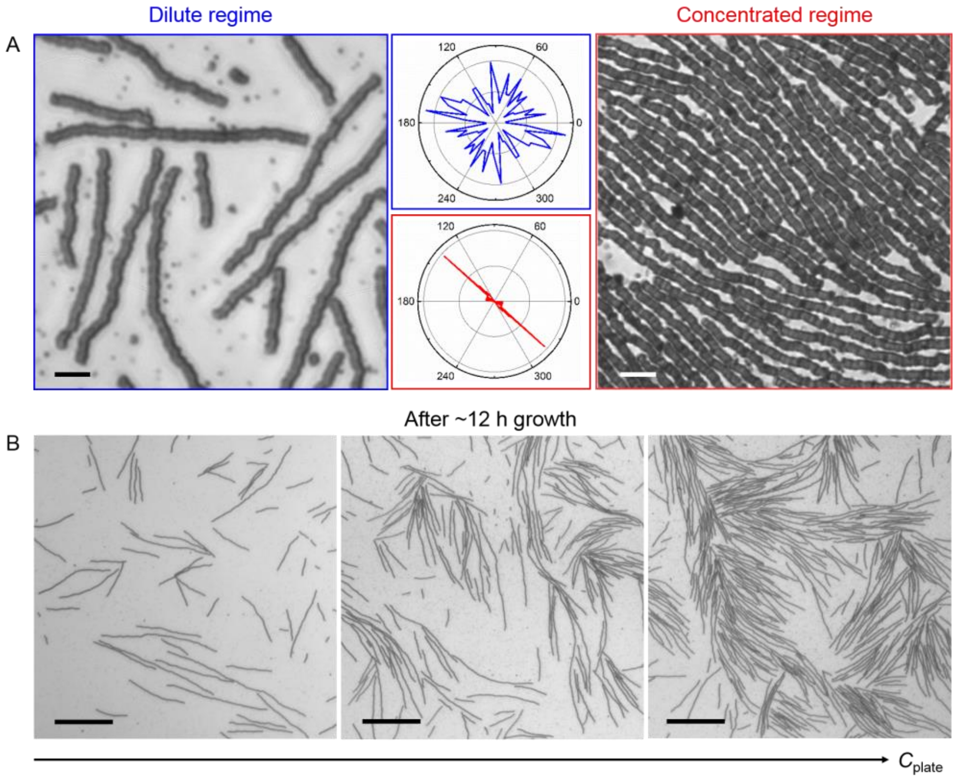

Figure 2.6. Optical microscopy images of chains self-assembled in solutions with different nanoplate concentrations and corresponding 2D radial order distribution plots.[88, 89] (A) Typical optical microscopy images of chains assembled from a solution with a low (far left) and a high (far right) concentration of silver nanoplates and (center) the corresponding 2D chain orientation distribution plots (The blue curve corresponds to the dilute regime and red curve corresponds to the concentrated regime. Units are in degrees). The 2D radial order distribution plots are based on assigning vectors to the colloidal chains. For the dilute radial order distribution plot, four images at the similar region were used together to obtain enough statistics. (B) Chains grow to more than 100 μm after ~12 h growth at different nanoplate concentration regimes. Ionic strength: 1.4 mM. Scale bars: 5 μm in (A) and 50 μm in (B). (Reprinted with permission from [51]. Copyright © 2017, American Chemical Society.)

The assembly of nanoplates into chains, markedly, proceeds by a mechanism characteristic of molecular step-growth polymerization. As shown in **Figure 2.7**, chains grow either by "monomer" addition or by the fusion of existing chains. In addition, we measured the number-average degree of polymerization $\bar{X}_\mathrm{n}$ (*i.e.* $\sum n_i i / \sum n_i$, where n_i is the number of chains containing i nanoplates)[90] over the chain growth process. Here we estimated values of i for different chains as $i = L/d$, where L is the length of the chain measured under optical microscopy and d is the center-to-center spacing between neighboring nanoplates in a chain determined from SAXS (**Figure 2.5B and Table 2.2**). The measured $\bar{X}_\mathrm{n}$ grows linearly with time t (**Figure 2.5C**), which is another qualitative feature of step-growth polymerization. Similarly, the average chain length grows linearly with time, which is also consistent with step-growth polymerization and the fact that the system is a closed system, with a constant number of nanoplates in the field of view (**Figure 2.7B**). We then applied the rate equation for the externally-catalyzed molecular step-growth polymerization of bifunctional monomers with identical functional groups,[90] namely $\bar{X}_\mathrm{n} = 4[M]_o kt + 1$ (where $[M]_o$ is the initial molar concentration of silver nanoplates in the field of view), to estimate the nanoplate self-assembly rate constant, k, as 3.2×10^7 $\mathrm{M^{-1}s^{-1}}$. This rate constant is three orders of magnitude larger than one that has been measured in an inorganic nanocrystal system (2.9×10^4 $\mathrm{M^{-1}s^{-1}}$).[90] We attribute this difference to the fact that the pairwise interaction between nanoplates—*i.e.* the driving force for self-assembly—is much stronger in this system, since it scales with the nanoplate surface area. This 1D chain formation is also observed with nanoplates of different edge lengths. We observed the assembly of larger nanoplates at lower ionic strengths (~0.5 mM for 2.17 µm nanoplates, ~0.8 mM for 1.44 µm nanoplates, *etc.*) which we attribute to the stronger net attraction between larger nanoplates. For the same reason, we expect that nanoplates would assemble at an even higher rate with higher ionic strengths, or with larger sizes at the same ionic strength condition, due to stronger attractions with each other.

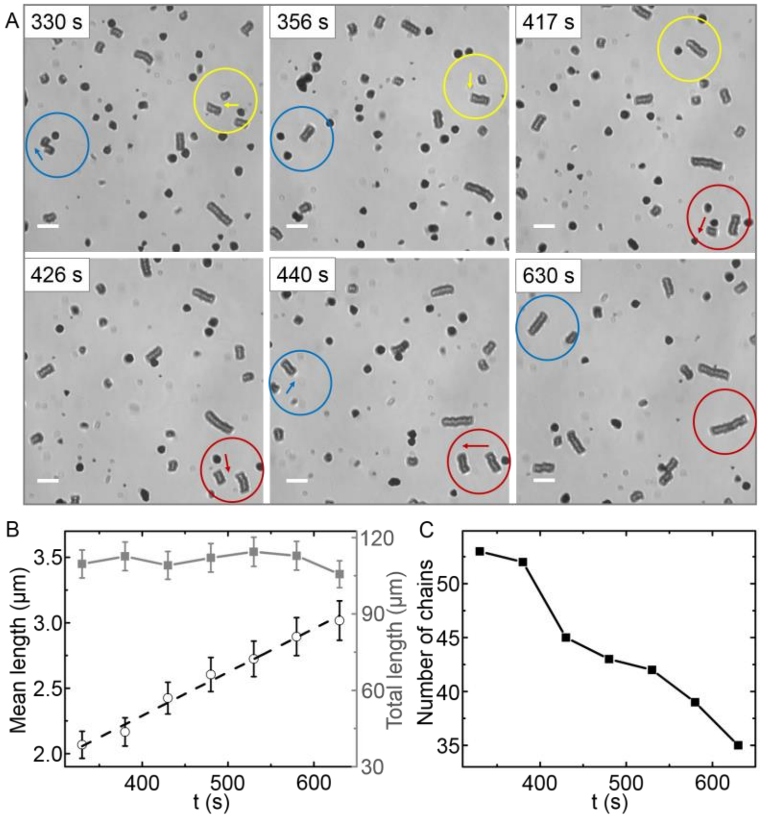

Figure 2.7. Step-growth polymerization of bifunctional nanoplates. (A) Time-lapse optical microscopy images of the silver chain growth process in the early growth stage (330 s to 630 s after adding NaCl solution to screen electrostatic repulsion between nanoplates) showing the step-growth polymerization mechanism. Different circles represent the growth of different chains, with the arrows highlighting the chain addition. Ionic strength: 1.4 mM. Scale bars: 5 μm. (B) Mean chain length growth (black circles) and total chain length (grey squares) in the field of view over time. The linear fitting (black dotted line) gives a growth rate of 3.3×10^{-3} μm/s ($R^2 = 0.99$). The error bars are from measurement errors. (C) Total number of chains in the field of view as a function of time. Due to the limited resolution of the optical microscope, we neglected measurements of very short chains (chain length < 1 μm) which could not be distinguished from single nanoplates during analysis. These short chains or single nanoplates are ~8% compared with all the chains in the field of view. (Reprinted with permission from [51]. Copyright © 2017, American Chemical Society.)

Table 2.2. The calculated center-to-center d spacing values ($d = \frac{2\pi}{q_1}$) between neighboring nanoplates in the chain, peak positions q_1 to q_6, and ratios between higher-order peak positions (q_2 to q_6) and the first-order peak position q_1 in SAXS spectra at two different ionic strength conditions (1.4 and 3.0 mM). The first- or second-order peak was not shown in the measured range (see **Figure 2.5B**) and was derived based on higher-order peak positions.

Ionic strength (mM)	d (nm)	q_1 (1/Å)	q_2 (1/Å)	$\frac{q_2}{q_1}$	q_3 (1/Å)	$\frac{q_3}{q_1}$	q_4 (1/Å)	$\frac{q_4}{q_1}$	q_5 (1/Å)	$\frac{q_5}{q_1}$	q_6 (1/Å)	$\frac{q_6}{q_1}$
1.4	116.6	0.00539*	0.0108*	2.0	0.0161	3.0	0.0216	4.0	0.0270	5.0	0.0334	6.2
3.0	85.5	0.00735*	0.0147	2.0	0.0222	3.0	0.0299	4.1	0.0376	5.1	0.0451	6.1

*These q values were derived based on higher-order peak positions.

We also found that the distribution of chain lengths at different times follows a Flory−Schulz distribution[90] (**Figures 2.5D and 2.8**). Namely, the fraction of chains containing i nanoplates (that is, n_i/N_L, where N_L is the total number of chains) is proportional to $(1-p)p^{i-1}$. Here, the fitting parameter p is the extent of reaction, or the probability that a nanoplate has "reacted" and become part of a chain, and is given by $p = ([M]_o - [M])/[M]_o$, where $[M]$ is the concentration of all species (*i.e.* chains of any length) at a particular time. As shown in **Figures 2.5D and 2.8**, as the reaction time increases, more nanoplates have assembled into longer chains, and the extent of reaction obtained from fitting the Flory–Schulz distribution approaches unity. These two features of molecular step-growth polymerization—that the number-average degree of polymerization grows linearly with time, and that the chain length distribution follows a Flory–Schulz distribution—are both ultimately associated with the assumption that reactivity is independent of chain length,[73] which further suggests that pairwise interactions dominate chain growth at this colloidal nanoparticle scale.

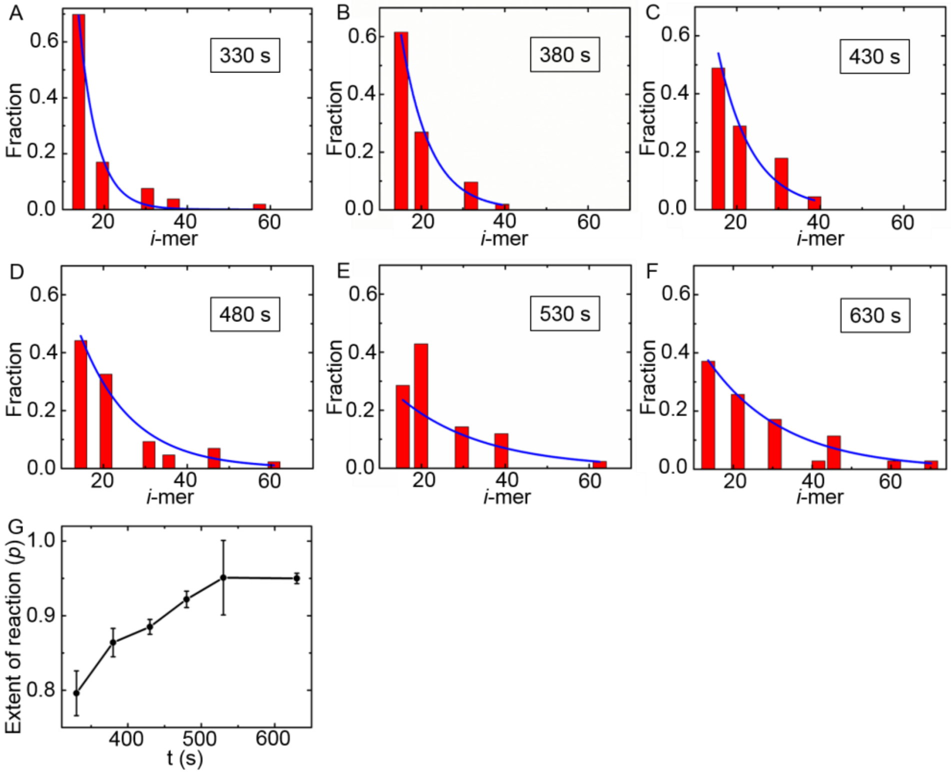

Figure 2.8. The i-mer fraction distributions at different stages of self-assembly and their corresponding Flory–Schulz distribution fitting (blue curves). (A) 330 s, (B) 380 s, (C) 430 s, (D) 480 s, (E) 530 s, (F) 630 s. The bin size is ~8.6. The first binning starts from 8.6 to 17.2, since the smallest i measured is 8.6 (corresponding to a chain of 1 μm long). (G) The extent of reaction (p) determined from the Flory–Schulz distribution fitting at different times. The error bars are from the standard error of the Flory–Schulz distribution fitting. (Reprinted with permission from [51]. Copyright © 2017, American Chemical Society.)

Seeded growth, although an established synthesis method for silver nanoplates, can still give rise to particles with some size dispersity (namely, both the large nanoplates we observed assembling and much smaller nanoplates), as shown in **Figure 2.1**. The population of smaller nanoplates in the sample has edge lengths 22–49% the size of the large nanoplates. However, these smaller nanoplates do not substantially affect the assembly of large ones because they have a considerably smaller surface area and, therefore, smaller van der Waals attraction. In particular, the net attraction between two large nanoplates at 1.4 mM ionic strength was calculated to be about –35 $k_{\mathrm{B}}T$ (where k_{B} is the Boltzmann constant and T is the temperature), favoring step-growth polymerization-like assembly. The net attraction between small–small nanoplate and small–large nanoplate pairs at the same ionic strength condition, based on the average size of the small nanoplates, is only about –4 $k_{\mathrm{B}}T$, which is not strong enough to induce stable assembly into chains.[80] Thus, small nanoplates do not tend to assemble with one another or with large nanoplates at relatively low ionic strength conditions (*i.e.* below 1.8 mM based on interaction calculations, see **Figure 2.9D**). To confirm this experimentally, we characterized the assembled chains after rapid solvent evaporation under vacuum condition by scanning electron microscopy (SEM). It is clear that these chains are primarily composed of large nanoplates of similar size (**Figure 2.10**). Meanwhile, unassembled small nanoplates are likely unable to serve as depletion agents that could enhance the self-assembly of large nanoplates, due to (i) the insufficient size separation between large and small nanoplates[13, 91, 92] and (ii) the very low number density of small nanoplates in solution. The estimated depletion attraction between two larger nanoplates induced by the smaller nanoplates is only about –0.03 $k_{\mathrm{B}}T$, which is negligible compared with the total net attraction strength (–35 $k_{\mathrm{B}}T$, see **Figure 2.9B**). This is also consistent with the fact that considering only electrostatic repulsion and van der Waals attraction in assembly very closely predicts the equilibrium lattice spacings in the assembled chains measured by SAXS (**Figure 2.9C**).

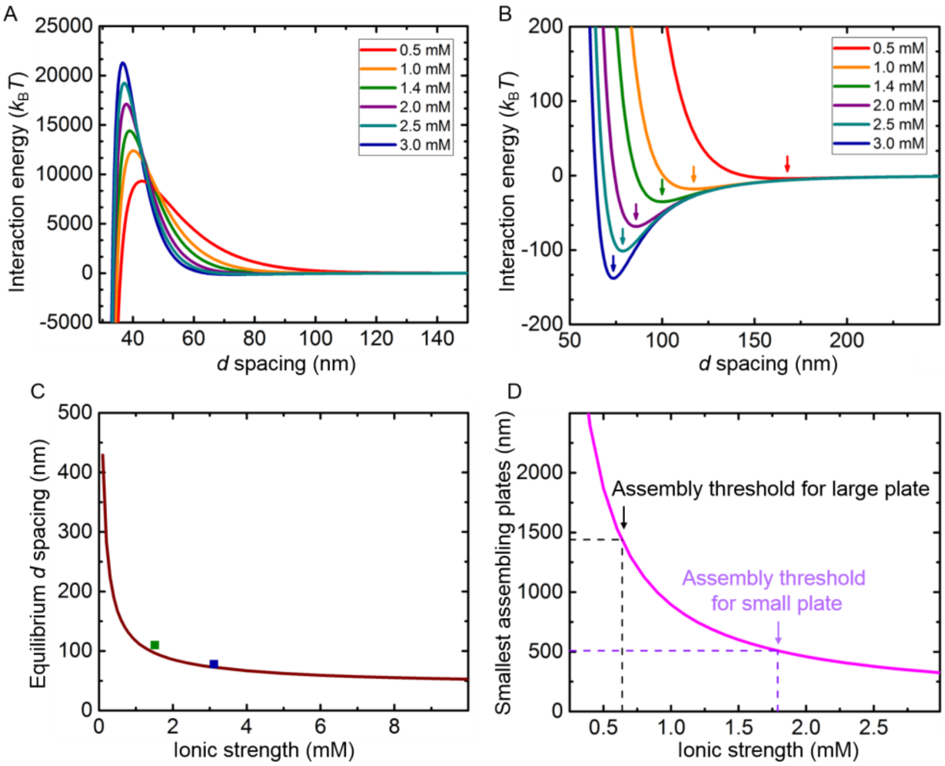

Figure 2.9. Interaction potential calculations and equilibrium center-to-center d spacings of two face-to-face assembled silver nanoplates. (A) Net interaction energy as a functional of center-to-center d spacing between two silver nanoplates at different ionic strength conditions. (B) A zoomed-in version of the plot in (A) showing the location of secondary energy minima at the equilibrium center-to-center d spacing. (C) The locations of secondary minima (namely the equilibrium center-to-center d spacing between two nanoplates) as a function of ionic strength (brown curve). The two squares mark measurements by SAXS at 1.4 (green) and 3.0 mM (blue), indicating decent agreement between the calculations and SAXS measurements. (D) The smallest assembling nanoplates at different ionic strength conditions. Here we set the secondary energy minima strength of at least $-7\ k_B T$ for a stable face-to-face assembly of nanoplates.[80] For interaction calculations of different size nanoplates, all the parameter values are same as (A), also listed in **Table 2.3**, except changing the surface area A_{plate}. For example, for a typical edge length of 1.44 μm, an ionic strength of at least 0.7 mM is needed for assembly (black dotted lines), which is also consistent with experimental observations (~0.8 mM); for assembly of small nanoplates (*i.e.*, 0.51 μm edge length), an ionic strength of at least 1.8 mM is needed (lavender dotted lines). (Reprinted with permission from [51]. Copyright © 2017, American Chemical Society.)

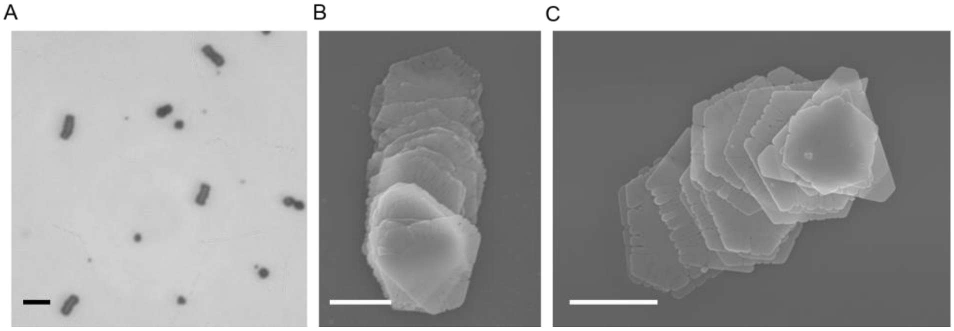

Figure 2.10. Characterization of assembled chains before and after solvent evaporation. (A) An optical microscopy image of assembled chains in 1.6 mM ionic strength solution (below the assembly threshold ionic strength of 1.8 mM for small nanoplates, based on the interaction calculation, see **Figure 2.9D**) before solvent evaporation. (B) and (C): SEM images of the assembled chains after rapid solvent evaporation under vacuum condition. The SEM images show that the assembled chains at this ionic strength condition (1.6 mM) are primarily composed of large nanoplates of similar size (*i.e.*, those with edge lengths of 1.44 ± 0.26 μm). Scale bars are: 5 μm in (A), 1 μm in (B) and (C). (Reprinted with permission from [51]. Copyright © 2017, American Chemical Society.)

Table 2.3. The parameters used in the nanoplate–nanoplate interaction calculation.

Interaction	Parameter	Value
van der Waals attraction	Hamaker constant (H)	1.6×10^{-19} J
	nanoplate edge length (a)	1.44 μm
	nanoplate thickness (t_{plate})	29 nm
electrostatic repulsion	carboxylate–thiol ligand monolayer thickness (t_{ligand})	2.4 nm
	relative permittivity of water (ε)	78.5
	vacuum permittivity (ε_0)	8.854×10^{-12} F/m
	zeta potential of silver nanoplates (ζ)	−41.9 mV

The length of actively assembling chains can be controlled by using a colloidal analogue to the molecular polymerization “chain stopper” strategy.[83, 93] This ability to control chain length has been shown to be an important part of modulating the longitudinal surface plasmon resonance of chains assembled from colloidal nanocrystals[70, 94, 95] and involves the introduction of monofunctional “stoppers” which terminate chain growth. In this context, Janus particles with one negatively charged, nanoplate-repelling polystyrene hemisphere and one gold-coated, nanoplate-attracting hemisphere were chosen to serve as colloidal stoppers (**Figures 2.11A and 2.12**). The degree of polymerization is directly regulated by the Janus particle–nanoplate concentration ratio; as shown in **Figures 2.11B and 2.13**, as a higher ratio of Janus particles is introduced, chains tend to be shorter. The fraction of chains capped with one or two Janus particles is 34% with only 1.2% Janus particles added to the system, and increases to 52% when more Janus particles are added (3.5%), which further demonstrates the effectiveness of the Janus particles as chain stoppers. More specifically, we found that the stopper-based control over the degree of polymerization is modeled by $\bar{X}_\mathrm{n}= 2/(2(1-p)+\frac{c_\mathrm{s}}{c_\mathrm{m}}pe^{-|\Delta U|/k_\mathrm{B}T})$, where c_s is the Janus particle concentration, c_m is the nanoplate concentration, and ΔU is the difference between the nanoplate–nanoplate and nanoplate–Janus particle interaction energies at a particular ionic strength. We applied this model to fit the data shown in **Figure 2.11B**, with $e^{-|\Delta U|/k_\mathrm{B}T}$ as the fitting parameter. The number-average degrees of polymerization $\bar{X}_\mathrm{n}$ obtained from fitting this model show good agreement with experimental results for each concentration ratio condition, as shown in **Table 2.4**. The obtained fitting parameter indicates an interaction energy difference of 1.6 $k_\mathrm{B}T$ to 2.5 $k_\mathrm{B}T$ for the ionic strength of 1.4 mM used in this experiment. Note that this chain stopper strategy is most effective only in a certain ionic strength range (Regime III in **Figures 2.11A and 2.14**). At relatively low ionic strengths (Regime II in **Figure 2.11A**), even though nanoplates start to self-assemble, the attraction between nanoplates and Janus particles is sufficiently small (given the curved surface of Janus particles compared to the flat surface of nanoplates) that they do not tend to assemble stably with one another. Meanwhile, at very high ionic strengths (*i.e.* Regime IV, when electrostatic repulsions between all particles are greatly screened), Janus particles self-assemble into clusters, which reduces the number of Janus particles available to attach to chain ends and arrest chain growth.

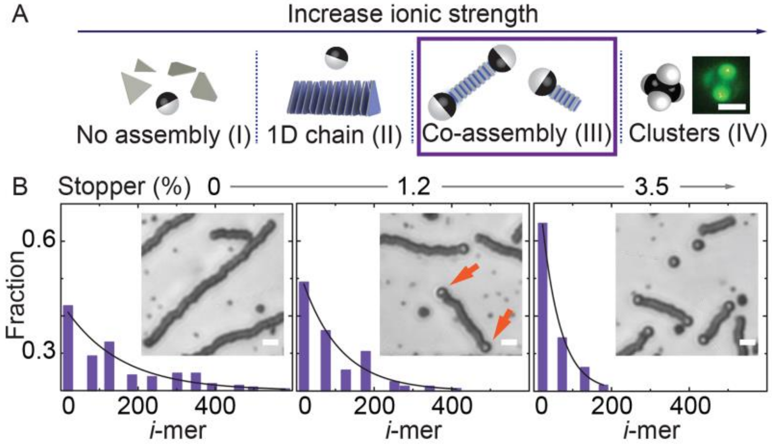

Figure 2.11. Control over chain length through co-assembly of anisometric nanoplates and Janus particles. (A) A schematic (not to scale) showing four ionic strength regimes that generate different assemblies from a binary mixture of nanoplates and Janus particles. The purple box highlights the "chain stopper" regime. The fluorescence microscopy image shows a representative tetrahedral cluster formed from Janus particles with a diameter of 2 µm. For corresponding optical microscopy images, see **Figure 2.14**. (B) Equilibrium i-mer fraction distributions and corresponding Flory–Schulz distribution fits (black curves) at different Janus particle–nanoplate concentration ratios (0%, 1.2%, and 3.5%). Each data point is binned over a range of i-mers, with a bin size of ~53. Ionic strength: 1.4 mM. The insets are optical microscopy images showing representative structures. Orange arrows indicate Janus particles attached to chain ends. Scale bars: 3 µm. (Reprinted with permission from [51]. Copyright © 2017, American Chemical Society.)

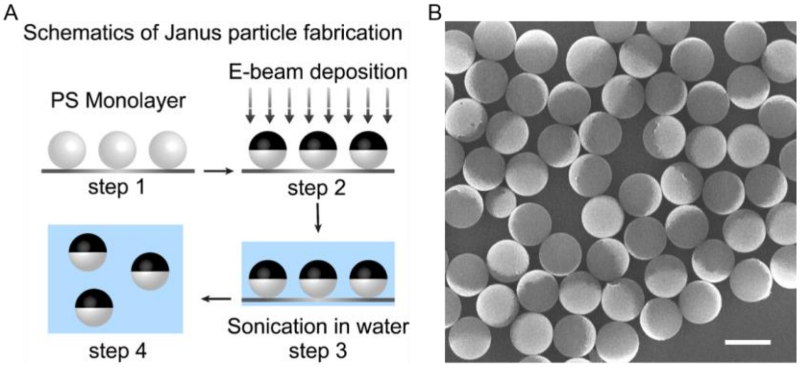

Figure 2.12. Janus polystyrene (PS) particles with a diameter of 2 μm. (A) Schematics of the Janus particle preparation process, which includes four steps: 1) Depositing a PS particle monolayer on glass slide; 2) Applying a 2 nm titanium and a 15 nm gold coating on one side of the particle by e-beam deposition; 3) Collecting Janus particles from the glass slide by sonication in water; 4) Dispersed Janus particles in water. (B) An SEM image of the prepared Janus particles. The bright side on the particle is the gold side and the dark side is the polystyrene side. Scale bar: 2 μm. (Reprinted with permission from [51]. Copyright © 2017, American Chemical Society.)

Table 2.4. Comparison of the number-average degrees of polymerization $\bar{X}_\mathrm{n}$ obtained from "chain stopper" model ($\bar{X}_\mathrm{n}= 2/(2(1-p)+\frac{c_\mathrm{s}}{c_\mathrm{m}}pe^{-|\Delta U|/k_\mathrm{B}T})$ and experimental results. The errors are from measurement errors.

$\frac{c_\mathrm{s}}{c_\mathrm{m}}$ (from experiment)	p (from fitting)	$\bar{X}_\mathrm{n}$ (from experiment)	$\bar{X}_\mathrm{n}$ (from fitting)
0%	0.9931	143 ± 8	145
1.2%	0.9900	90 ± 6	92
3.5%	0.9792	47 ± 6	43

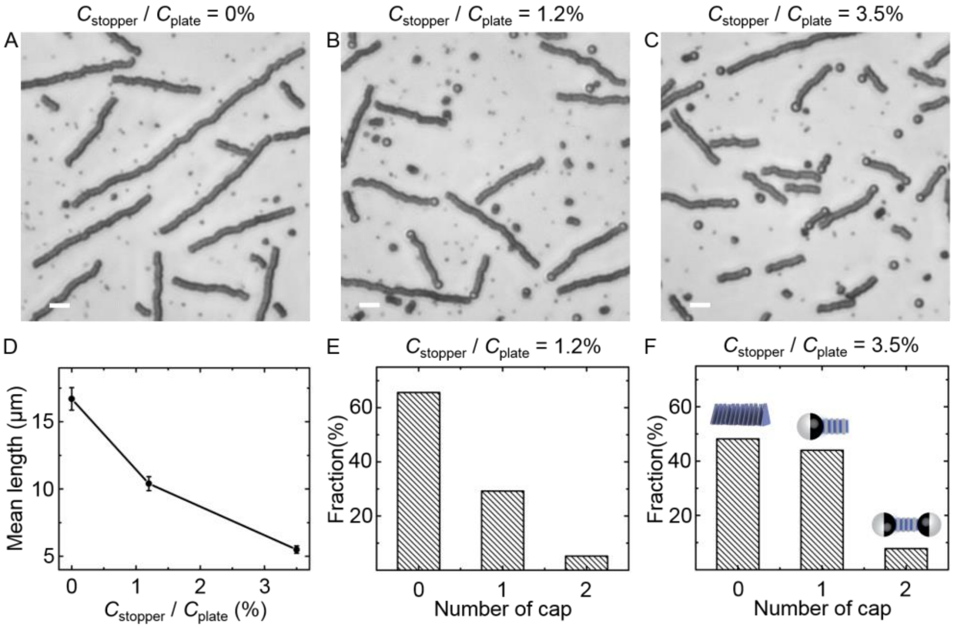

Figure 2.13. Janus particles as chain stoppers. Representative optical microscopy images to show the control over chain lengths through co-assembly of silver nanoplates with Janus particles (stoppers) at different Janus particle–nanoplate concentration ratios. (A) No Janus particles added. All chains grow without hindrance. (B) A relatively low Janus particle–nanoplate concentration ratio of 1.2%. Most chains have their growth halted by Janus particle stoppers. (C) A relatively high Janus particle–nanoplate concentration ratio of 3.5%. Chains tend to be even shorter, as more Janus particles are added for chain stopping. Ionic strength: 1.4 mM. Scale bars: 5 μm. (D) Mean chain length at different Janus particle–nanoplate concentration ratios. The error bars are from measurement errors. The distribution of chains capped with different number of Janus particles (0, 1, and 2, see the corresponding schematics inset in (F)) on the chain ends, at a low Janus particle–nanoplate concentration ratio of 1.2% (E) and high Janus particle–nanoplate concentration ratio of 3.5% (F). Note: The schematics inset in (F) are not drawn to scale. (Reprinted with permission from [51]. Copyright © 2017, American Chemical Society.)

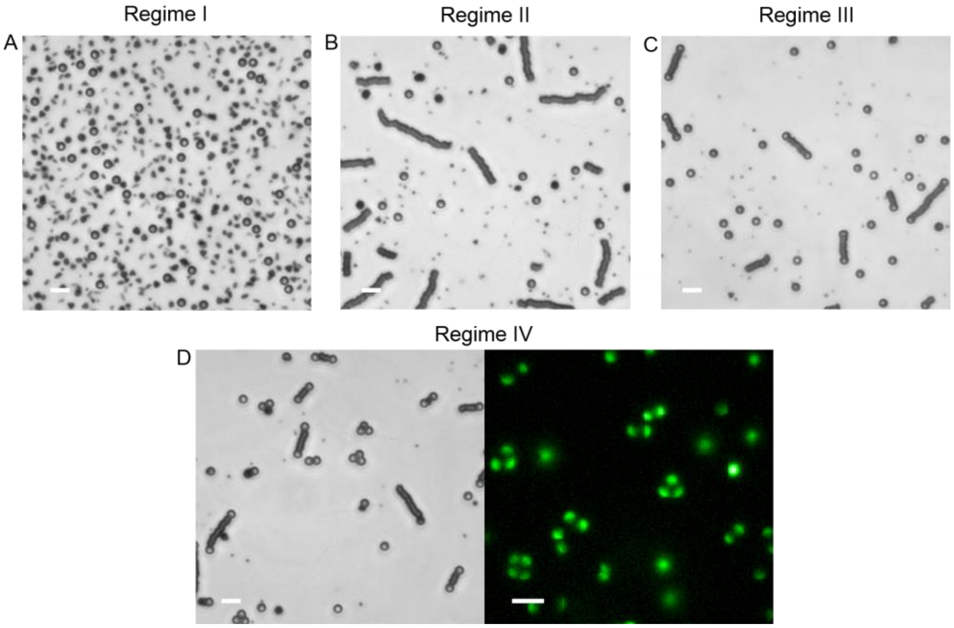

Figure 2.14. Representative optical microscopy images of the assembly of a binary mixture of silver nanoplates and Janus particles in different ionic strength regimes (**Figure 2.11**). (A) No assembly (Regime I). Ionic strength: 0.3 mM. (B) Nanoplate-only chains and dispersed Janus particles (Regime II). Ionic strength: 0.8 mM. (C) The desired co-assembly regime, where Janus particles are attached to the silver chain ends (Regime III). Ionic strength: 1.4 mM. (D) Janus clusters (Regime IV). The left is a bright-field optical microscopy image and the right is a fluorescence microscopy image highlighting the Janus clusters. Ionic strength: 3.0 mM. Scale bars: 5 μm. (Reprinted with permission from [51]. Copyright © 2017, American Chemical Society.)

Fine-tuning the ionic strength also enables direct modulation of the stiffness of co-assembled chains. Colloidal chain stiffness is the central control variable in applications of so-called electrorheological[96-98] and magnetorheological[99, 100] fluids, where the strength of an applied electric or magnetic field is used to manipulate chain fluctuations and, consequently, the rheological properties of a chain solution. To quantify chain stiffening in this system, from real-time optical microscopy movies we characterized the transverse fluctuations of chains for two ionic strength conditions (1.4 mM and 3.0 mM). Specifically, we tracked chain “skeletons” for one hundred frames (about 5.81 s in total) and considered statistics of the transverse displacement

Δh of two points as a function of their relative separation $|x - x'|$ along a chain[77-79] (**Figure 2.15A–C**). At low relative separations, this relationship follows a power law of the form $\langle(h(x) - h(x'))^2\rangle^{1/2} \propto |x - x'|^\alpha$ (**Figure 2.15D**), where α is referred to as the "roughness exponent." At a lower ionic strength (1.4 mM), averaging data from four chains of different chain lengths (see **Table 2.5**) gives $\alpha =$ 0.736 ± 0.018 whereas at a higher ionic strength (3.0 mM), $\alpha =$ 0.656 ± 0.013. This exponent characterizes the steady-state chain roughness, with an exponent of α > 0.5 arising in the case of a biased or directed random walk.[79] In this context, such a walk is mostly restricted to the transverse direction, as strong volume exclusion effects between nanoplates impede any substantial chain bending. We attribute the difference in this exponent between ionic strength conditions to the more attractive potential between nanoplates at higher ionic strength, which more strongly disfavors the enthalpy penalties associated with larger transverse misalignments. Based on a Boltzmann-type argument, the strength of inter-nanoplate interactions permits them to slide past one another by as much as a few tens of nanometers at both ionic strengths (see **Figure 2.16**), but greater degrees of sliding are possible at a lower ionic strength. The magnitude of the lateral fluctuations we observed under optical microscopy is consistent with this energetic estimate (**Figure 2.16C**). We also calculated the persistence length of eight different chains (four for each ionic strength condition). The persistence length is a measure of the flexibility of a chainlike object and can be defined as the length scale beyond which vectors tangent to the chain contour lose their correlation.[75] In each case, the persistence length calculated for a chain exceeds its length by about one order of magnitude or more (**Figure 2.17 and Table 2.5**), which further indicates that the assembled chains are essentially "rigid rods" and unbending. In addition, the persistence length also increases with increasing ionic strength, which is a further indication of stiffening.

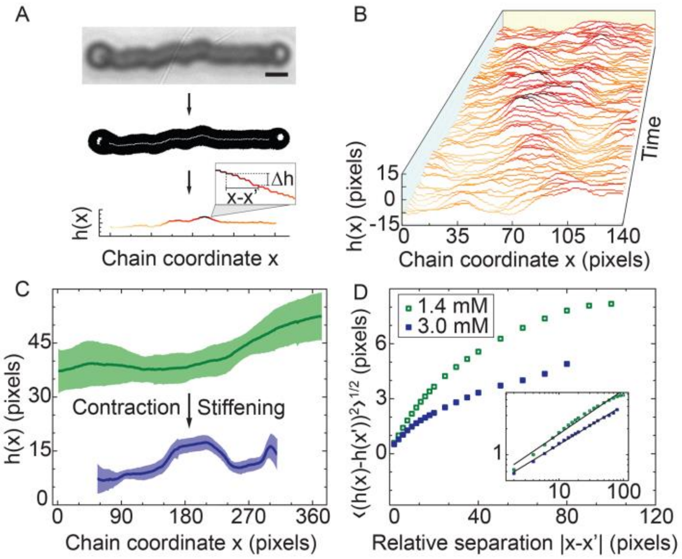

Figure 2.15. Analysis of chain fluctuation. (A) Optical microscopy image analysis and extraction of $h(x)$. Scale bar: 2 µm. (B) Accumulated height functions for a particular chain over 75 frames (about 4.36 s in total). The height axis has been scaled by ~110% for clarity between different curves. Pixel size: 1/73.86 nm. (C) Chains stiffen and contract upon an increase in ionic strength. Here we compare the overall length and the standard deviation of $h(x)$ at each x over 100 frames (denoted by the shaded area around a line tracing the temporal average at each point) for a chain capped with Janus particles on both ends that is initially exposed to low ionic strength (1.4 mM, top) and later to higher ionic strength (3.0 mM, bottom). (D) Root-mean-squared transverse displacement $\langle (h(x) - h(x'))^2 \rangle^{1/2}$ *versus* relative separation $|x - x'|$ at two ionic strength conditions (1.4 mM and 3.0 mM). The inset is a log-log plot of the same data used to determine the power law scaling. (Reprinted with permission from [51]. Copyright © 2017, American Chemical Society.)

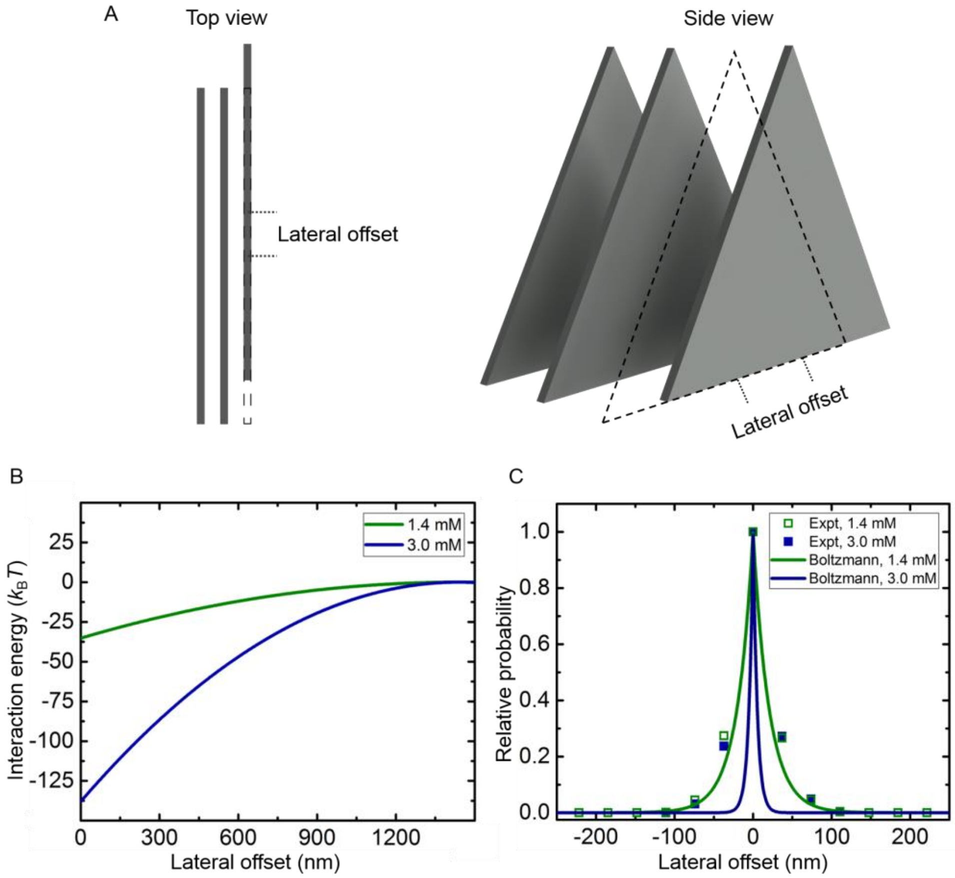

Figure 2.16. Interaction energy and probability of chain lateral offset. (A) Schematics (not to scale) of nanoplate lateral offset in a chain due to “sliding” away from the central position. Left: top view. Right: side view. (B) A plot showing the interaction energies at the equilibrium center-to-center spacing as a function of lateral offset distance at two ionic strength conditions. (C) Relative probability at different lateral offset distances at two ionic strength conditions, based on a Boltzmann probability distribution. The squares in the plot are the experimentally observed distribution of $h(x+1)-h(x)$ normalized to zero offset (*i.e.*, such that $h(x+1)-h(x)=0$ has relative probability of 1) for each ionic strength condition, for qualitative comparison. (Reprinted with permission from [51]. Copyright © 2017, American Chemical Society.)

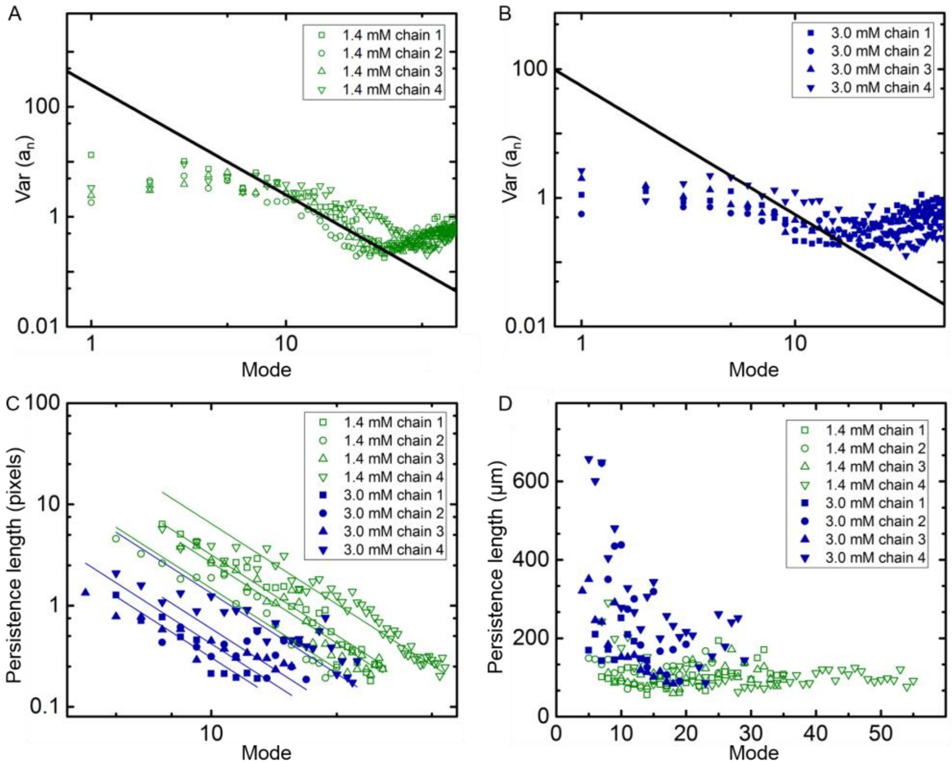

Figure 2.17. Persistence length analysis. (A) and (B) The log−log plots showing the variance of the mode amplitude as a function of the mode number for eight chains across the persistence length spectrum at (A) 1.4 and (B) 3.0 mM ionic strength conditions. The black lines in (A) and (B) have a slope of –2, indicating the regime(s) where the relation between mode number and persistence length applies. (C) Linear fitting of the curves in (A) and (B) at the low mode regions. Pixel size: 1/73.86 nm. (D) Persistence length as a function of the mode number for eight chains analyzed. The persistence length values for each chain are also listed in **Table 2.5**. (Reprinted with permission from [51]. Copyright © 2017, American Chemical Society.)

Table 2.5. Roughness exponents and persistence length values for each of the eight chains analyzed. The errors shown in the averaged values for both ionic strength conditions are the standard deviation among different chains. The errors in the persistence length for each chain are from averaging persistence lengths for different modes.

Ionic strength	Chain labeling (length)	Roughness exponent α	Persistence length (μm)
1.4 mM	chain 1 (13.96 μm)	0.753	103 ± 31
	chain 2 (10.34 μm)	0.730	119 ± 28
	chain 3 (13.00 μm)	0.730	105 ± 26
	chain 4 (20.39 μm)	0.735	112 ± 44
1.4 mM average		0.737 ± 0.011	
3.0 mM	chain 1 (5.69 μm)	0.750	178 ± 37
	chain 2 (9.53 μm)	0.673	271 ± 158
	chain 3 (6.57 μm)	0.559	181 ± 88
	chain 4 (13.74 μm)	0.735	292 ± 155
3.0 mM average		0.679 ± 0.087	

As shown in **Figure 2.15C**, chain stiffening is accompanied by chain contraction. Chains contract because the equilibrium center-to-center spacing between nanoplates, d, decreases with increasing ionic strength. The relative contraction measured from the initial and final length of the nanoplate portion of co-assembled chains in optical micrographs (0.70 ± 0.08, based on averaging the contraction of three chains, see **Table 2.6**) is consistent both with the d spacing ratio determined from SAXS (0.73 ± 0.01) and predictions from theoretical calculations[30] (0.74, see **Figure 2.9**).

Table 2.6. Comparison between the relative contraction of co-assembled chains upon an ionic strength increase from 1.4 mM to 3.0 mM as obtained from optical microscopy, SAXS, and theoretical calculations. The errors shown in chain length measurements are from measurement errors. The errors shown in SAXS data are from averaging three SAXS measurements at each ionic strength condition.

	1.4 mM	3.0 mM	Relative contraction
Length of chain 1 (μm)	28.05 ± 1.40	18.74 ± 0.94	0.67 ± 0.07
Length of chain 2 (μm)	21.79 ± 1.09	15.31 ± 0.77	0.71 ± 0.07
Length of chain 3 (μm)	20.51 ± 1.03	14.81 ± 0.74	0.73 ± 0.08
Averaging three chains			0.70 ± 0.08
d from SAXS (nm)	116.9 ± 0.3	85.1 ± 0.9	0.73 ± 0.01
d from calculation (nm)	100.0	73.6	0.74

At higher ionic strengths within Regime III, a Janus particle can accommodate more than one chain on its gold hemisphere, which leads to the formation of 2D, not just 1D structures. In particular, by increasing the ionic strength (while remaining below the threshold for Janus particle clustering), one can further screen the electrostatic repulsion between nanoplates and Janus particles and make Janus particles bifunctional, such that they connect chains into a "V" shape (**Figures 2.18A and 2.19**). We found that two chains connected by a Janus particle tend to stay in physical contact (**Figure 2.18B**), which we hypothesize is either due to a lateral van der Waals attraction between chains or an effort to maximize the rotational entropy of the Janus particle[101] (**Figure 2.20**). As such, the "bond angle" θ (**Figure 2.18B**) can be estimated directly from the size of the Janus particle (diameter D) and the width of the chains (W, *i.e.* the average edge length of the assembled nanoplates) as $\theta = 2\, tan^{-1}(W/D)$. If W = 1.15 µm and D = 2 µm, the predicted bond angle is 60° (*i.e.* the interior angle of an equilateral triangle), which is consistent with the dominant bond angle observed in experiments with particles of this size combination (**Figures 2.18C and 2.21A**). Other assemblies, such as "zigzag" chains and multimembered rings, were also observed in the binary mixture system (**Figures 2.18C and 2.22**).

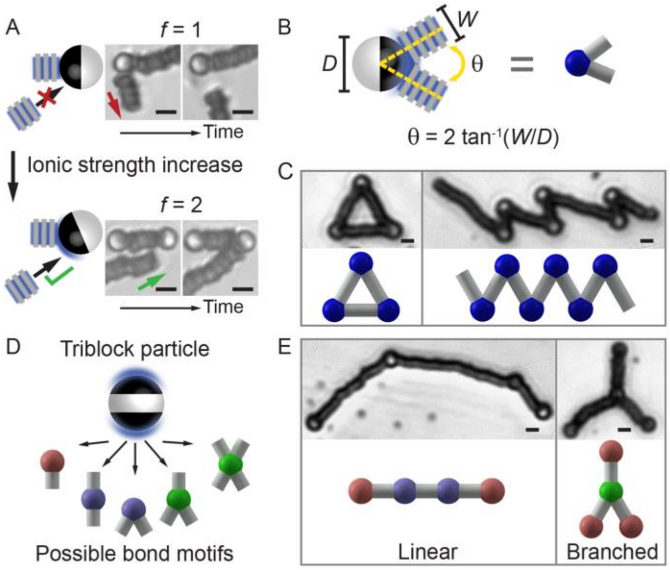

Figure 2.18. Co-assembly of anisometric nanoplates with patchy spheres. (A) Schematics and representative optical microscopy images showing the functionality (f) of the Janus particles changes from 1 to 2 when the ionic strength is increased from 1.0 to 1.6 mM. (B) A schematic showing the bond angle θ. (C) Optical microscopy images of a triangular ring and "zigzag" chain, with corresponding schematics, assembled from nanoplates with a 1.15 ± 0.14 µm edge length (large nanoplate population) and Janus particles with a diameter of 2 µm. Ionic strength: 1.6 mM. (D) Schematics of a triblock particle with a functionality of 4 and the possible bond motifs with nanoplates. (E) Representative optical microscopy images and schematics of linear and branched assemblies from nanoplates and triblock particles. Ionic strength: 1.6 mM. Scale bars: 2 µm. (Reprinted with permission from [51]. Copyright © 2017, American Chemical Society.)

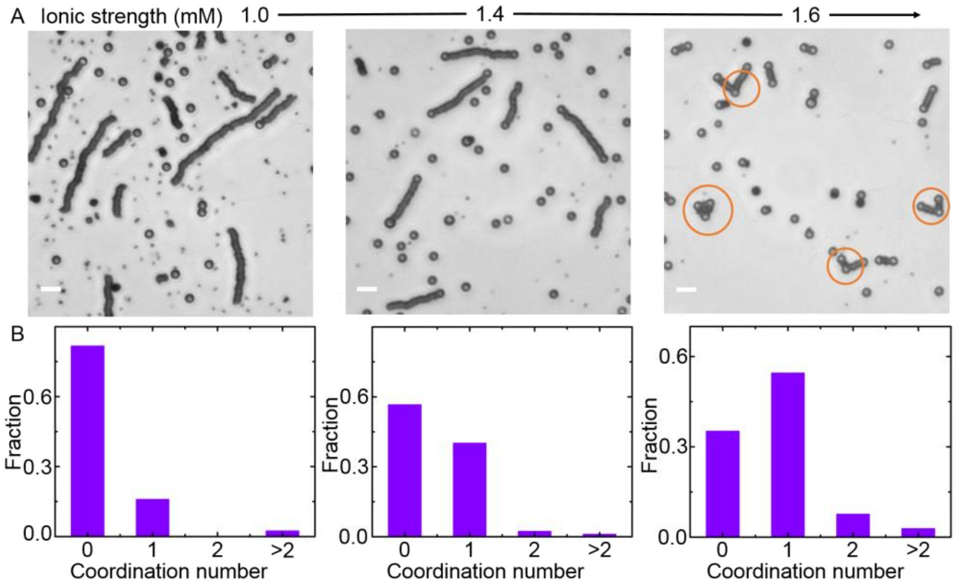

Figure 2.19. Janus particle coordination number distribution at different ionic strengths. (A) Typical optical microscopy images of structures assembled from nanoplates and Janus particles at three ionic strengths (1.0, 1.4 and 1.6 mM). Scale bars: 5 μm. (B) The Janus particle coordination number distribution plots at different ionic strength conditions. In the horizontal coordinate, “0” means an unassembled Janus particle; “1” means a Janus particle with one chain attached; “2” means a Janus particle with two chains attached (highlighted by the orange circles in the optical microscopy image); “>2” means a Janus particle cluster. In all of these three plots, more than 120 Janus particles were measured and we compared regions where the chain–Janus particle concentration ratio is similar (0.7–0.8 on average) at the three ionic strength conditions. Note that the Janus particle coordination number distribution is slightly different at regions with different chain–Janus particle concentration ratios. (Reprinted with permission from [51]. Copyright © 2017, American Chemical Society.)

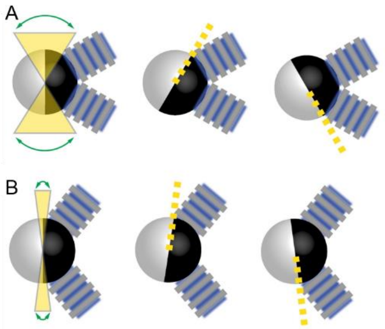

Figure 2.20. Schematics indicating the different degrees of Janus particle rotational entropy in the two-chain coordination case. (A) The case when the two chains on the Janus particle are in physical contact, giving the Janus particle more rotational entropy without reducing contact area with both chains on the Janus particle, as shown in the yellow region. (B) The case when the two chains on the Janus particle are away from each other, giving the Janus particle less rotational entropy, as shown in the yellow region. (Reprinted with permission from [51]. Copyright © 2017, American Chemical Society.)

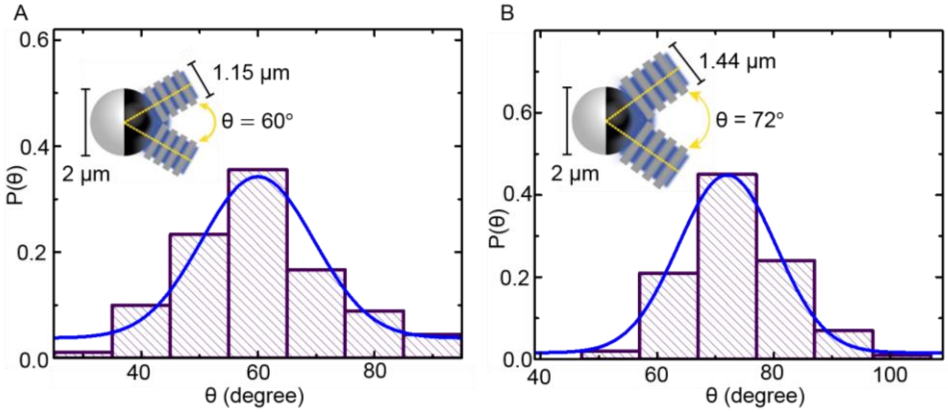

Figure 2.21. Experimental bond angle distributions in the two-chain coordination case with two different nanoplate–Janus particle size ratios at an ionic strength of 1.6 mM. (A) There is a dominant bond angle of 60° between the two silver chains (assembled from nanoplates with an average edge length of 1.15 μm) attached to the Janus particle (2 μm in diameter). (B) There is a dominant bond angle of 72° between the two silver chains (assembled from nanoplates with an average edge length of 1.44 μm) attached on the Janus particle (2 μm in diameter). In both cases, the bond angle distributions are obtained based on ~100 measurements. (Reprinted with permission from [51]. Copyright © 2017, American Chemical Society.)

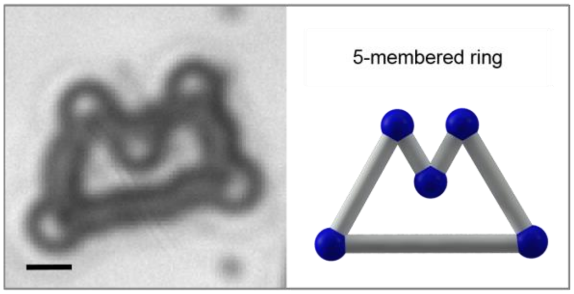

Figure 2.22. Optical microscopy image (left) of a 5-membered ring assembled from nanoplates with a 1.15 ± 0.14 μm edge length and Janus particles (2 μm in diameter). Ionic strength: 1.6 mM. Scale bar: 2 μm. (Reprinted with permission from [51]. Copyright © 2017, American Chemical Society.)

The library of possible structures is further enriched through the incorporation of multipatch spheres.[81] The triblock particles used here, for example, have attractive gold patches at both "north" and "south" poles (**Figures 2.18D and 2.23**). When both of the triblock particle patches have a functionality f = 2, these triblock particles can exhibit I-, V-, Y-, or X-shaped bonding with silver nanoplates (**Figure 2.18D**). One can use these motifs to construct various linear and branched structures (**Figure 2.18E**). The broader potential of this strategy lies in the modularity of the size, position, and number of patches on the linker surface. Moreover, the linker colloids need not be spherical. In fact, this method to assemble many different architectures from only one or two types of "monomers" simply by varying the linker unit is commonly used in biology[102-104] and has already shown great success in other synthetic systems.[105-107] For example, using the patchy spheres implemented here, if the angle between two gold patches is ϕ and the linked chains are of similar length, one would anticipate an m-membered ring to form, with m given by $m = 360°/(180° - \phi)$ (**Figure 2.24**). Going even further, by varying which linkers are present over the course of nanoplate polymerization, it would be possible to co-assemble an even wider variety of shapes and architectures.

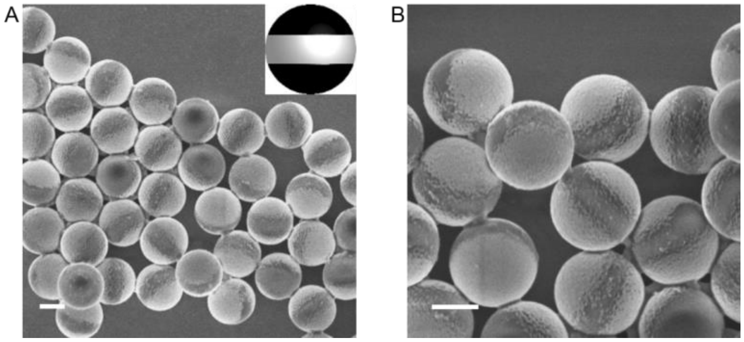

Figure 2.23. Low- (A) and high-magnification (B) SEM images of triblock particles with a diameter of 2 μm. The bright parts on the particle are the two gold patches and the dark part in the middle of the particle is the polystyrene side. The inset in (A) is a schematic of a triblock particle (gold in black, and polystyrene in white). Scale bars: 1 μm. (Reprinted with permission from [51]. Copyright © 2017, American Chemical Society.)

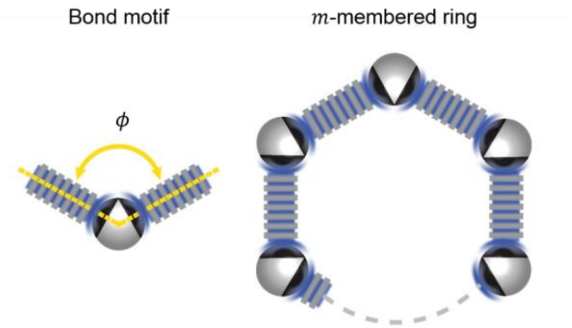

Figure 2.24. The m-membered ring structures one might expect from the co-assembly of angled patchy spheres and silver nanoplates. Here, m can be estimated by $m = \frac{360°}{180°-\phi}$, if the chain segments are of roughly uniform length and ϕ is the angle between the two gold patches on the polystyrene particle, which can be tuned following a reported method.[81] (Reprinted with permission from [51]. Copyright © 2017, American Chemical Society.)

Conclusions

In summary, we demonstrate that a combination of highly anisometric silver nanoplates and patchy spheres can be used to “polymerize” a wide variety of adaptive 1D and 2D structures. We show that the ionic strength can be used during assembly to control the functionality of linkers (Janus and triblock particles) and, consequently, the morphologies of structures that assemble. We also show that ionic strength can be used post-assembly, for the dynamic manipulation of structural properties, such as the size, stiffness, and interparticle distance within assemblies. We hope these results can inspire the bottom-up fabrication of highly adaptive structures with advanced properties, or perhaps serve as the basis for controlled, synthetic analogues to functional one- and two-dimensional structures found in nature.[108, 109]

Methods

Synthesis of Anisometric Silver Nanoplates. A modified seeded-growth method was used to synthesize anisometric silver nanoplates.[47] Silver seeds were prepared first, by sequential addition of aqueous solutions of $AgNO_3$ (25 mL, 0.1 mM), sodium citrate (600 µL, 75 mM), and hydrogen peroxide (30 wt %, 60 µL) to a 125 mL Erlenmeyer flask being stirred at 300 rpm at room temperature in air. After addition of the hydrogen peroxide, the stirring speed was increased to 1050 rpm before rapid injection of a freshly prepared aqueous $NaBH_4$ solution (250 µL, 0.1 M). This $NaBH_4$ solution was prepared by adding water which had been precooled in an ice bath for 10 min to solid $NaBH_4$ and vortexing immediately. The seed solution turned blue approximately 4–10 min after the injection of the $NaBH_4$ solution and was kept stirring for another 5 min after this color change. Then the seed solution was centrifuged (using an Eppendorf Centrifuge 5804) at 10500 rpm for 8 min and the sediment was redispersed in 10 mL 0.94 mM sodium citrate solution. A UV–vis spectrum of the as-prepared seeds was measured using a Scinco S-4100 PDA spectrophotometer. From batch to batch, the extinction peak position was at wavelengths between 700 and 800 nm (**Figure 2.1A**). In a typical seeded-growth process, the seed solution was diluted until a peak intensity value of 0.012 was achieved, using additional 0.94 mM sodium citrate solution. Then, 0.75 mL L-Ascorbic acid (0.1 M) was added to 20 mL of this diluted seed solution in a 40 mL glass vial (Fisherbrand, 29 mm × 94 mm). A separate solution was prepared by mixing 20 mL $AgNO_3$ (1.0 mM), 0.125 mL citric acid (0.1 M), and 0.1 mL sodium citrate (1.5 mM). This solution was added to the seed solution dropwise through a syringe pump (Fusion 200, Chemyx Inc.) with an injection rate of 0.4 mL/min. After 5 min (2 mL) of injection, two-thirds of the reaction solution was removed, and the remaining amount was used as a source of seeds for the next growth cycle. The removed products of the first few cycles were discarded (since the nanoplates at these stages were still small) but samples from cycles 3, 4, and 5 were collected in separate 8 mL glass vials (Wheaton). During the whole growth process, the seed solution was shaking vigorously at room temperature with a thermomixer (Eppendorf, ThermoMixer C) at a shaking speed of 300–1000 rpm. Silver nanoplates of different edge lengths were obtained from the products of different cycles (**Figure 2.3).** We found that the UV–vis extinction peak position measured from a solution of the prepared seeds, the injection rate, and the shaking speed during growth would also affect (or were related to) the edge length of the nanoplates. More details on the effects of these parameters are given in **Table 2.1**.

Thiol Modification of Silver Nanoplates. The surfaces of silver nanoplates as-synthesized were coated with citrate ligands. These ligands were exchanged with carboxylate–thiol molecules ($HS(CH_2)_{11}(OC_2H_4)_6OCH_2COOH$) to improve colloidal stability in solution. This exchange was performed, first, by adding 200 μL of a 7.93 mM thiol ligand solution to 2 mL of a silver nanoplate sample solution directly collected from a certain growth cycle. This 7.93 mM thiol solution was prepared by adding 5 μL of the thiol as received from Prochimia to 1 mL water and vortexing immediately. After allowing the nanoplates to sit and sediment overnight and removing the resulting supernatant, 2 mL water was added to the sediment to dilute any free thiol ligands and residual ions. After 5 h of additional sedimentation, the supernatant of this solution was removed and the final product was stored in 1.5 mL water in an 8 mL glass vial (Wheaton).

Preparation of Patchy Spheres. Janus particles were prepared by directional electron beam (e-beam) evaporation of gold onto a monolayer of colloidal polystyrene particles on a glass substrate.[80] A 2 wt % aqueous suspension (35 μL) of carboxylate–polystyrene particles (F8825, Invitrogen, 2 μm in diameter) was spread on a glass slide (7.6 cm × 2.5 cm) which had been pretreated with Piranha solution (a mixture of H_2SO_4 and 30 wt % H_2O_2 with a volume ratio of 3:1) for 40 min. The particles were then dried with N_2 to form a sub-monolayer on the glass slide. Then, a 2 nm titanium coating (at a deposition rate of 0.3–0.4 Å/s), followed by a 15 nm gold coating (at a deposition rate of 1.0 Å/s), was deposited vertically on the monolayer using an electron beam evaporation system (Temescal). Next, the glass slide was sonicated (using a Fisher Scientific FS30H ultrasonic water bath) in 15 mL water in a 50 mL centrifuge tube for 40 s to detach the Janus particles from the glass slide. Then, the glass slide was removed from the solution and further sonication of this solution for at least 6 min was applied to break up any Janus particles linked by the gold coating and to obtain dispersed Janus particles. After sedimentation for 3 h, most of the supernatant was removed, such that the volume of the remaining solution was 2 mL. This concentrated stock suspension was used for later characterization and self-assembly experiments. Right before optical microscopy imaging, the Janus particle stock solution was sonicated for 6 min to break up any possible aggregations in the solution. Triblock particles were prepared following a procedure from literature.[81] First, an 8 wt % suspension (in 80 μL water/ethanol with volume ratio of 1:1) of carboxylate–polystyrene particles (F8825, Invitrogen, 2 μm in diameter) was dropped onto a 1 cm × 1 cm Si wafer just barely covered by water in a petri dish. This Si wafer had been pretreated with Piranha solution (see above) to make its surface hydrophilic. The particle suspension quickly spread on the water surface and formed a monolayer covering nearly the entire air–water interface. Then, additional water was carefully added beneath the monolayer to lift the monolayer away from the particles in bulk water. Next, 10 µL of a 2 wt % SDS solution was added to condense the monolayer. After 3 h, the monolayer was picked up using a larger Si wafer (1.5 cm × 2.5 cm, also pretreated with Piranha solution) and dried in air. Next, a 2 nm titanium coating, followed by 25 nm gold coating, was deposited vertically on the particle monolayer (which had been picked up by the Si wafer) using the same electron beam deposition conditions as for Janus particles. After deposition, particles were lifted from the substrate with a polydimethylsiloxane (PDMS) stamp. The PDMS stamp was prepared by mixing Sylgard 184 agents (Dow Corning) with monomer and cross-linking agent at a weight ratio of 10:1 and curing this mixture in an oven at 70 ˚C and under vacuum conditions overnight. Before stamping, the surface of the PDMS was treated with oxygen plasma (Harrick Plasma Cleaner PDC-32G) at 150 mTorr pressure and low power (6.8 W) for 50 s. The particles inverted on the stamp then underwent a second titanium and gold deposition using the same conditions as the first deposition. After the second deposition, particles on the stamp were immersed in 20 mL gold etching solution for 80 s and then washed with 200 mL water three times. The etching solution was prepared by adding 4.93 g $Na_2S_2O_3$, 0.0994 g $K_4Fe^{II}(CN)_6\cdot 3H_2O$, 0.667 g $K_3Fe^{III}(CN)_6$, and 11.2 g KOH to 200 mL water. Finally, the stamp was sonicated (Fisher Scientific, FS30H) in 15 mL water in a 50 mL centrifuge tube for 1 min to collect the triblock particles from the stamp. Then the stamp was removed from the solution and further sonication of this solution for at least 6 min was applied to obtain dispersed triblock particles. After sedimentation for 3 h, most of the supernatant was removed, such that the volume of the remaining solution was 1 mL. This concentrated stock suspension was used for later experiments. Right before optical microscopy imaging, the triblock particle stock solution was sonicated for 6 min to break up any possible aggregations in the solution.

Sample Characterization. The morphology of silver nanoplates was characterized using a Hitachi S4800 High-Resolution scanning electron microscope (SEM) and a JEOL 2100 Cryo transmission electron microscope (TEM). The thickness of carboxylate–thiol-coated silver nanoplates was measured using both tapping-mode atomic force microscopy (AFM, Asylum Research Cypher) and SEM when the nanoplates were in a standing configuration. The silicon wafer used in the AFM measurement was first washed with acetone and isopropanol, with sonication for 15 min in each solvent (Fisher Scientific, FS30H), and then treated with oxygen plasma (Harrick Plasma Cleaner PDC-23G) at medium power for 1 min to make the surface hydrophilic. Then, one drop of the silver nanoplate sample solution was put on the Si wafer and allowed to dry under ambient conditions. The zeta potential of carboxylate–thiol-coated silver nanoplates in pure water was measured using a Zetasizer Nano (Malvern) as –41.9 ± 6.8 mV.

Optical Microscopy Imaging and Image Analysis. The particle suspension (~150 μL) was added to an 8-well chamber (composed of a 0.13 to 0.17 mm thick cover slip with plastic walls to make eight 0.2 to 0.4 mL wells, Chambered Coverglass, Thermo Scientific) for optical microscopy imaging. Bright-field optical microscopy imaging was performed using a Zeiss inverted microscope (Axiovert 200) with a 10× air objective (NA = 0.25), a 63× air objective (NA = 0.75) with 1.6× post-magnification, and 100× oil objectives (NA = 1.45 and 1.30). Optical microscopy images were recorded using a complementary metal–oxide–semiconductor (CMOS) camera (Edmund Optics 5012 M GigE). Epifluorescence imaging was performed using a Zeiss inverted microscope (Observer.Z1) with a 100× oil objective (NA = 1.30) and an iXon electron-multiplying charge-coupled device (EMCCD) camera. A 532 nm laser line was used to excite fluorescence in Nile red fluorophores contained in the polystyrene particles. The particle suspension used for fluorescence microscopy imaging was prepared by first adding the well-mixed silver nanoplate and Janus particle solution (~150 μL) to the same type of 8-well chamber used for bright-field optical microscopy imaging. Typically, we used a Janus particle–nanoplate concentration ratio of 1:100. During imaging, sometimes both fluorescence microscopy and bright-field optical microscopy imaging were applied together in order to see both the fluorescent polystyrene particles and the non-fluorescent silver nanoplates. For all the chain length measurements from optical microscopy images, we assigned a 5% error based on the resolution of the optical microscope. For the images used, we slightly adjusted the contrast and brightness in ImageJ or MATLAB, without changing any feature inside the images.

Small-Angle X-ray Scattering Measurements. SAXS measurements were performed on the chains assembled from silver nanoplates to determine the equilibrium center-to-center spacing between neighboring nanoplates in the chain. Measurements were made on chain solutions with two different ionic strengths, 1.4 and 3.0 mM. In each case, 100 μL of a concentrated chain sample at the desired ionic strength condition was gently transferred into a quartz capillary (1.5 mm outer diameter, 0.01 mm wall thickness, Hampton Research), which was then carefully sealed with poly(tetrafluoroethylene) (PTFE) tape to prevent evaporation. We then waited for 1 h for the sample to equilibrate. Right before the SAXS measurement, the capillary was gently inverted a few times to disperse the concentrated chains uniformly at the bottom of the capillary. Transmission SAXS spectra were collected for 30 min using a home-built setup (Forvis Technologies, Santa Barbara) with a Xenocs GeniX3D Cu Kα ultralow divergence X-ray source (1.54 Å/8 keV) with a divergence of ~1.3 mrad and a Pilatus 300 K 20 Hz hybrid pixel detector (Dectris). FIT2D (software from the European Synchrotron Radiation facility, http://www.esrf.eu/computing/scientific/FIT2D) was used to integrate 2D scattering plots and determine the intensity (I) and scattering vector (q) relation. SAXS spectra show a series of peaks in the detected q range. The fact that q values are integer multiples indicates a 1D lamellar structure.[110] Due to the large lattice spacing of the assembled chains, the first- or even second-order peaks (those with q values less than about 0.01 Å^{-1}) were overwhelmed by the profile of the unscattered beam. Consequently, the q values of these peaks were derived from higher-order peaks. The d spacing, *i.e.*, the equilibrium center-to-center spacing between neighboring nanoplates in the chain, was calculated based on the derived first-order peak position (q_1) as $d = \frac{2\pi}{q_1}$.

Notes to Chapter 2

This chapter is adapted with permission from the paper "Luo, B. et al. Polymerization-like co-assembly of silver nanoplates and patchy spheres. *ACS Nano* **11**, 7626-7633 (2017)",[51] Copyright © 2017, American Chemical Society.

CHAPTER 3: HIERARCHICAL SELF-ASSEMBLY OF 3D LATTICES FROM POLYDISPERSE ANISOMETRIC COLLOIDS

Abstract

Colloids are mainly divided into two types defined by size. Micron-scale colloids are widely used as model systems to study phase transitions, while nanoparticles have physicochemical properties unique to their size. Here we study a promising yet underexplored third type: anisometric colloids, which integrate micrometer and nanometer dimensions into the same particle. We show that our prototypical system of anisometric silver plates with a high polydispersity assemble, unexpectedly, into an ordered, three-dimensional lattice. Real-time imaging and interaction modeling elucidate the crucial role of anisometry, which directs hierarchical assembly into secondary building blocks—columns—which are sufficiently monodisperse for further ordering. Ionic strength and plate tip morphology control the shape of the columns, and therefore the final lattice structures (hexagonal versus honeycomb). Our joint experiment–modeling study demonstrates potentials of encoding unconventional assembly in anisometric colloids, which can likely introduce properties and phase behaviors inaccessible to micron- or nanometer-scale colloids.

Introduction

Anisometry is a potent strategy for biological and artificial building blocks to integrate the merits of both micron- and nanometer-scale dimensions.[51, 62, 71, 105, 111-113] For example, bundling of anisometric tropocollagen helices into the fibrous protein collagen allows multiple building blocks to work in concert under loads, giving collagen its exceptional elastic energy absorption.[62] Nanoscale DNA strands can be engineered to braid into micron-scale filaments to build programmed architectures.[105] Similarly shaped synthetic nanowires can serve as ideal energy transport materials to direct longitudinal conduction of quantum particles such as electrons, phonons, and photons.[111, 112, 114, 115] However, despite extensive work on micron-scale colloids[2, 74, 75, 116-119] and nanoparticles,[4, 5, 120-122] anisometric colloids as a promising and emergent particle type are still greatly underexplored. Most work has focused on one-dimensional anisometric building blocks (filaments, tubes, wires, *etc.*).[62, 105, 111, 112] Recent work by our group and others explored shapes like anisometric metallic plates,[51, 71] which were shown to be great candidates for self-assembly studies. On one hand, a nanoscale thickness (and therefore low gravitational drag) allows the plates to diffuse freely in solution, which enables their assembly in three dimensions (3D). In comparison, previous work on micron-scale colloids has required either a precise match with solvent density[116, 123] or an external field[124] to build 3D structures against gravity. These experimental requirements pose limitations which are in principle irrelevant here. On the other hand, a micron-scale basal plane makes plates visible under optical microscopy, making it possible to track their translational and rotational motions one-by-one and thus elucidate the assembly dynamics from real time and real space imaging, which was not accessible in nanoplate systems characterized previously by small-angle X-ray scattering (SAXS),[125-128] small-angle neutron scattering (SANS),[127] or electron microscopy with dried samples.[129, 130] In comparison, although nanoparticles can assemble into 3D structures,[4, 131, 132] understanding and predictive engineering of their assembly pathways have been challenging due to the technical difficulty in direct imaging of such processes in solution.[5, 49, 133] However, despite the great advantages from anisometric plates, the observed assembly into one-dimensional lamellar superlattices from these plates is the same behavior seen in nano-sized metallic plates;[13, 30] the potential of anisometry to enrich phase behavior was not fully harnessed.

Here we show that the anisometry of silver plates (micron-scale basal plane, nanoscale thickness), when utilized meticulously, opens the design space of colloidal self-assembly to a regime not easily accessible before. Anisometry not only brings the technical ease for studying self-assembly, it also renders strongly directional interactions that favor hierarchical self-assembly along one plate axis at a time. In this way, the initial products in our system, hereafter referred to as "columns", embody the concept of secondary building blocks in molecular crystals,[134] which can further assemble into ordered 3D lattices due to a size-focusing effect (an effective narrowing of the building block size distribution). The apparent shape of columns can be predictively manipulated by ionic strength or the extent of plate tip truncation, which leads to distinct final lattice structures. Such unexpected 3D lattices have not been observed in previous systems of metallic nanoplates.[13, 30, 51, 71] Our study demonstrates the unique secondary building block engineering opportunity enabled by anisometry as well as the greatly enriched phase behaviors of anisometric colloids, which opens doors to incorporating their unique mechanical, optical, and electronic properties into 3D assemblies.[4, 111]

Results and Discussion

Anisometric silver plates studied in this work have a triangular basal plane and tunable extent of tip truncation (**Figures 3.1A and 3.2, Table 3.1**) that we later show as critical to the selection of final lattice structures. The plates were colloidally synthesized following literature methods of seeded growth with slight modification.[47, 51] Tip truncation results from the formation of alternating side during the kinetic expansion of the basal plane, as explained by Lofton and Sigmund in the silver halide model.[135] The first plate type we studied has a long side length L of 1.49 ± 0.24 µm, a short side length L' of 0.79 ± 0.27 µm and a plate thickness t_{plate} of 35 ± 5 nm (**Figures 3.1A and 3.2**). The aspect ratio of the plates, defined as the ratio of circumscribed diameter to the thickness, is as high as ~66. Plates are coated with negatively charged carboxylate–thiols[51] and thus electrostatically repel each other when dispersed in deionized water (**Figure 3.1A**). The plates exhibit vivid in-plane and out-of-plane rotations in 3D as observed under optical microscopy, with a vertical fluctuation height[136] as much as 11 times the plate thickness (**Figure 3.3A–B**). Such out-of-plane rotation in 3D, given one order of magnitude difference between the densities of silver and water, is possible due to the nanoscale thickness.

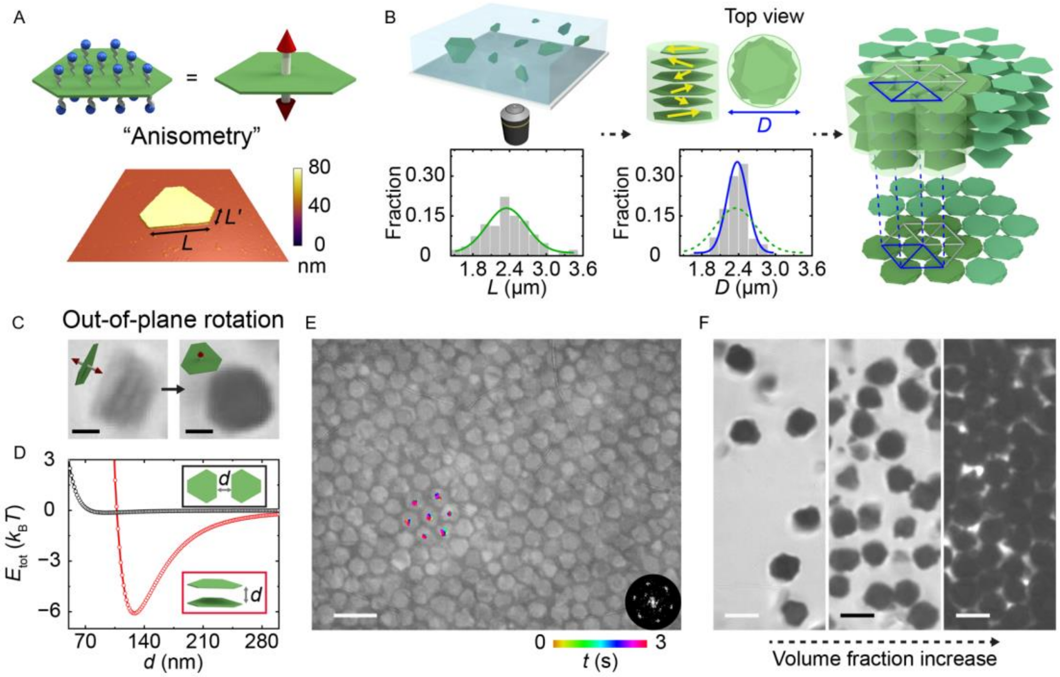

Figure 3.1. Hierarchical self-assembly of polydisperse, anisometric plates into a 3D lattice. (A) Top: schematics of anisometric silver plates (green) coated with thiolated COO^- ligands (blue) and their directional attractions (red arrows). Bottom: a representative atomic force microscopy (AFM) scan over an anisometric plate. The color bar represents height. Scan area: 5 μm × 5 μm. (B) Schematics describing the hierarchical building process: plates first stack into columns (yellow arrows denoting the random orientations of the plates), which then assemble into a hexagonal lattice. The graphs below show the distribution of the long side length L of plates (left, green curve), and that of column projection diameter D (right, blue curve). The L distribution was rescaled so that $\overline{L}$ and $\overline{D}$ have the same value (2.36 μm) for direct comparison. (C) Time-lapse optical microscopy images and schematics showing the lying and standing orientations of the same rotating column. (D) Theoretical calculations of the net pairwise interactions E_{tot} of two plates in the face-to-face (red circles) and side-by-side (black circles) configurations as a function of the plate–plate distance *d* (labeled in inset schematic). (E) An optical microscopy image showing a hexagonal lattice, overlaid with tracked trajectories of the central positions of the column projections. The image was processed as detailed in **Figure 3.4**. The bottom right inset is a Fourier transform pattern of the image. (F) Optical microscopy images showing column arrangements as their concentration increases (from left to right). Ionic strength in (C) to (F): 0.5 mM. The schematics were not drawn to scale. Scale bars: 1 μm in (C), 5 μm in (E), 3 μm in (F). (Reprinted with permission from [50]. Copyright © 2019, Springer Nature.)

Table 3.1. Synthesis conditions of silver plates of different side lengths and truncations.

The peak intensity in UV-vis spectrum of the seed solution after dilution	Injection rate (mL min^{-1}) and injection time (min) in each growth cycle	Shaking or stirring speed during growth (rpm)	The growth cycle to collect product	Long side length L (μm)	Average truncation $\overline{m}$
0.012	0.2, 10	700 in cycle 1, 1000 in later cycles (shaking)	Cycle 5	1.49 ± 0.24	0.55
0.0024	0.4, 5	700 in all cycles (shaking)	Cycle 5	1.21 ± 0.15	0.71
0.012	0.2, 10	700 in cycle 1, 1000 in later cycles (shaking)	Cycle 7	1.35 ± 0.22	0.51
0.012	0.4, 5	900 in cycle 1, 800 in later cycles (stirring)	Cycle 3	1.28 ± 0.27	0.17
0.012	0.4, 5	1050 in cycle 1, 800 in cycle 2, 600 in later cycles (stirring)	Cycle 3	0.92 ± 0.16	0.16
			Cycle 4	1.54 ± 0.25	0.14
0.0024	0.4, 5	700 (stirring)	Cycle 4	2.18 ± 0.53	0.48

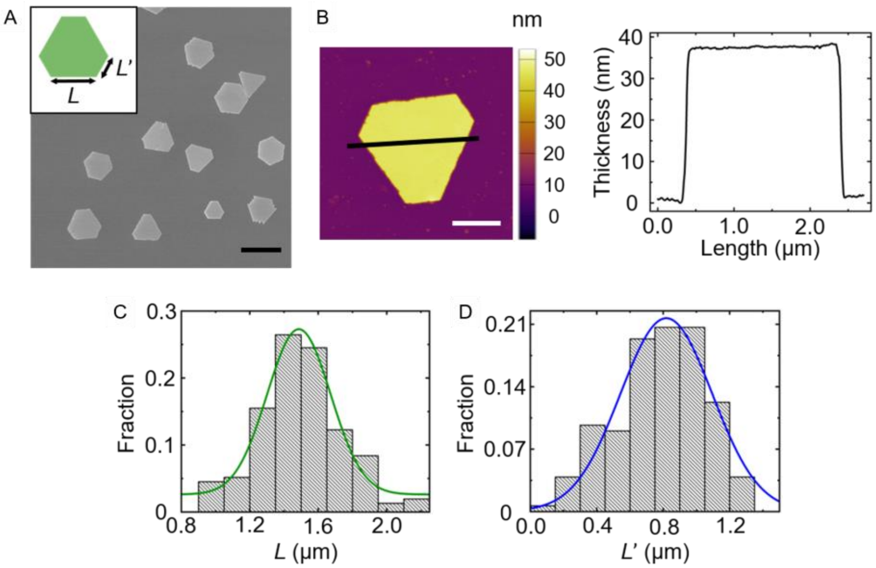

Figure 3.2. Characterization of the anisometric silver plates (long side length L: 1.49 ± 0.24 μm, used for the hexagonal lattice). (A) A SEM image of the anisometric silver plates. The inset is a schematic of a single silver plate labeled with long side length L and short side length L'. (B) (left) A typical atomic force microscopy (AFM) image and (right) the corresponding thickness profile (across the black line in the AFM image) of a representative silver plate. The color bar represents height. (C) and (D) The long and short side length distributions of silver plates measured from SEM images using ImageJ. The green and blue curves are the Gaussian fits. Note that our samples contain in general two size populations as discussed in our previous work:[51] large plates that assemble and small plates that do not participate in self-assembly at our typical experimental ionic strength conditions, due to their much smaller surface area and the consequent weak van der Waals attraction. Similar to our previous work,[51] here the reported side length, thickness and truncation distributions consider only the large plate population that assemble in our experimental conditions. Scale bars: 3 μm in (A), 1 μm in (B). (Reprinted with permission from [50]. Copyright © 2019, Springer Nature.)

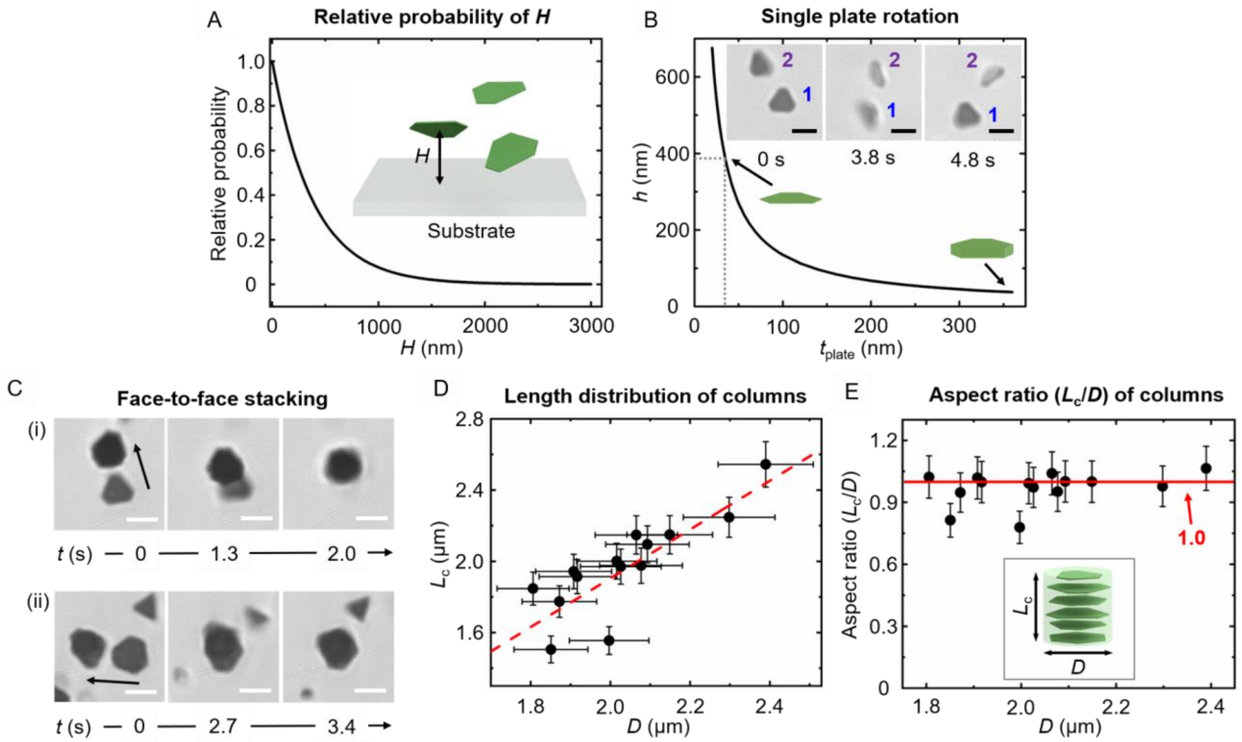

Figure 3.3. The calculation of the fluctuation height of single plates and the optical microscopy characterization of the face-to-face plate stacking into columns. (A) A graph of calculated relative probabilities of plates residing at different heights. The inset schematic shows the plate height H defined as the height of plate center-of-mass from the substrate. (B) A graph of calculated fluctuation height of plates as a function of the plate thickness. The inset schematics show the representative plates of different thickness (not drawn to scale). The thin plate on the left has the same dimension as that used in our hexagonal lattice assembly. The inset time-lapse optical microscopy images show the 3D rotation of two dispersed plates (labelled as "1" and "2") in water. (C) Two sets of time-lapse optical microscopy images showing the plate face-to-face stacking process (indicated by the black arrows). (D) A graph of the length L_c distribution of assembled columns of different overall diameters D (see the inset schematic in (E)). Column lengths are measured from optical microscopy images when the columns are exhibiting out-of-plane rotations. The red dotted line is the linear fit to the data. (E) A graph of the aspect ratio distribution of assembled columns in (D). The column aspect ratio is defined as L_c/D. The horizontal red solid line is at an aspect ratio of 1.0 as the guide for the eye. The error bars in (D) and (E) are from the measurement errors in the optical microscopy images. Ionic strength in (C) to (E): 0.5 mM. Scale bars: 2 μm. (Reprinted with permission from [50]. Copyright © 2019, Springer Nature.)

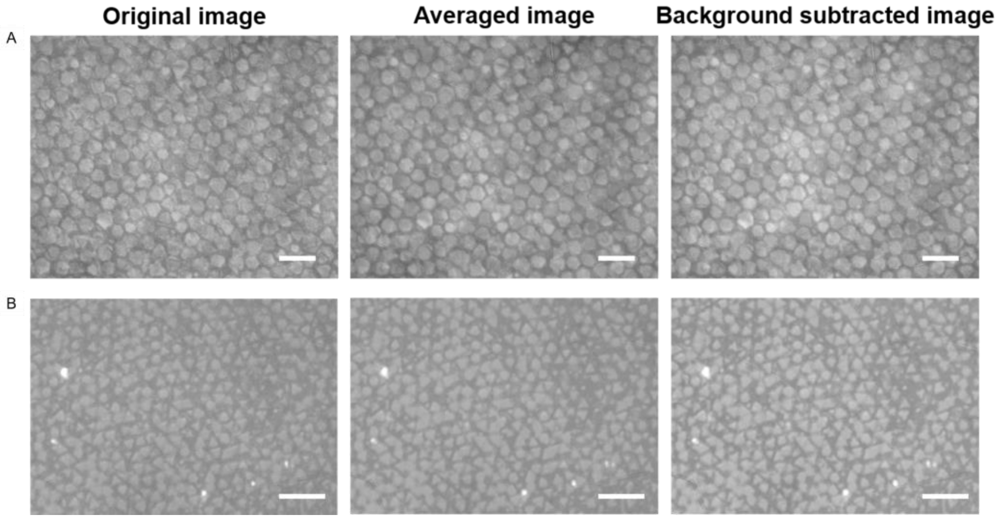

Figure 3.4. The flowchart of image processing procedures. The image processing process illustrated by optical microscopy images including averaging and background subtraction. Scale bars: 5 μm. (Reprinted with permission from [50]. Copyright © 2019, Springer Nature.)

Self-assembly of the dispersed plates was triggered by increasing the ionic strength (0.5 mM NaCl), leading to the formation of standing column secondary building blocks by face-to-face plate stacking (**Figures 3.1B and 3.3C**). The column geometry was verified under optical microscopy, as rotating columns exhibit light, rectangular projections while lying on their sides and dark, polygonal projections while standing vertically on the substrate (**Figure 3.1C**). At this ionic strength, van der Waals attraction (E_{vdW}) between adjacent plates overcomes screened electrostatic repulsion (E_{el}), and because the basal plane has a ~63 times larger interacting area than the plate side, face-to-face stacking into columns is favored over lateral assembly. Specifically, based on the pairwise interaction ($E_{\mathrm{tot}} = E_{\mathrm{vdW}} + E_{\mathrm{el}}$) we computed following a discretized model,[137, 138] the face-to-face stacking as observed in experiments has an E_{tot} minimum of –6.1 $k_{\mathrm{B}}T$ (**Figures 3.1D and 3.5, Table 3.2**), while the side-by-side configuration is not as stable, with a negligible E_{tot} minimum of –0.02 $k_{\mathrm{B}}T$. Face-to-face stacking of plates within the columns was further verified by SAXS, where the measured face-to-face spacing between adjacent plates, the *d* spacing, is consistent with that predicted by both the analytical and discretized models for plate–plate interactions (**Figure 3.6, Table 3.3**). Based on the *d* spacing, one column is composed of ~15 plates (**Figure 3.3D–E**). The column structure was also observed in our earlier work[51] on plates that have a smaller basal plane area (0.90 µm^2, versus 3.27 µm^2 here). The key difference is that, due to their larger basal plane area, the columns in this work experience enhanced van der Waals attraction with the substrate and gravitational force, so the columns prefer to stand vertically on the substrate (**Figure 3.3C**), facilitating the subsequent lateral assembly of columns as secondary building blocks.

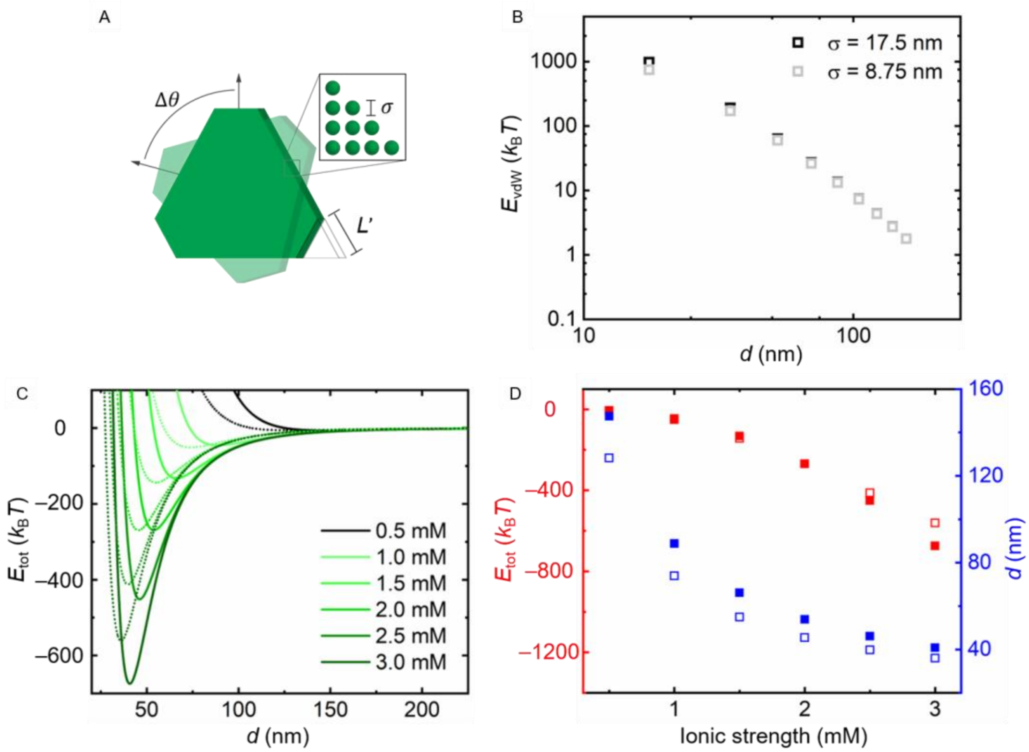

Figure 3.5. Calculations of pairwise interaction and equilibrium interparticle *d* spacing of two face-to-face assembled silver plates using both analytical and discretized models. (A) A schematic showing the discretized model; $\Delta\theta$ is the relative rotation between plates, σ is the size of the discrete "bead," and L' is the extent of tip truncation. (B) The comparison of van der Waals interaction calculation using different bead sizes, which shows consistent results, especially in the experimental interaction range (~50–150 nm). (C) Net pairwise interaction energy of two stacked plates as a function of interparticle *d* spacing at different ionic strength conditions at $\Delta\theta$ = 0º. The solid lines are analytical model calculations and the dashed lines are discretized model calculations. (D) The interaction strength (red) and equilibrium interparticle distance *d* (blue) comparisons between analytical (solid squares) and discretized models (empty squares) at different ionic strength conditions at $\Delta\theta$ = 0º. (Reprinted with permission from [50]. Copyright © 2019, Springer Nature.)

Table 3.2. The parameters used in the plate–plate interaction calculation.

Interaction	Parameter	Value
van der Waals attraction	Hamaker constant (H_0) at zero separation	4.0×10^{-19} J
	plate basal plane area (S)	3.27 μm^2
	plate thickness (t_{plate})	35 nm
electrostatic repulsion	carboxylate–thiol monolayer thickness (t_{ligand})	2.4 nm
	relative permittivity of water (ε)	78.5
	vacuum permittivity (ε_0)	8.854×10^{-12} F m^{-1}
	zeta potential of silver plates[51] (ζ)	−41.9 mV

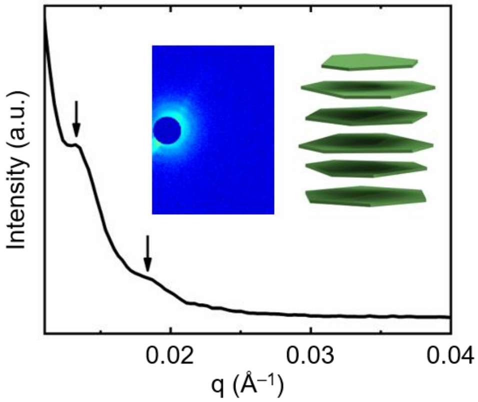

Figure 3.6. Small-angle X-ray scattering (SAXS) spectrum of the column sample when the ionic strength is 0.9 mM. The black arrows indicate the peak positions. The left inset is the corresponding 2D scattering image from SAXS. The right inset is a schematic showing the 1D column structure assembled from plates. (Reprinted with permission from [50]. Copyright © 2019, Springer Nature.)

Table 3.3. The calculated center-to-center d_c spacing value ($d_\mathrm{c} = \frac{2\pi}{q_1}$), peak positions q_1 to q_4, and ratios between higher-order peak positions (q_2 to q_4) and the first-order peak position q_1 in SAXS spectra and the comparison of d_c obtained from SAXS, analytical and discretized models.

Ionic strength (mM)	d_c (nm)	q_1 (Å^{-1})	q_2 (Å^{-1})	$\frac{q_2}{q_1}$	q_3 (Å^{-1})	$\frac{q_3}{q_1}$	q_4 (Å^{-1})	$\frac{q_4}{q_1}$
0.9	142.8	0.0044*	0.0088*	2.0	0.0132	3.0	0.0184	4.2
0.9	130.9	From analytical model						
0.9	117.4	From discretized model						

*These q values were derived based on higher-order peak positions.

The standing columns further assemble as their concentration increases, into an ordered hexagonal lattice due to a size-focusing effect in the columns. This size-focusing effect is a direct result of the plate anisometry. **Figure 3.1E–F** summarizes the overall trend as we tilt the microscopy chamber slightly to concentrate the columns. The Fourier transform of the final equilibrated structure (**Figure 3.1E** inset) reveals a global hexagonal order. Our tracking of adjacent columns in the lattice (traces labeled in **Figure 3.1E**) shows highly localized vibrations at the lattice sites, validating the lattice stability. Two details are noted in the hexagonal lattice formation. First, the plates are polydisperse (about 16% based on L, 34% based on L') because the growth of micron-sized particles from nano-sized seeds is highly susceptible to local fluctuations in solution, as reported previously.[47, 71] This polydispersity is usually considered too high for forming an ordered crystal (for example, less than 12% polydispersity is required for spheres to crystallize).[139] However, the secondary building blocks of columns average their sizes due to plate stacking, thereby rendering them greatly reduced polydispersity (8%) to assemble into ordered lattice (**Figure 3.1B**). Such a size-focusing effect can potentially account for the formation of similar 3D lattices from polydisperse $Al(OH)_3$ nanoplates presented in earlier work, where ensemble structure was characterized by SAXS.[125, 126, 128] This effect which enables ordered assembly from polydisperse building blocks is also reminiscent of the monodisperse supraspheres formed from polydisperse CdSe nanoparticles,[140] but was achieved here *via* hierarchical averaging, not self-limiting clustering which requires an intricate balance of competing forces.[140] Second, the columns are otherwise dispersed at low or intermediate column concentrations (**Figures 3.1F and 3.7**), indicating a weak or negligible attraction between the columns at this ionic strength. The weak attraction is further verified as the columns were observed to diffuse close into contact and then apart due to the absence of strong attraction (**Figure 3.7A–B**), such that they only crystallize into ordered lattice when their concentration is sufficiently high.[141] The ordered hexagonal lattices are observed in multiple plate samples of different sizes (**Figure 3.8**), further demonstrating the robustness of the 3D hierarchical assembly. The 3D nature of the assembled structures is also verified by scanning electron microscopy (SEM) imaging, where layers of plates are clearly shown to stack into laterally interacting columns (**Figure 3.9**).

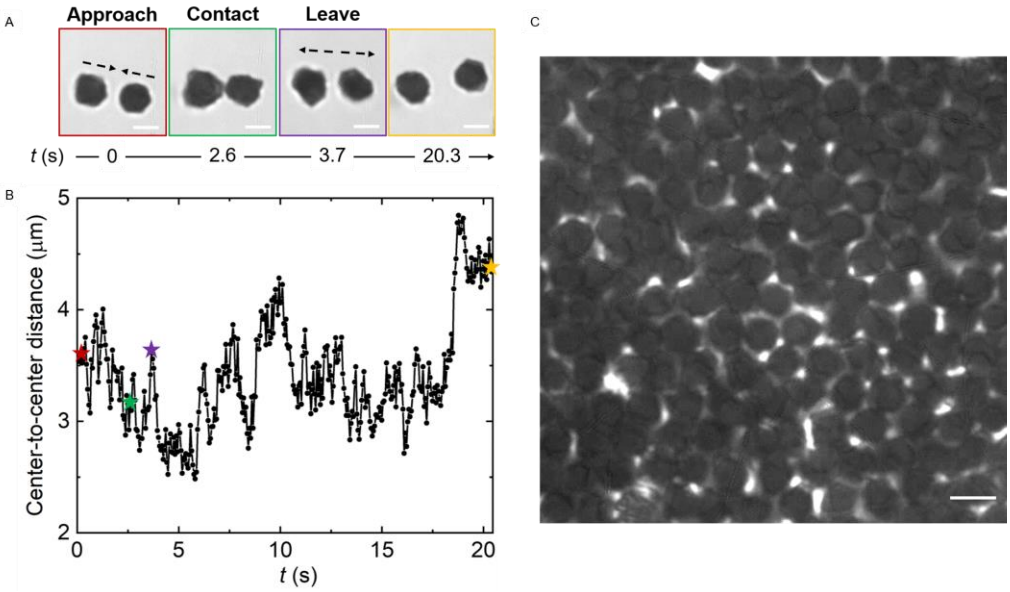

Figure 3.7. Standing columns at low to high column concentrations. (A) Time-lapse optical microscopy images showing a representative column pair diffusing close and then apart due to the absence of strong column attractions at the same ionic strength as in the hexagonal lattice but at a lower column concentration. The black dotted arrows indicate the motion directions of this column pair. (B) A plot showing how the center-to-center distance between the columns in the pair (A) changes over time. The stars indicate the four time points color matched with the boxed images in (A). (C) An optical microscopy image showing the plates at intermediate column concentration. As shown in the image, the empty space (bright regions) between each column helps visualize the stacking and rotation nature of plates in each column, further verifying the 3D structure in the assembly. Ionic strength: 0.5 mM. Scale bars: 2 μm in (A), 3 μm in (C). (Reprinted with permission from [50]. Copyright © 2019, Springer Nature.)

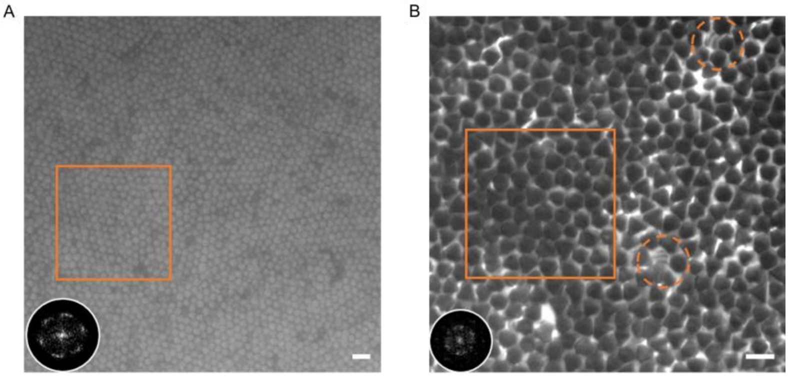

Figure 3.8. Hexagonal lattices assembled from plates of different sizes. (A) An optical microscopy image showing the hexagonal lattice from relatively small plates (long side length L: 1.21 ± 0.15 µm, short side length L': 0.85 ± 0.17 µm; t_{plate}: 46 ± 10 nm, average truncation $\overline{m} = 0.71$). The inset is the corresponding Fourier transform of the image in the orange box. Ionic strength: 0.5 mM. (B) An optical microscopy image showing the hexagonal lattice from large plates at high plate concentration (long side length L: 2.18 ± 0.53 µm, short side length L': 0.93 ± 0.38 µm; t_{plate}: 30 ± 4 nm, average truncation $\overline{m} = 0.48$). The inset is the corresponding Fourier transform of the image in the orange box. The orange circles highlight the stacking nature of the columns when they are slightly tilted. Scale bars: 5 µm. (Reprinted with permission from [50]. Copyright © 2019, Springer Nature.)

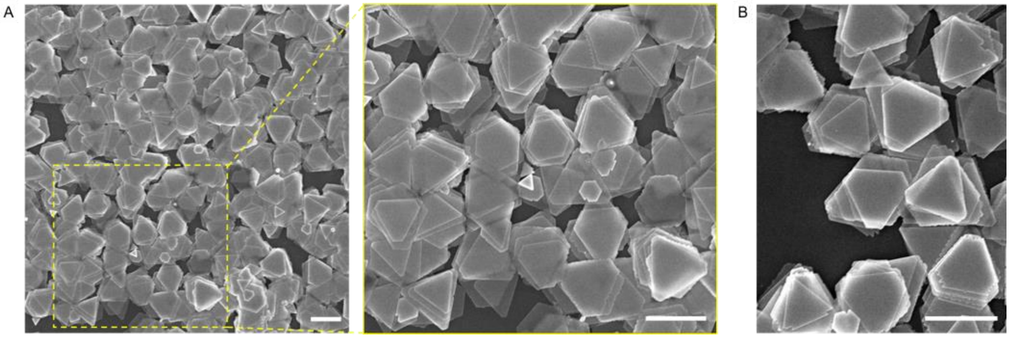

Figure 3.9. SEM images (A) and (B) showing the 3D structures assembled from plates. The SEM images of the assembled 3D lattices after drying in air in the optical microscopy chamber, which show that plates stack face-to-face into columns, and these columns assemble laterally into 3D structures. The plate dimension is: long side length L: 1.35 ± 0.22 µm, short side length L': 0.64 ± 0.24 µm; t_{plate}: 28 ± 5 nm, average truncation $\overline{m} = 0.51$. Scale bars: 2 µm. (Reprinted with permission from [50]. Copyright © 2019, Springer Nature.)

A close investigation into the relative rotations of plates in the columns further reveals how the effective shape of columns is reduced into monodisperse, radially symmetric circular columns. As shown in **Figures 10–12**, the constituent plates in a column rotate relative to each other so that the projections of columns dynamically vary. Plates at the first few layers in the column are clearly identified based on their contrast difference under optical microscopy. The outlined contours of the column projections were color-coded according to the local curvature, which fluctuate to average the triangular plates of different orientations into a circular column projection as quantified in **Figure 10B**. As a result, the effective circular columns pack closely into a hexagonal lattice when concentrated, much like how circular disks crystallize at high disk concentrations.[141] The column projection diameter D was obtained from the center-to-center distance between nearest neighbor columns in the lattice. The measured value is 2.36 ± 0.19 µm, which is close to the diameter of a circle circumscribing an average plate (2.32 µm), indicating that the columns in the lattice are closely packed. The plates in a nearest pair of columns are expected to stay "enveloped" by the circular rims, experiencing little physical contact as they rotate. Indeed, the orientations of two such plates span a range over 120° over time as shown in **Figure 10C**, indicating a full 360° rotation range given the three-fold rotational symmetry of the plate. The Pearson correlation coefficient[34] of the plate orientations (θ_1, θ_2) sampled for n continuous frames, defined as $\frac{\sum \theta_{1f}\theta_{2f} - n\overline{\theta_1}\,\overline{\theta_2}}{\sqrt{(\sum \theta_{1f}{}^2 - n\overline{\theta_1}^2)}\sqrt{(\sum \theta_{2f}{}^2 - n\overline{\theta_2}^2)}}$, is as low as –0.01 ($f$ being the frame number; $n = 300$ here), confirming a weak angular correlation between plates in adjacent columns.

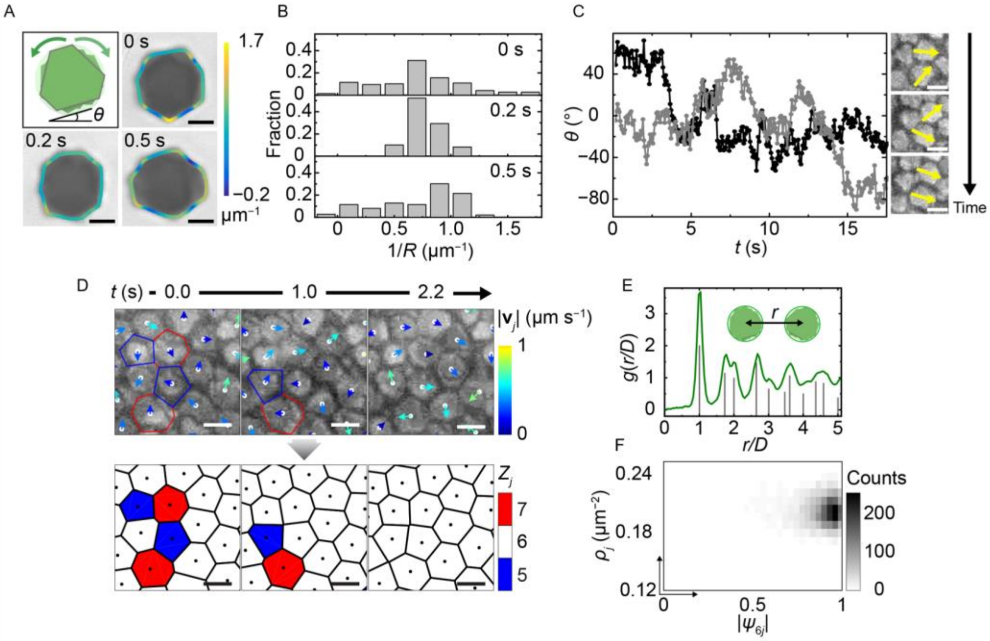

Figure 3.10. Radially symmetric columns assembled from triangular plates. (A) Schematic and time-lapse optical microscopy images of the projections of the same column, overlaid with contour lines color-coded according to the local curvature (the inverse of the locally fitted circle radius R).[137] The color bar represents curvature values. (B) The distribution of local curvature of the projection contours. (C) Orientations of two plates (one in gray, the other in black) in a pair of nearest neighbor columns inside the lattice over time, and time-lapse optical microscopy images with the plate orientations labeled in yellow. The measurement errors are ± 5°. (D) Time-lapse optical microscopy images (top) and corresponding Voronoi cell representations (bottom) of the hexagonal lattice, showing the annealing of imperfectly coordinated sites. The arrows in the top panel are color-coded by the velocity magnitude $|\mathbf{v}_j|$ of columns. The color of each Voronoi cell denotes the number of nearest neighbors Z_j per column j. (E) Radial distribution function of the lattice in experiment (green curve) and that of an ideal hexagonal lattice (gray lines). (F) The local order–local density ($|\psi_{6j}|, \rho_j$) histogram based on single column tracking of the hexagonal lattice. Here $|\psi_{6j}| = |\frac{1}{Z_j}\sum_{k=1}^{Z_j}\exp(6i\beta_{jk})|$, where the summation goes over all the nearest neighbors of column j, and β_{jk} is the angle between the bond linking column j and its kth neighbor and an arbitrary reference axis.[142, 143] Ionic strength: 0.5 mM. Scale bars: 1 μm in (A), 2 μm in (C) and (D). (Reprinted with permission from [50]. Copyright © 2019, Springer Nature.)

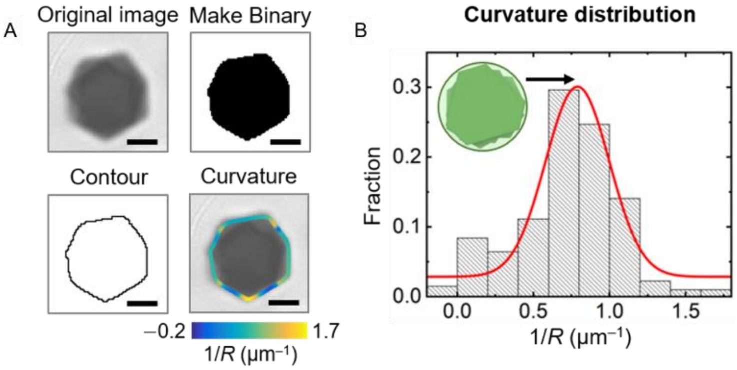

Figure 3.11. Column curvature analysis procedures. (A) From the original optical microscopy image, we used the "Make Binary" function in ImageJ to binarize the image, the "Outline" function in ImageJ to recognize the contour, and the "Wand" function in ImageJ to get the XY coordinates of this contour, which serve as the inputs for the curvature calculation in MATLAB. The color bar represents curvature values. Scale bars: 1 μm. (B) A plot showing curvature distribution of all the column projections at 0 s, 0.2 s and 0.5 s. The red curve is the corresponding Gaussian fit, which gives a $1/R$ value of 0.79 ± 0.03 μm^{-1}. Thus, the radius of the column projection derived from the Gaussian fit is 1.27 ± 0.05 μm, close to the column projection radius measured directly from optical microscopy image (1.18 ± 0.10 μm). (Reprinted with permission from [50]. Copyright © 2019, Springer Nature.)

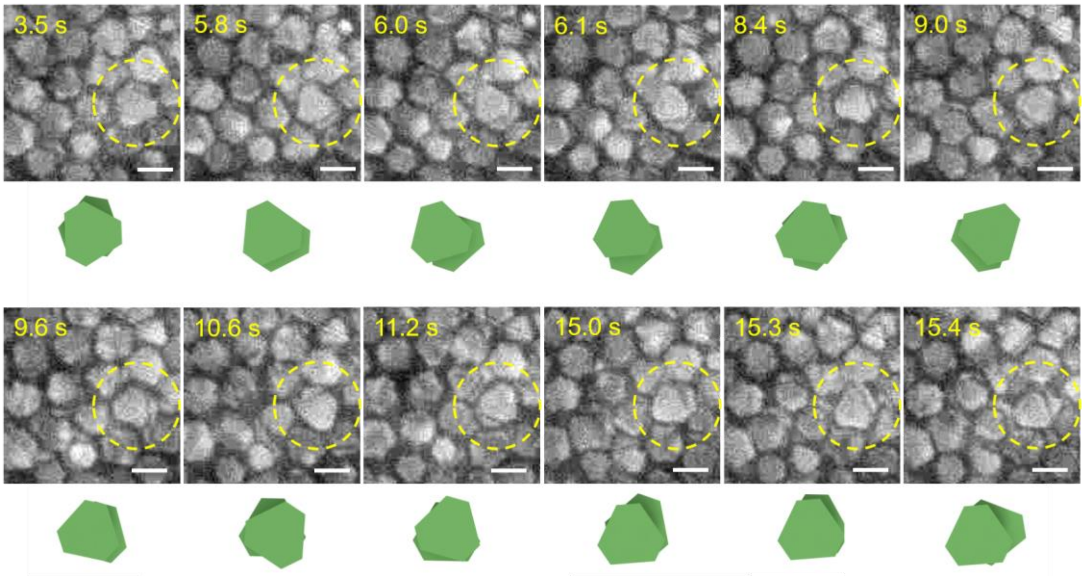

Figure 3.12. Time-lapse optical microscopy images and corresponding schematics showing the visible first- and second-layer plates in the hexagonal lattice. Note that both top and bottom layers experience rotation over the time course shown. Scale bars: 2 μm. (Reprinted with permission from [50]. Copyright © 2019, Springer Nature.)

The tracked column positions and their local motions at the lattice sites reveal not only detailed lattice relaxation dynamics but also a series of parameters characteristic of a hexagonal lattice (**Figure 3.13**). For example, we mapped out the velocity $\mathbf{v}_j$ for each column j (top panel, **Figure 3.10D**) and the Voronoi cell representation of the lattice (bottom panel, **Figure 3.10D**) defining areas specific to each column. This analysis shows the dynamic evolution of imperfectly arranged columns as the number of nearest neighbors (Z_j) reaches to 6 of a perfect hexagonal lattice (**Figure 3.10D**). The radial distribution function[117] $g(r)$ of the column lattice is similar to that of an ideal hexagonal lattice with persisting peaks (**Figure 3.10E**). The calculated six-fold local bond orientation order parameter[142, 143] per column j, $|\psi_{6j}|$, together with the computed local density ρ_j, shows that the columns are both of a high density ρ_j and a high local order $|\psi_{6j}|$ (83% of all the values larger than 0.8 and an average $|\psi_{6j}|$ value of 0.87 over all the columns) (**Figures 3.10F and 3.13E–F**), indicating the high crystallinity of hexagonal lattice from column secondary building blocks.[142]

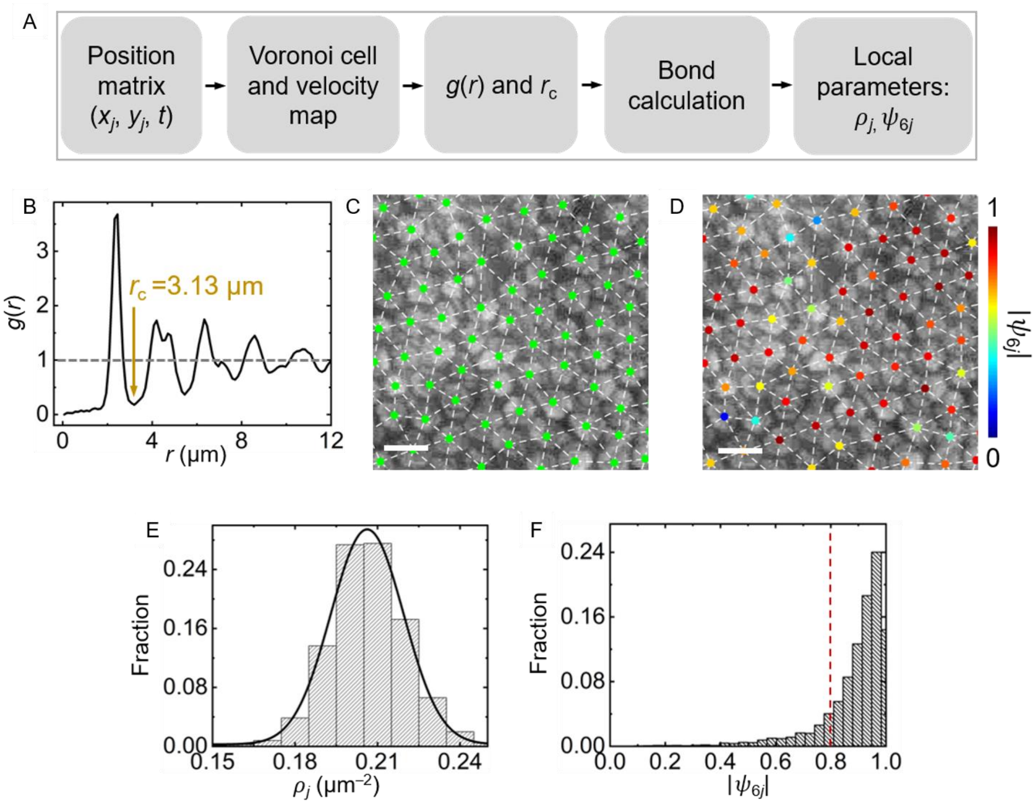

Figure 3.13. The flowchart of the analysis procedure for the hexagonal lattice. (A) A workflow showing the whole analysis procedure. (B) Radial distribution function $g(r)$ calculated based on column positions by accumulating over 32 frames. A cutoff value r_c = 3.13 μm is measured from the first minimum after the first peak position (see the arrow). This cutoff value is used to determine if two columns are connected as nearest neighbors. (C) Bond network overlaid with the original optical microscopy image. (D) The optical microscopy image overlaid with bond network and the tracked center positions (dots color-coded according to the local order parameter $|\psi_{6j}|$ values). (E) Local density ρ_j distribution and (F) local structural order parameter $|\psi_{6j}|$ distribution over 32 frames. A Gaussian fit (black curve in (E)) to the local density distribution gives a peak position of 0.21 μm^{-2} (R^2 = 0.997), which is the same as the local density of a column in a hypothetical hexagonal lattice composed of closely packed circles circumscribing an average plate. Scale bars: 3 μm. (Reprinted with permission from [50]. Copyright © 2019, Springer Nature.)

Having elucidated that the circular shape of columns leads to hexagonal lattices, we next demonstrated that the effective shape of columns can be controlled by changing the ionic strength or the extent of plate tip truncation, potentially leading to different lattice structures. Here we define a parameter m as the ratio between the short (L') and the long (L) side lengths of a plate, to quantify the extent of tip truncation. As shown in both the schematics and SEM images (**Figure 3.14A**), an m value of 0 corresponds to a triangular plate with sharp tips and 1 to an equilateral hexagonal plate. Regarding the ionic strength effect, given the same type of plates as studied above (the plates that are assembled into a hexagonal lattice), we calculated the interactions E_{tot} between a stacked plate pair with varying relative in-plane orientations $\Delta\theta$ at their energy minimum spacings, as a function of ionic strength (**Figure 3.14A–B**). At a relatively low ionic strength (0.5 mM, the experimental condition for forming hexagonal lattice), E_{tot} is weakly dependent on $\Delta\theta$ over a range of –60° to 60°. Based on a Boltzmann distribution argument (relative probability, $p_{\mathrm{rel}}(\Delta\theta) \approx e^{-\Delta E/k_{\mathrm{B}}T}$, where ΔE is the E_{tot} difference for two plates at different relative orientations, see **Figure 3.14C**), large plate–plate relative rotations are allowed with low energy penalty. This prediction is also consistent with our experimental observations of fast relative rotations of plates at this ionic strength condition (**Figure 3.10A–B**). The interaction profile becomes increasingly steeper with respect to plate relative rotation as ionic strength increases, restraining the relative rotations between adjacent plates so that the plates within the columns favor aligned orientations (**Figure 3.14C**). We verified this trend in experiments at high ionic strength (2.0 mM). At this ionic strength, the electrostatic repulsion is more screened, leading to a decreased separation between plates in the columns, higher enthalpic penalties for plate relative rotation, and therefore dampening of plate relative rotations as well as a significant increase in the lateral attraction between columns. Irregular, fractal-like assemblies from columns were observed from the same plate sample at high ionic strength (2.0 mM, **Figure 3.15**). In addition, plate tip truncation also drastically changes the allowed relative rotations of plates and thus the effective shape of columns. For pairwise interaction E_{tot} calculated at a constant ionic strength and a constant basal plane area, but at varying m, we find a more hexagonal shape (a larger m) renders a flatter interaction profile over different $\Delta\theta$ values (**Figure 3.14D–E**). The plates with a more triangular shape (a smaller m), on the other hand, have a steeper potential well disfavoring relative rotations between plates. This interaction profile, on the column level, maintains the generic three-fold symmetry of triangular plates instead of a smeared-out circular shape. This detail of tip truncation was not recognized in previous literature,[51] due to the lack of importance in inter-column interactions in those systems.

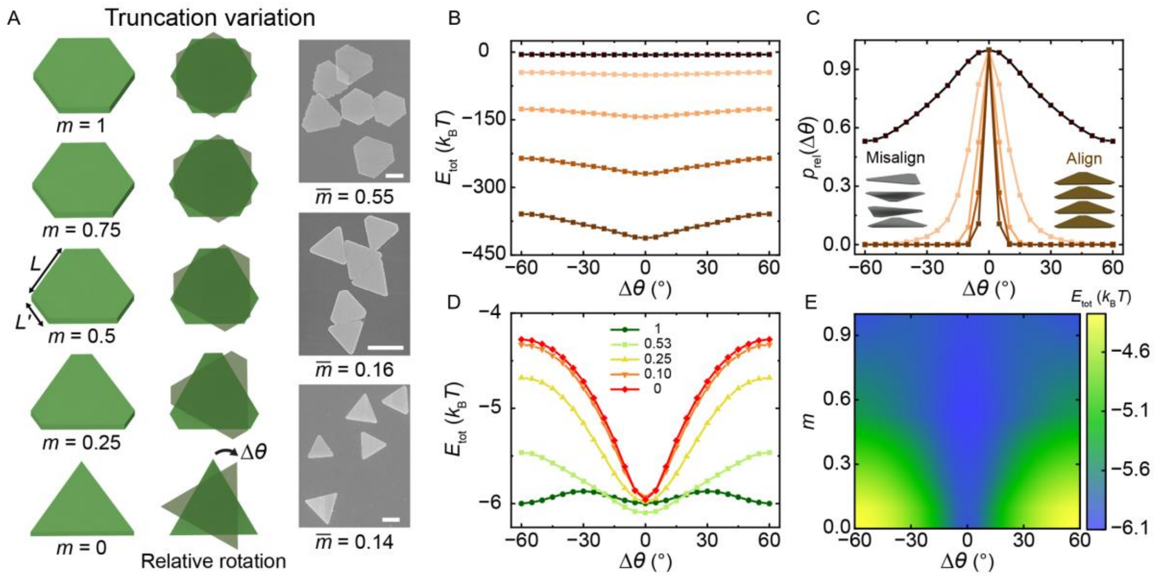

Figure 3.14. The effective shape of columns modulated by ionic strength or plate tip truncation. (A) Schematics (left) and SEM images (right) showing plates of a systematically varying extent of truncation m (defined as L'/L). The top right SEM image shows the plates used in the hexagonal lattice. The corresponding truncation distributions are shown in **Figure 3.16**. Scale bars: 1 μm. (B) A graph showing how the computed pairwise interaction E_{tot} between two stacked plates (m = $\overline{L}'/\overline{L}$ = 0.53, corresponding to the plates used for hexagonal lattice) changes as a function of $\Delta\theta$ at different ionic strengths (from top to bottom: 0.5 mM, 1 mM, 1.5 mM, 2 mM, 2.5 mM, respectively). Note that 0.5 mM is used in the hexagonal lattice assembly. (C) Relative probability distributions of $\Delta\theta$ based on a Boltzmann distribution argument at different ionic strengths, computed from the interaction energy plot in (B). The inset schematics show misaligned plate orientations inside column (left) at low ionic strength (0.5 mM) and well-aligned plate orientations (right) at high ionic strength (2.5 mM). (D) A graph showing how the computed pairwise interaction E_{tot} between two stacked plates changes as a function of $\Delta\theta$ at different extent of truncation m as labeled. Here the calculations are conducted at fixed basal plane area (3.27 μm^2). Ionic strength: 0.5 mM. (E) Pairwise interaction strength as a function of $\Delta\theta$ and truncation m, at their energy minimum spacing *d*. Ionic strength: 0.5 mM. (Reprinted with permission from [50]. Copyright © 2019, Springer Nature.)

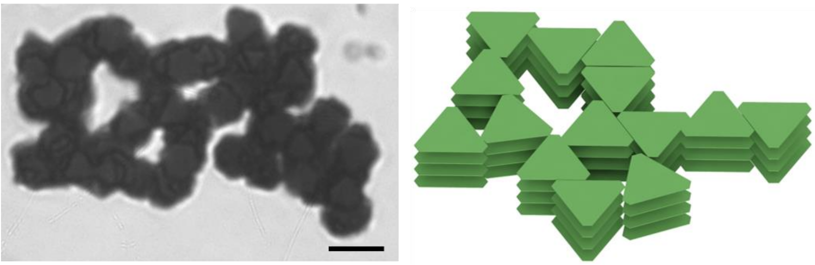

Figure 3.15. A representative optical microscopy image showing irregular assemblies of columns at high ionic strength (2.0 mM). The plate sample here is the same sample (average truncation $\overline{m}$ of 0.55) used for the hexagonal lattice. Scale bar: 3 μm. (Reprinted with permission from [50]. Copyright © 2019, Springer Nature.)

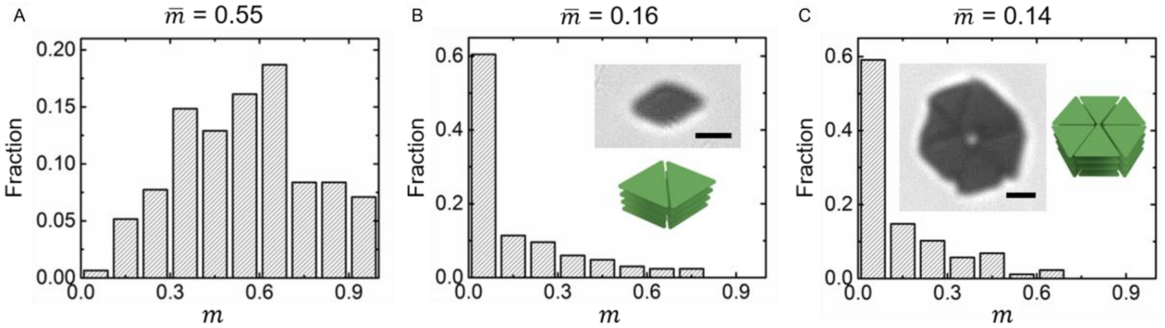

Figure 3.16. The distributions of the extent of truncation (m) of the three types of plates whose SEM images were shown in **Figure 3.14A**. (a) The plates of an average truncation $\overline{m}$ of 0.55, which are used for the hexagonal lattice assembly. (b) The plates of an average truncation $\overline{m}$ of 0.16. The inset is an optical microscopy image and the corresponding schematic of an assembled structure ("dimer") at 7 mM ionic strength. (c) The plates of an average truncation $\overline{m}$ of 0.14. The inset is an optical microscopy image and the corresponding schematic of an assembled structure ("hexamer") at 4 mM ionic strength. Scale bars: 1 μm. (Reprinted with permission from [50]. Copyright © 2019, Springer Nature.)

Finally, we experimentally realized the triangular columns predicted above, and in doing so observed a different final assembly: honeycomb, not hexagonal, lattice domains are formed upon decreasing the extent of plate tip truncation and increasing the ionic strength (**Figure 3.17A**). We synthesized less truncated triangular plates while maintaining anisometry ($\overline{m}$ = 0.17, **Figures**

3.17A and 3.18). As shown in **Figure 3.17B**, these plates assemble into columns at increased ionic strengths (3.2–3.5 mM). The column projections are mostly triangular, with the contoured local curvature distributions staying roughly constant over time (**Figure 3.17B**). Such distributions suggest that the stacked plates within the columns remain aligned, with negligible relative plate rotation. This observation is consistent with our interaction modeling (**Figure 3.17E**), which shows that even a small relative plate rotation of 20º can be strongly disfavored due to an interaction energy penalty as high as 3 $k_{\mathrm{B}}T$. The disfavoring of plate misalignment in the columns leads to a triangular column projection, which encodes an assembly symmetry distinct from the isotropic, circular ones studied above. At low column concentration, the triangular columns assemble side-by-side into small clusters *via* individual plate or column addition (see "hexamer" formation in **Figure 3.17C**), indicating a directional attraction between columns that is strong enough to hold them together once coming close. At high column concentration, the elementary side-by-side attachment extends to 3D honeycomb lattice domains (**Figure 3.17D**).

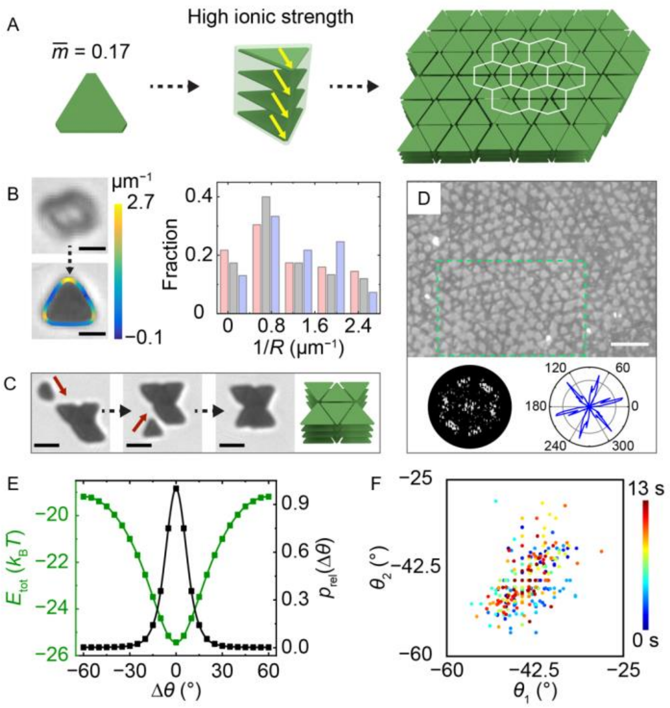

Figure 3.17. Experimental observation of plates assembling into 3D honeycomb lattice domains. (A) Schematics showing the hierarchical self-assembly process. The plates here have the dimensions, L: 1.28 ± 0.27 µm; L': 0.19 ± 0.19 µm; t_{plate}: 22 ± 2 nm; $\overline{m}$ = 0.17. The yellow arrows denote the aligned plate orientations in the column. (B) Time-lapse optical microscopy images (left) showing the lying and standing orientations of the same rotating column. The bottom image is overlaid with contours color-coded according to local curvature. The color bar represents curvature values. The right plot shows the local curvature distributions of the standing column projection contours over time (pink: 0 s; grey: 1 s; purple: 1.5 s). Ionic strength: 3.2 mM. (C) Time-lapse optical microscopy images and schematic showing the assembly process of the columns into a “hexamer”. (D) An optical microscopy image of the assembled lattice with multiple ordered honeycomb domains. The image was processed following details in **Figure 3.4**. The bottom left image is a Fourier transform of one honeycomb lattice domain in the green box. The bottom right plot is an orientation distribution map of the plates in the same lattice domain. (E) Pairwise interaction (green curve) and relative probability distribution normalized to $\Delta\theta$ = 0º (black curve) of the two stacked plates as a function of plate relative orientation $\Delta\theta$. (F) A scatter plot showing the orientations of two plates in a nearest neighbor pair in the honeycomb domain over time. Each data point color corresponds to a different time. The measurement errors are ± 2°. The color bar represents time. Ionic strengths in (C) to (F): 3.5 mM. Scale bars: 1 µm in (B), 2 µm in (C), 5 µm in (D). (Reprinted with permission from [50]. Copyright © 2019, Springer Nature.)

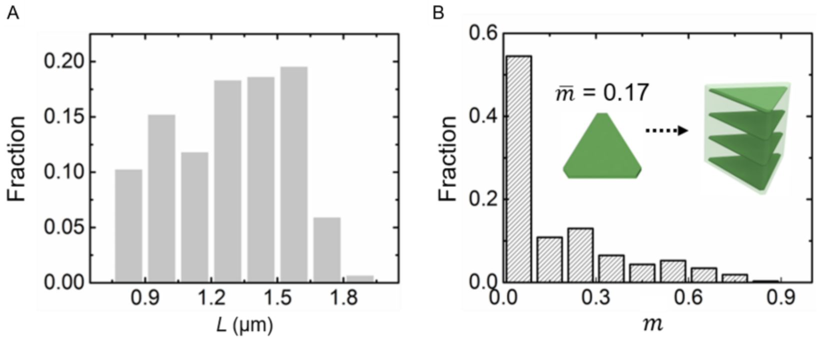

Figure 3.18. Characterization of slightly-truncated silver plates used in **Figure 3.17** (long side length L: 1.28 ± 0.27 μm, average truncation $\bar{m}$ = 0.17) for the assembly of honeycomb domains. (A) The long side length distribution of plates measured from SEM images. (B) Truncation distribution of plates measured from SEM images. The inset schematics show a triangular column formation. (Reprinted with permission from [50]. Copyright © 2019, Springer Nature.)

In comparison with the previous hexagonal lattice, the honeycomb lattice domains exhibit high orientational order and positively correlated plate rotation in a nearest neighbor pair of columns. The first-layer plate orientation distributions (by measuring the orientations of the three sides of a plate) show a six-fold orientational order (bottom right plot in **Figure 3.17D**), consistent with a honeycomb lattice. The two plates in a nearest neighbor column pair have greatly hindered rotations that are positively correlated (a Pearson correlation coefficient of 0.51, **Figure 3.17F**), which suggests side-by-side arrangements. Furthermore, upon an ionic strength decrease from 6 mM to 2 mM in a similarly truncated plate system ($\bar{m}$ = 0.16), we observed a transition from the space-filling honeycomb lattice composed of triangular columns to a loosely packed structure which exhibits hexagonal packing due to increased electrostatic repulsion and lowered penalty for relative plate rotation (**Figure 3.19**). Such precise control of the final 3D lattice structures arises from the effective shape and consequent coordination symmetry of the column secondary building blocks. Anisometry in the plates drives 3D hierarchical assembly, which proceeds one step at a time and enables engineering of the intermediate product, a strategy molecular crystal engineering adopts to obtain a rich library of crystal structures.[134] Control experiments on the 2D assembly of silver plates at different plate concentrations did not show ordered structure formation (**Figure 3.20**).

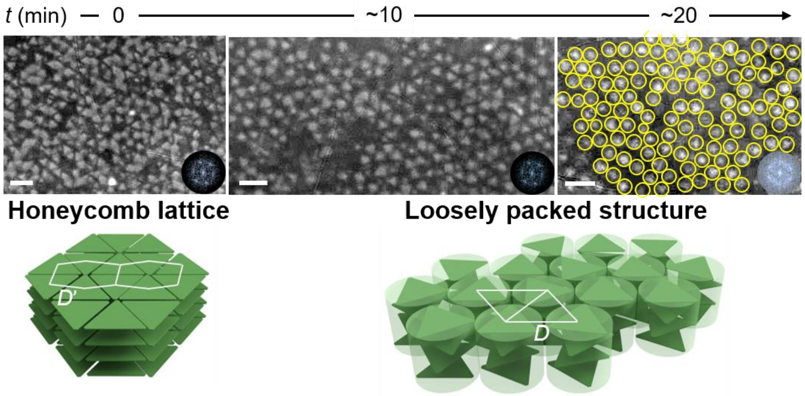

Figure 3.19. The transition from honeycomb domains to a loosely packed structure upon an ionic strength decrease. Time-lapse optical microscopy images and schematics showing this transition from honeycomb domains to a loosely packed structure which exhibits hexagonal packings upon a decrease in ionic strength from 6.0 mM to 2.0 mM. The rightmost image was overlaid with yellow circles to highlight the column positions. The honeycomb domains at 6 mM are stable up to days. The insets in each image are the corresponding Fourier transform of the images. The center-to-center distance between nearest column pairs measured from the optical microscopy images changes from 0.70 ± 0.09 µm (0 min) to 1.07 ± 0.11 µm (~20 min). The plates are the same as shown in the middle SEM image of **Figure 3.14A** (long side length L: 0.92 ± 0.16 µm, short side length L': 0.12 ± 0.12 µm; t_{plate}: 22 ± 2 nm, average truncation $\overline{m}$ = 0.16). Scale bars: 2 µm. (Reprinted with permission from [50]. Copyright © 2019, Springer Nature.)

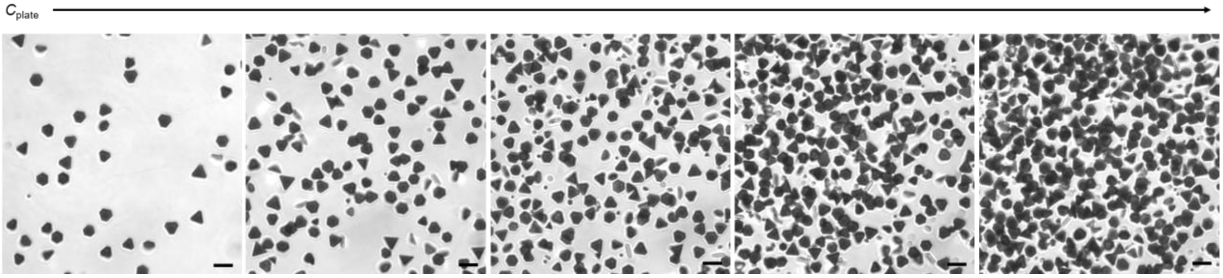

Figure 3.20. 2D assembly of one layer of large plates. Optical microscopy images showing the 2D assembly at different plate concentrations in water, which did not show ordered structures. The plates have long side length L: 2.18 ± 0.53 μm, short side length L': 0.93 ± 0.38 μm; t_{plate}: 30 ± 4 nm, average truncation $\overline{m}$ = 0.48. Due to their large size, these plates mostly stay parallel with the substrate as one layer. Scale bars: 5 μm. (Reprinted with permission from [50]. Copyright © 2019, Springer Nature.)

Conclusions

In summary, in our study of anisometric colloidal self-assembly, two otherwise separated length scales merge to induce 3D hierarchical self-assembly. Fundamentally the anisometry encodes highly directional interactions and induces the formation of secondary building blocks, which enable the selection of final structures from polymorphs over an otherwise complicated free energy landscape. Beyond the conventional small molecular ligands used here, macromolecular shelling[37] or ligands that are responsive to external fields[48, 144] can also be introduced to the anisometric colloids to render patchy interactions or non-equilibrium assemblies, thereby aiding self-assembly into further complicated 3D superstructures. The colloidal shapes as well as the basic quantum-confinement properties can have rich variations. For example, star-shaped or other polygonal[145] basal planes have architecture-dependent plasmonic coupling which can be potentially modulated in the form of 3D arrays as optoelectronic devices.[146] Remarkably, our experimentally observed 3D hierarchical lattices are different from those adopted by simulated triangular prisms, which only form into honeycomb lattices due to hard-core exclusion,[147] yet resembling those simulated for high aspect-ratio circular disks.[148, 149] The combination of positional order and orientational disorder we observed is reminiscent of molecular systems.[150, 151] For example, plate-like molecules can stack into columnar phases[150] to harness longitudinally-favored charge conduction paths and show greater conductivity along the columns than in the perpendicular direction.[152] Molecules such as boron-containing “connectors” or hydrocarbon “linkers” can form into covalent organic frameworks, with cage architecture and rotational order developed upon a delicate balance between intermolecular attraction (van der Waals, π-π stacking) and electrostatic repulsion.[151] The formation of covalent organic frameworks is similar to the formation of our honeycomb lattice from triangular plates, upon a balance of interparticle interactions. The real-time dynamics observed here can potentially provide insight into phenomena taking place in those molecular systems.

Methods

Synthesis of Anisometric Silver Plates. The silver plates of controlled extent of truncation were synthesized following a slightly modified seeded-growth method.[47, 51] Silver seeds were prepared by adding 25 mL $AgNO_3$ (0.1 mM), 600 μL sodium citrate (75 mM), and 60 μL hydrogen peroxide (30 wt %) in sequence to a 125 mL Erlenmeyer flask stirring at 300 rpm at room temperature. Next the stirring speed was increased to 1050 rpm before rapid injection of 250 μL freshly prepared aqueous $NaBH_4$ solution (0.1 M). This $NaBH_4$ solution was prepared by adding solid $NaBH_4$ to water which had been precooled in an ice bath for ~10 min and then vortexing immediately. The obtained light yellow solution turned blue about 4–10 min after the injection of the $NaBH_4$ solution and was kept stirring for another 5 min after this color change. Then the mixture was centrifuged (Eppendorf Centrifuge 5804) at 10,500 rpm for 8 min and most of the supernatant was carefully removed, leaving ~50 μL sediment. This sediment was redispersed in 10 mL 0.94 mM sodium citrate solution as the seed solution. A UV–vis spectrum of the as-prepared seeds was measured using a Scinco S-4100 PDA spectrophotometer. In different batches of seed preparation, the extinction peak positions were at 700–800 nm. Based on the UV–vis spectrum, we diluted the seed solution using 0.94 mM sodium citrate solution to a concentration with an extinction intensity of 0.012 or 0.0024 at the maximum peak position; this diluted solution was later used as our seed solution stock to grow silver plates. All the parameters used in silver plate growth (different size and different extent of truncation m) are listed in **Table 3.1**. Below are the synthesis details of the two typical types of plates for which we studied self-assembly behavior. For plates with $\overline{m}$ = 0.55, 0.75 mL of L-ascorbic acid (0.1 M) was added to 20 mL of the seed solution stock kept in a 40 mL glass vial (Fisherbrand, 29 mm × 94 mm) as growth solution I. At the same time, a separate growth solution II was prepared by mixing 20 mL $AgNO_3$ (1.0 mM), 125 μL citric acid (0.1 M), and 100 μL sodium citrate (1.5 mM). Growth solution II was added to growth solution I dropwise through a syringe pump (Fusion 200, Chemyx Inc.) at a rate of 0.2 mL min^{-1} to start the plate growth. During the growth process, the growth solution was shaken vigorously at room temperature at a speed of 700 rpm for the first cycle and 1000 rpm for the later cycles (Eppendorf, ThermoMixer C). After every 10 min of injection, which is one growth cycle, two-thirds of the growth solution in the vial was removed, and the remaining solution was used for the next growth cycle to grow larger plates. The solution removed after growth cycle 5 was collected and stored in 8 mL glass vials (Wheaton, borosilicate glass, 17 mm × 60 mm) for further thiol modification. For plates with $\overline{m}$ = 0.17, all the procedures and reactant concentrations are the same as above, except that (i) during the plate growth, the growth solution was kept stirring vigorously at a speed of 900 rpm for the first cycle and 800 rpm for the later cycles; (ii) the injection rate of growth solution II was 0.4 mL min^{-1}, with 5 min injection as one growth cycle; and (iii) plates after growth cycle 3 were collected and used for thiol modification.

Thiol Modification of Silver Plates. The silver plates obtained above were coated with citrate ligands. These ligands were exchanged with carboxylate–thiols ($HS(CH_2)_{11}(OC_2H_4)_6OCH_2COOH$) to improve colloidal stability in solution. Specifically, 100–200 μL, 7.93 mM thiol solution was added to 2 mL silver plate solution collected from the growth cycle. This 7.93 mM thiol solution was prepared by dissolving 5 μL thiol as received from Prochimia in 1 mL water. The reaction solution was then allowed to sit overnight without stirring to complete the ligand exchange. After that, the plates with exchanged ligands sediment to a thin layer at the bottom of the vial. The supernatant was carefully removed, and 2 mL water was added to the sediment. After 5 h of additional sedimentation, the supernatant was removed and the final sediment product was stored in water in an 8 mL glass vial.

Plate Characterization. The shape and size distribution of silver plates, and the assembled 3D lattice structures were characterized using SEM (Hitachi S4800). The plate thickness was measured using either tapping-mode AFM (Asylum Research Cypher) or SEM when the plates were vertical to the viewing angle. The silicon wafer used in the AFM measurement was first sonicated with acetone and isopropanol each for 15 min, and then treated with oxygen plasma (Harrick Plasma Cleaner PDC-23G) at medium power for 1 min to render the wafer surface hydrophilic. Then one drop of silver plate solution (~5 μL) was pipetted on the wafer and allowed to dry under ambient conditions before the AFM measurements. The 3D lattice structures formed in solution in the optical microscopy chamber were controllably dried in the chamber under ambient conditions, to maximally maintain the structure for SEM imaging.

Optical Microscopy Imaging. Approximately 150 μL silver plate suspension after thiol modification was added to an 8-well chamber (composed of a 0.13–0.17 mm thick cover slip with plastic walls, Chambered Coverglass, Thermo Scientific). Bright-field optical microscopy imaging was performed using a Zeiss inverted microscope (Axiovert 200) with 100× oil objective (NA = 1.45) and 1× or 1.6× post magnification. Optical microscopy images were recorded using a complementary metal–oxide–semiconductor camera (Edmund Optics 5012 M GigE) at a rate of 17.2 or 21.8 frames per second (fps).

SAXS Measurements. SAXS measurements were conducted on the truncated plate sample ($\overline{m}$ = 0.55) to confirm that plates stack face-to-face into columns and to measure the equilibrium plate-to-plate spacing between adjacent plates in the columns at certain ionic strengths. Specifically, the columns were prepared by adding salt to a concentrated plate suspension to an ionic strength that induces self-assembly (0.9 mM). Next, SAXS samples were prepared by gently transferring 100 μL as-prepared columns at the desired ionic strength into a quartz capillary (1.5 mm outer diameter, 0.01 mm wall thickness, Hampton Research), which was then sealed with poly(tetrafluoroethylene) tape to prevent any evaporation. We waited for 3 h for the sample to equilibrate at the bottom of the capillary. Right before the SAXS measurement, the capillary was gently shaken a few times to disperse the concentrated columns uniformly at the bottom of the capillary. Transmission SAXS spectra were collected for 10–30 min using a home-built setup (Forvis Technologies, Santa Barbara) with a Xenocs GeniX3D Cu Kα ultralow divergence X-ray source (1.54 Å/8 keV) with a divergence of ~1.3 mrad and a Pilatus 300 K 20 Hz hybrid pixel detector (Dectris). FIT2D (from European Synchrotron Radiation facility, http://www.esrf.eu/computing/scientific/FIT2D) was used to analyze the two-dimensional (2D) scattering plots and obtain the intensity (I) and scattering vector (q) profile (**Figure 3.6**). The fact that q values in the SAXS spectra are integer multiples indicates a 1D lamellar structure[51] (see **Table 3.3**). Due to the large plate-to-plate spacing of the assembled chains, the first two peaks (those with q values less than 0.01 Å^{-1}) were overwhelmed by the profile of the unscattered beam.

Consequently, the q values of the first two peaks were derived from higher-order peaks (**Table 3.3**). The equilibrium center-to-center distance between neighboring plates in the columns, d_{c}, was calculated based on the derived first-order peak position (q_1) as $d_{\mathrm{c}} = \frac{2\pi}{q_1}$.

Analytical Modeling of Pairwise Interactions. In **Figure 3.1D**, the pairwise interaction $E_{\mathrm{tot}}(d)$ was evaluated as a sum of van der Waals attraction[13] between silver in water and electrostatic repulsion between charged ligands,[30] $E_{\mathrm{tot}}(d) = E_{\mathrm{vdW}}(d) + E_{\mathrm{el}}(d)$, where

$$E_{\mathrm{vdW}}(d) = -\frac{H_{\mathrm{eff}}S}{12\pi}\left[\frac{1}{(d)^2} - \frac{2}{\left(d+t_{\mathrm{plate}}\right)^2} + \frac{1}{\left(d+2t_{\mathrm{plate}}\right)^2}\right] \tag{1}$$

and

$$E_{\mathrm{el}}(d) = \frac{\varepsilon\varepsilon_0\zeta^2 S}{b}\left[1 - \tanh\left(\frac{d-2t_{\mathrm{ligand}}}{2b}\right)\right]. \tag{2}$$

Here, d is the face-to-face spacing between two neighboring plates, t_{plate} is the plate thickness, and S is the plate basal plane area. In the electrostatic potential, ε is the relative permittivity of water, ε_0 is the vacuum permittivity, ζ is the zeta potential of the thiol-coated silver plates in water, and b is the Debye length, given (in nanometers) for an aqueous solution of sodium chloride salt as $b = \frac{0.304}{\sqrt{I}}$ for ionic strength I (in moles per liter). In addition, t_{ligand} is the thickness of the carboxylate–thiol monolayer on the plate surface.[30] Here we assumed that the two plates are in a perfectly aligned, face-to-face configuration. Because the plates in this system achieve large interparticle separations, the Hamaker constant was treated as an “effective” Hamaker constant in such a way that the retardation of the van der Waals attraction at large separations is accounted for. In other words,

$$H_{\mathrm{eff}} = \frac{H_0}{1+\frac{ad}{\lambda}} \tag{3}$$

Here a is constant describing the geometry of the interaction (a = 5.3 for two surfaces, a = 11 for two spheres, and $a = 14$ for a sphere and a surface) and λ is parameter describing the onset length scale for retardation. H_0 is the Hamaker constant for silver and silver interacting across water at zero separation (4.0×10^{-19} J).[153, 154] This model was previously shown to be a simple but robust approximation for more complicated retardation theories.[138, 155] The value of λ can be approximated by

$$\lambda = \frac{hc}{\Delta E} \tag{4}$$

where h is Planck's constant, c is the speed of light, and ΔE is a "characteristic energy" in the electronic spectrum of the material, commonly taken to be the first ionization energy. For silver, λ is therefore about 164 nm. Net interaction potentials and the locations of their secondary minima at different ionic strength conditions are indicated in **Figure 3.5**, as calculated using the values in **Table 3.2**.

Discretized Modeling of Pairwise Interactions. The interaction models discussed above do not account for the relative rotation of the plates perpendicular to the column axis. Therefore, we also constructed a coarse-grained (CG), pairwise interaction model to evaluate the effect of relative plate rotation on the interaction potential. Anisometric plates were discretized as N = 21392 to 26744 beads per plate (depending on the extent of truncation) with beads 17.5 nm in diameter (**Figure 3.5A**). Beads were treated as point-like particles, whose van der Waals and electrostatic interactions can be described as:

$$e_{\mathrm{vdW}}(r_{\mathrm{bead-bead}}) = \frac{-H_{\mathrm{eff}}\sigma^6}{\pi^2 r_{\mathrm{bead-bead}}^6} \tag{5}$$

and

$$e_{\mathrm{el}}(r_{\mathrm{bead-bead}}) = \frac{{Z_{\mathrm{bead}}}^2 e^2}{4\pi\varepsilon\varepsilon_0 r_{\mathrm{bead-bead}}} \mathrm{e}^{-r_{\mathrm{bead-bead}}/b} \tag{6}$$

where $r_{\text{bead-bead}}$ is the distance between beads in a pair, σ is the bead size, and the remaining variables have the same meaning as in the above analytical modeling.[137, 138] The charge of a bead, Z_{bead}, was approximated first by calculating the surface charge density, ρ_{surf}, based on the zeta potential, using the Grahame equation:[156]

$$\rho_{\text{surf}} = \sqrt{8I\varepsilon\varepsilon_0 RT}\,\sinh\left(\frac{e\zeta}{2k_{\text{B}}T}\right) \tag{7}$$

finding the total charge of the plate surface, and then dividing this charge across all N beads. The van der Waals interaction between anisometric plates was taken as the sum of all bead–bead van der Waals interactions, *i.e.*,

$$E_{\text{vdW}}^{\text{CG}}(d) = \sum_{i=1}^{N}\sum_{j=1}^{N} e_{\text{vdW}}(r_{\text{bead-bead}}) = \sum_{i=1}^{N}\sum_{j=1}^{N} \frac{-H_{\text{eff}}\sigma^6}{\pi^2\left|\mathbf{r}_i-\mathbf{r}_j\right|^6} \tag{8}$$

for beads i in one plate and beads j in the other. Similarly, the plate–plate electrostatic interaction was evaluated as

$$E_{\text{el}}^{\text{CG}}(d) = \sum_{i=1}^{N}\sum_{j=1}^{N} e_{\text{el}}(r_{\text{bead-bead}}) = \sum_{i=1}^{N}\sum_{j=1}^{N} \frac{{Z_{\text{bead}}}^2 e^2}{4\pi\varepsilon\varepsilon_0\left|\mathbf{r}_i-\mathbf{r}_j\right|}\,\mathrm{e}^{-\left|\mathbf{r}_i-\mathbf{r}_j\right|/b} \tag{9}$$

Note that for the electrostatic interactions, the ligand length was taken into account in determining the interbead distance, depending on whether the beads were on the near, opposite, or same faces of the plates. Net van der Waals and electrostatic interactions were determined in this manner for a series of interparticle distances. The two potentials were then fit in Origin to curves of standard form for interparticle interactions:

$$E_{\text{vdW}}(d) = \frac{-A_1}{d^{B_1}} \tag{10}$$

and

$$E_{\text{el}}(d) = A_2 e^{-d/B_2} \tag{11}$$

with fitting parameters A_1, A_2, B_1 and B_2. The sum of these two curves, E_{tot}, was used to determine the position of the secondary energy minima, using Mathematica. We also evaluated the bead size effect by calculating the van der Waals interaction using a smaller bead size (8.75 nm in diameter) and the results are consistent with different bead sizes (**Figure 3.5B**). To assess the validity of the CG approximation, we first compared the analytical and CG models assuming no rotation between the plate pair. A comparison of interaction curves based on the two calculations at various ionic strengths is given in **Figure 3.5C**. **Figure 3.5D** demonstrates that the relevant features—secondary energy minima and their positions—are predicted with reasonable agreement. We therefore proceeded to use the CG model to determine the interaction of plates with various degrees of rotation and/or truncation.

Estimation of the Fluctuation Height of Anisometric Plates. The fluctuation height h, the height a colloid in a solvent can thermally fluctuate up to against gravity, is defined following a literature convention: $(\rho_{\text{Ag}} - \rho_{\text{water}})Vgh = k_{\text{B}}T$,[136] where ρ_{Ag} and ρ_{water} are the densities of silver (10.49 g cm^{-3}) and water (1.0 g cm^{-3}) respectively, V is the volume of a silver plate, g is the standard gravity, 9.8 m s^{-2}, k_{B} is Boltzmann constant (1.38 × 10^{-23} J K^{-1}) and T is the temperature (298 K). Take the truncated plates (**Figure 3.1**) as an example. They have an average basal plane area (S) of 3.27 μm^2 and an average thickness (t_{plate}) of 35 nm, leading to a volume V of 1.14 × 10^{-1} μm^3. For this system, we have h =388 nm, which is as much as 11 times the plate thickness. In **Figure 3.3A**, we calculated the relative probabilities of plate at different heights (H) based on the Boltzmann distribution ($p_{\text{rel}}(H) \approx e^{-((\rho_{\text{Ag}}-\rho_{\text{water}})VgH)/k_{\text{B}}T}$), which shows the plates can go up to micrometers away from the substrate. In **Figure 3.3B** which shows the fluctuation height as a function of plate thickness, we varied the plate thickness t_{plate} (in units of nm), while keeping the basal plane area constant (3.27 μm^2). The fluctuation height decreases with increasing plate thickness, suggesting the importance of nanoscale thickness to allow free motions of particles in the vertical direction.

The Deprotonation Percentage of Carboxylate–Thiols. The percentage of deprotonated carboxylate–thiols on the plate surface determines the plate surface charge density. We followed the Henderson–Hasselbalch equation: $\mathrm{pH} = \mathrm{p}K_\mathrm{a} + \log(\frac{[\mathrm{A}^-]}{[\mathrm{HA}]})$, where $[\mathrm{A}^-]$ and [HA] are the molar concentrations of $–\mathrm{COO}^-$ and –COOH groups. The $\mathrm{p}K_\mathrm{a}$ of the carboxylate–thiols is between 3.5 and 3.7 (according to the manufacturer), and we used 3.5 in our calculation. Based on the equation, over 99% of carboxylate–thiols are deprotonated at a pH higher than 5.5. Under the experimental condition, the amount of CO_2 dissolved in water under atmosphere pressure can be calculated to evaluate its effects on pH and ionic strength of the solution. Based on Henry's Law,[157] the amount of CO_2 dissolved in water is $[CO_2(aq)] = H^{cp}_{\mathrm{CO_2}} P_{\mathrm{CO_2}}$. Here $H^{cp}_{\mathrm{CO_2}}$ is Henry solubility constant for CO_2 in water and $P_{\mathrm{CO_2}}$ is the equilibrium partial pressure of CO_2 in air. Plugging in $H^{cp}_{\mathrm{CO_2}} = 3.4 \times 10^{-2}$ mol L^{-1} atm^{-1}, and $P_{\mathrm{CO_2}} = 0.000355$ atm, we get the concentration of dissolved CO_2, $c_0 = 1.2 \times 10^{-5}$ mol L^{-1}. The dissolved CO_2 will then react with H_2O: $CO_2(aq) + H_2O \rightleftharpoons H^+ + HCO_3^-$. The (apparent) first dissociation constant follows $K_{\mathrm{a1}} = \frac{[\mathrm{H^+}][\mathrm{HCO_3}^-]}{[\mathrm{CO_2}(aq)]} = 4.45 \times 10^{-7}$ mol L^{-1} and the second dissociation constant follows $K_{\mathrm{a2}} = 4.69 \times 10^{-11}$ mol L^{-1}. Since $\sqrt{c_0 K_{\mathrm{a1}}} > 40 K_{\mathrm{a2}}$ and $c_0 K_{\mathrm{a1}} > 20\, K_\mathrm{w}$ (K_w is the dissociation constant for water), we can ignore the amount of H^+ from water dissociation and the second dissociation reaction. As a result, we get $[H^+] \approx [HCO_3^-] = \sqrt{(c_0 - [\mathrm{H^+}])K_{\mathrm{a1}}} = 2.1 \times 10^{-6}$ mol L^{-1}. The solution pH after considering CO_2 dissolving in water is 5.7, which still keeps 99% of the charged ligands fully deprotonated. We expect this pH value would not change the deprotonation of ligands, namely the surface charge density of the plates, and have negligible increase (0.002 mM, 0.4% increase) on the ionic strength of the solution at 0.5 mM NaCl condition.

Columns Standing Versus Lying on the Substrate. We observed experimentally that the columns composed of plates of a relatively large basal plane area (3.27 µm^2), such as those used in **Figure 3.1**, tend to favor a "standing" configuration (where the plate basal planes sit parallel to the substrate) and have a lower tendency to orient their basal plane perpendicular to the substrate. "Lying" columns were observed in a small proportion (< 10%). This "standing" configuration is likely due to a combined effect of gravitational force and the van der Waals attraction between plate and glass substrate, which we calculated as below. A silver plate standing perpendicular to the substrate has a larger center-of-mass height than that lying parallel to the substrate (Δh ~868 nm). As a result, the standing plate experiences a higher gravitational potential of 2.5 $k_\mathrm{B}T$. This estimation suggests that the plates are favored to sit parallel to the substrate due to gravity. Regarding van der Waals attraction, the equation between two parallel slabs of different materials[158] is

$$E_\mathrm{vdW}(d') = -\frac{H_{1w2}S}{12\pi}\left[\frac{1}{(d')^2} - \frac{1}{\left(d'+t_\mathrm{plate}\right)^2} - \frac{1}{\left(d'+t_\mathrm{glass}\right)^2} + \frac{1}{\left(d'+t_\mathrm{plate}+t_\mathrm{glass}\right)^2}\right]$$

Here t_glass is the thickness of glass substrate (0.13–0.17 mm), much larger than the thickness of a plate t_plate (35 nm), so the equation can be simplified to

$$E_\mathrm{vdW}(d') = -\frac{H_{1w2}S}{12\pi}\left[\frac{1}{(d')^2} - \frac{1}{\left(d'+t_\mathrm{plate}\right)^2}\right]$$

In both equations, d' is the face-to-face separation between the substrate and the plate, S is the plate basal plane area, and H_{1w2} is the Hamaker constant for Ag and silica interacting across water (1.9×10^{-20} J).[159] Based on the calculation, the plate–substrate van der Waals attraction can be about –18 $k_\mathrm{B}T$ at a separation of ~100 nm and a few $k_\mathrm{B}T$ at ~250 nm separation, to support the columns "standing" on the substrate. On the other hand, when columns are composed of plates with small basal planes (for example, 0.90 μm^2), the lying configuration is preferred at relatively low ionic strengths.[51] Standing configurations are only favored when the ionic strength is high enough to screen the electrostatic repulsion between the columns and the substrate.

Processing of Optical Microscopy Images. The optical microscopy images in **Figures 3.1E and 3.17D** were processed as follows[137] to improve the image quality. The raw optical microscopy images were first extracted using ImageJ. Next a small number of sequential frames in the movie were averaged using MATLAB (5 images for **Figure 3.1E** and 5 images for **Figure 3.17D**). The number of sequential frames used for averaging was chosen such that the contrast was improved without loss of spatial resolution due to motion-blurring. The averaged image was further processed to subtract the image background using the built-in function of "Subtract Background" in ImageJ, followed by brightness and contrast adjustment. The rolling ball radius for the background subtraction was set as 1000 pixels. The original, averaged and background subtracted images are shown in **Figure 3.4**.

Characterization of the Three-Dimensional (3D) Nature of the Assembled Lattice. We have the following experimental data to demonstrate the 3D nature of the assembled lattices. First, the formation of the columns is supported by (i) direct imaging of face-to-face stacking of individual plates into columns as shown in **Figure 3.3C**, and (ii) direct imaging of a rotating column exhibiting different orientations as shown in **Figure 3.1C**. Rotating columns exhibit light, rectangular projections while lying on their sides, and dark, polygonal projections while standing vertically on the substrate. The fact that the columns serve as the building blocks of the lattice suggests that the lattice is 3D. Second, the polygonal projections of the standing columns shown in **Figure 3.1C** match with the building blocks in the final hexagonal lattice (**Figure 3.1E**), and we observed the gradual increase of the concentration of standing columns leading to the 3D structure (**Figure 3.1F**). The empty space between each standing column in the 3D structure at intermediate column concentration makes it clear to see the plates stacked upon each other into columns with fast rotations (**Figure 3.7C**). A similar aspect is shown in **Figure 3.12** detailing different plate layers in columns comprising the 3D hexagonal lattice presented in **Figure 3.10C**. Lastly, the polygonal projections of the lattice building blocks dynamically change their shapes, which is not possible if the lattice is formed from 2D layer of individual triangular plates. Plates of the first few layers in the column are identified based on their contrast under optical microscopy. We controllably dried the observed lattice after its formation at 3 mM ionic strength in the optical microscopy chamber, to maximally maintain the structure for scanning electron microscopy (SEM) imaging as we monitored under the optical microscopy (although the plate-to-plate spacing in the same column disappears). In **Figure 3.9**, the SEM images clearly show that the plates are stacked face-to-face into columns, which further assemble laterally into 3D structures.

Analysis of the Local Curvature of Column Projection Contours. Curvature analysis (**Figures 3.10A–B and 3.17B**) was performed using built-in functions in ImageJ to identify the contours of the column projection, followed by local curvature calculation using MATLAB. Specifically, we used the “Make Binary” function in ImageJ to binarize the optical microscopy image, the “Outline” function in ImageJ to recognize the contour, and the “Wand” function in ImageJ to extract the XY coordinates of this contour, which serve as the input for the curvature calculation in MATLAB.[137] The detailed processes are shown in **Figure 3.11A**. Sometimes the image threshold was slightly adjusted in order to differentiate a column from nearby single plates, followed by the “Dilate” function to obtain accurate contours. The curvature values $(1/R)$ were calculated by fitting a local arc of the contour with circles, where R is the radius of the fitted circle. The fitting was conducted by first smoothing the contour by averaging every successive 5 points, and then finding the circle radius for each point using the nearest 25 points (**Figure 3.10A–B**) or 15 points (**Figure 3.17B**) in the contours depending on the image magnification.

Analysis of the Hexagonal Lattice. The analysis workflow of the hexagonal lattice (**Figure 3.10**) is shown in **Figure 3.13**. First the positions of individual columns in each frame were tracked, as the central positions of the fitted circumscribed circles of the column projections. Based on the tracked central positions, we were able to derive a series of parameters. First, we computed the velocities of each column over time increments of 0.7 s (12 frames) as shown in **Figure 3.10D**. Second, we performed a Voronoi cell analysis and calculated the local density ρ_j, which is the inverse of the area of the Voronoi cell enclosing column j. Third, the radial distribution function[117] $g(r)$ was calculated based on the column positions over 32 frames in the movie of the hexagonal lattice (**Figure 3.10E**). We followed the standard method[160] to perform periodic boundary correction of the computed $g(r)$ to account for the limited viewing area. From the $g(r)$ *vs.* r curve, r_c (3.13 μm) located at the first minimum after the first peak of $g(r)$ was obtained to determine the threshold for the nearest-neighbor bond length (**Figure 3.13B**). In particular, only columns with a center-to-center distance $r < r_\mathrm{c}$ are recognized as connected *via* a nearest neighbor bond. A bond network was mapped for each frame in the movie to determine the number of the nearest neighbors (**Figure 3.13C**). We then computed a six-fold local bond orientation order parameter[142] for each column j following $|\psi_{6j}| = |\frac{1}{Z_j}\sum_{k=1}^{Z_j}\exp(6i\beta_{jk})|$, where Z_j is the number of nearest neighbors of column j, the summation goes over all nearest neighbors, and β_{jk} is the angle between the bond linking column j and its kth neighbor and an arbitrary reference axis. This analysis was performed on each frame in the movie (in total 32 frames). Given the local density ρ_j and structural order parameter $|\psi_{6j}|$, we were able to plot out a two-dimensional (2D) histogram of columns on $(|\psi_{6j}|, \rho_j)$ as shown in **Figure 3.10F**.

Analysis of the Honeycomb Lattice Structures. In a honeycomb lattice domain, we measured the orientations of three long sides of the visible (likely on the first layer) plates in each column. The 2D orientation map of the three long sides of first-layer plates is shown in **Figure 3.17D**, which shows a six-fold symmetry, further confirming the honeycomb lattice structure.

Notes to Chapter 3

This chapter is adapted with permission from the paper "Luo, B. et al. Hierarchical self-assembly of 3D lattices from polydisperse anisometric colloids. *Nat. Commun.* **10**, 1815 (2019)",[50] Copyright © 2019, Springer Nature.

CHAPTER 4: UNIVERSAL LAYER-BY-LAYER GROWTH MODE IN NANOPARTICLE SUPERLATTICES

Introduction

Growth of crystals occurs through attachment of new building units, such as atoms, ions, molecules, and nanoparticles, to surfaces from a suspended medium.[56-58, 60, 161-166] This kinetic process dictates major design parameters (e.g., crystal symmetry, morphology, and surface structure) as well as their applications ranging from semiconductors to strain-relief nanostructured arrays.[161, 164, 165, 167] For example, the extent of supersaturation has been shown to determine the polymorphs of lysosome crystals,[168, 169] while the ion flux during the growth of semiconductor devices shapes the distribution of grain boundaries and defects, which interfere with transport of charge carriers.[164] Phenomenologically, one robust observation is an intriguing yet puzzling dependence of crystal growth modes on the size of the building units.[164, 167, 170] On the atomic scale, crystals growth theories have been established decades ago and successfully applied to explain and guide experimental crystal growth.[57, 161, 162, 166] In particular, layer-by-layer growth has been regarded as a hallmark of atomic crystallization to produce flat films of semiconductors or alloys.[60, 161, 171] In contrast, crystalline photonic coating consisting micron-sized colloids often adopt corrugated surfaces, which can be seen as an anthill covered by ants crawling on each other, with surface roughness matching with predictions of capillary waves.[123, 172, 173] The lack of scalability of crystal growth mode with the size of building units becomes even harder to understand due to the existence of knowledge gap on the crystal growth behaviors at the intermediate nanoscale.

Until now, crystal growth modes of nanoscopic building units have remained largely unexplored in both experiments[5, 174] and simulations,[11] though the same set of design parameters govern critically the applications of their crystalline form, such as metamaterials and photocatalysis in the case of nanoparticle superlattices.[4] Experimental challenges come from the difficulty of directly imaging real-time, real-space dynamics in solution at the needed spatial resolution,[5, 30, 49, 175] where routine electron microscopy requires dry and thus static samples,[4, 176, 177] while ensemble scattering (e.g., small-angle neutron or X-ray scattering) methods do not resolve structure or dynamics at the single-particle level.[13, 30] For simulation and modeling, crystal growth kinetics poses challenges unique to the nanoscale.[11] The importance of discreteness and fluctuation resulting from the comparable sizes of nano-sized building units with solvent and ligand molecules makes the modeling of elementary force field highly non-trivial. As a result, it has been hard to reconcile the fine details of force field with the requested much larger time and length scales concerning mass transport and the large number of post-nucleation building units present in growth studies. More importantly, the fundamental lack of experimental data on key parameters (e.g., energy barriers, diffusion rates, flux rate) essentially excludes the use of trustable inputs or validation for simulations. This situation differs from atomic crystallization, where materials-specific parameterization has been established experimentally.

Here we report the first imaging of crystal growth modes at the nanoscale and present a unified framework that applies to nanoscopic building units, where key parameters are measured that are otherwise inaccessible, such as diffusion rate, and its associated energetic barriers.[167] The experimental imaging has been made possible via low-dose liquid-phase transmission electron microscopy (TEM)[5, 174] combining compatibility with a suspension and nanometer resolution. We focus on the model systems of nanoparticles crystallizing into three-dimensional (3D) superlattices, where tracking of individual nanoparticles reveals the complete superlattice growth process such as nanoparticle adsorption/desorption, surface diffusion, propagation and merging of the steps, and individual nanoparticle displacements in the crystalline structures. We elucidate unexpectedly a prevalent layer-by-layer growth mode reminiscent of atomic crystallization[56-58, 60] in a diversity of nanoparticle shapes, where a new surface layer grows only after the preceding layer is completed. Coupling statistical analysis of experimental TEM movies with molecular dynamics (MD) simulations, we elucidate that building unit size governs the order of magnitudes of two important controlling factors in crystal growth: the surface diffusion rate D, and the interaction range (Δ). These two parameters further shape the thermodynamic and kinetic driving forces for growth behaviors. Notably, our framework explains the prevalent observation of corrugated crystal surface composed of micron-sized colloids,[2, 123, 172] whose relatively shorter-ranged interaction reduces the thermodynamic preference to the smooth surface, and the slower diffusion rate leads to more trapping at local energy-minima surface sites.[167, 178] Our work fills the long-standing knowledge key gap of crystal growth habits at the nanoscale. The universally achieved layer-by-layer growth can serve as the synthetic basis of faceted superlattices and the principle underneath can enable crystal morphology engineering (e.g., Wulff, Winterbottom and Summertop construction rules, new shapes from seeded growth resembling snowflake morphologies) on the edge and corner surface sites for applications such as nonlinear optics and photocatalysis.[166]

Results and Discussion

Liquid-phase TEM (**Figure 4.1**) captures directly the layer-by-layer growth of a simple cubic superlattice from a suspension of concave gold nanocubes. The concave nanocubes have an edge length $L = 62.0 \pm 4.6$ nm and a concaving angle[179] α of 16° (**Figures 4.1A and 4.2**). They are coated with negatively charged thiols, causing them to remain dispersed in deionized water due to electrostatic repulsion (E_{el}). For liquid-phase TEM imaging, an aqueous suspension of highly concentrated concave nanocubes is sealed between two SiN_x chips following our previously reported protocols.[30, 137, 174] Low electron beam dose rates (4–27 $e^{-}Å^{-2}s^{-1}$) are used in all the experiments, which keep thiol ligands and nanoparticles intact under electron beam illumination and do not fundamentally alter the interparticle interactions.[30, 137, 174] Upon an increase in the phosphate buffer concentration (PBS, pH = 8; range of ionic strength I: 15–110 mM) in the sample, the elementary interparticle interaction (E_{tot}) becomes attractive, as the van der Waals attraction E_{vdW} balances the screened E_{el} and the (entropic) steric repulsion[91] of the ligands E_{steric} (**Figure 4.1A**), thereby triggering nucleation and growth of superlattices in-situ. The nucleation of the square lattice occurs via the face-to-face attachment of concave nanocubes (**Figure 4.3**). In this work we focus on the growth stage, the further expansion of single crystallinity subsequent to nucleation, which produces large-scale 3D simple cubic superlattices (**Figure 4.3A**). The radial distribution function and bond network of the superlattice (**Figure 4.3, B to C**) show high ordering spanning a lateral dimension larger than 2 µm, comprising more than 1000 concave nanocubes in the superlattice. Due to thermal fluctuations, the concave nanocubes exhibit local vibrations and self-correction of mis-coordinated sites as they relax at the lattice sites (**Figure 4.3D**).

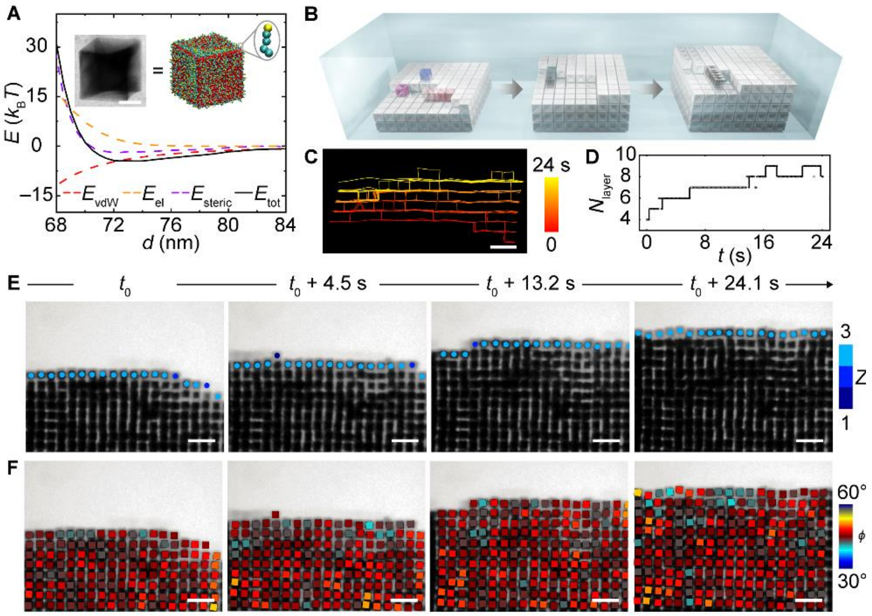

Figure 4.1. Layer-by-layer growth of nanoparticle superlattices from gold concave nanocubes. (A) Contributions to the interaction energy of two concave nanocubes approaching face-to-face at I = 25 mM as a function of center-to-center distance d, as computed from molecular dynamics simulation (right inset schematic). Left inset: TEM image of a concave nanocube. Note that the pairwise binding energy (with magnitude $\varepsilon = 4.5\ k_\mathrm{B}T$) is estimated as the minimum of E_tot versus d. (B) Schematic of terrace (blue), step (purple), and kink (red) sites on the surface of a simple cubic lattice from concave nanocube assembly, following layer-by-layer growth pathways. (C) Interface profile of the superlattice in (E). (D) Staged growth of the number of layers N_layer over time t in (E). (E) Time-lapse liquid-phase TEM images showing the layer-by-layer growth of simple cubic superlattice from concave nanocubes at I = 25 mM. Particles in the advancing surface layer are labeled with dots color-coded by their coordination numbers. Dose rate 27.1 $\mathrm{e}^{-}\text{Å}^{-2}\mathrm{s}^{-1}$. (F) Voronoi cell partition and orientation maps of the concave nanocubes in (E). Each Voronoi cell is colored according to the orientation ϕ_j of each concave nanocubes. Scale bars: 30 nm in (A), 200 nm in (C), (E), and (F).

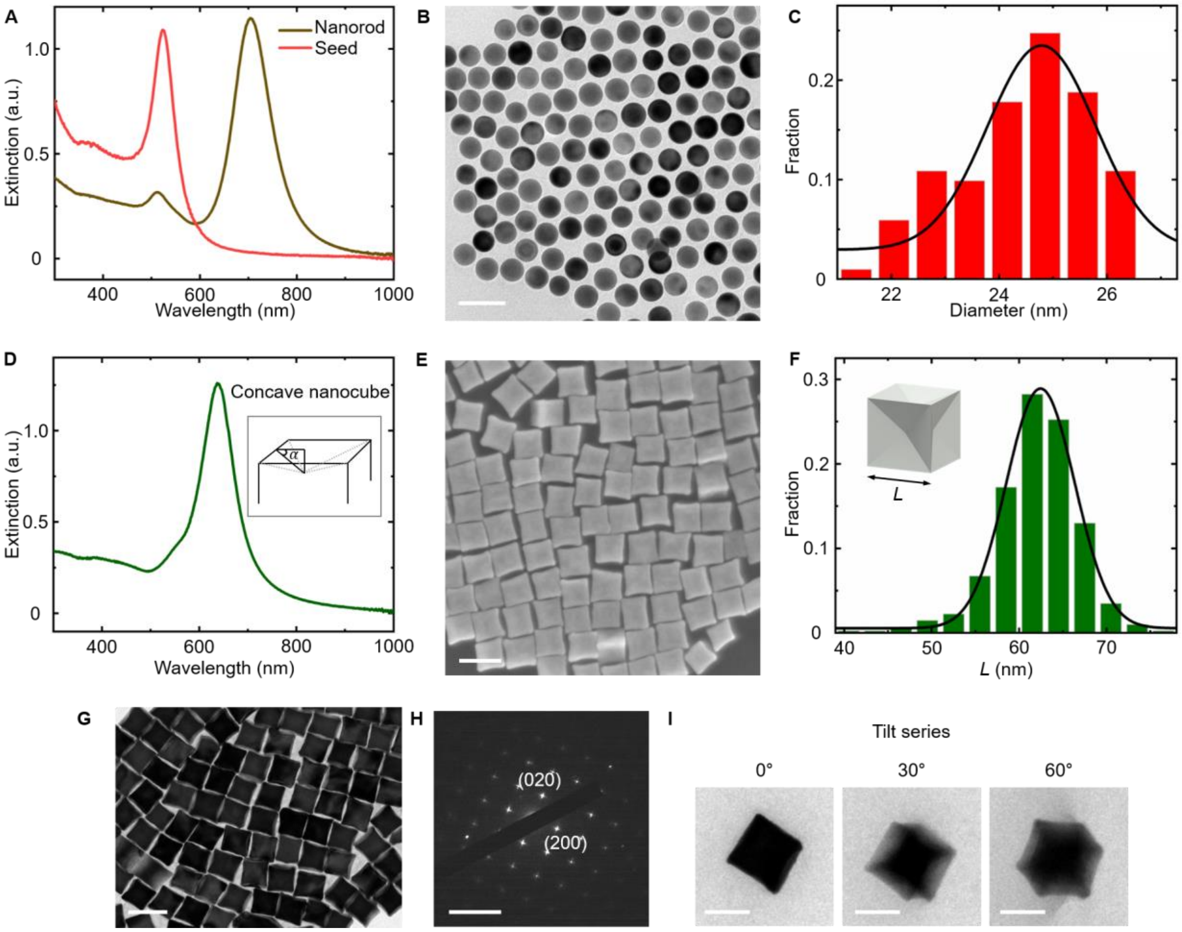

Figure 4.2. Characterization of the gold nanorods, monodisperse gold spherical seeds and gold concave nanocubes. (A) UV-Vis spectra of the as-synthesized gold nanorods and the monodisperse gold spherical seeds. (B) TEM image of the as-synthesized monodisperse gold spherical seeds. (C) Size histogram of the gold spherical seeds. (D) UV-Vis spectrum of the gold concave nanocubes, inset schematic denoting the concaveness α, defined as the angle between the facets and the (100) facets of an ideal cube. (E) SEM image of the gold concave nanocubes. (F) Histogram of the edge length (L, inset schematic) of the concave nanocubes. (G) TEM image of the gold concave nanocubes. (H) Nanobeam diffraction pattern of a single gold concave nanocube, showing that the surfaces of the concave nanocube correspond to the {100} facets of the face centered cubic structure of gold. (I) Tilt series of TEM images of the gold concave nanocubes. Scale bars: 50 nm in (B) and (I), 100 nm in (E) and (G), 10 nm^{-1} in (H).

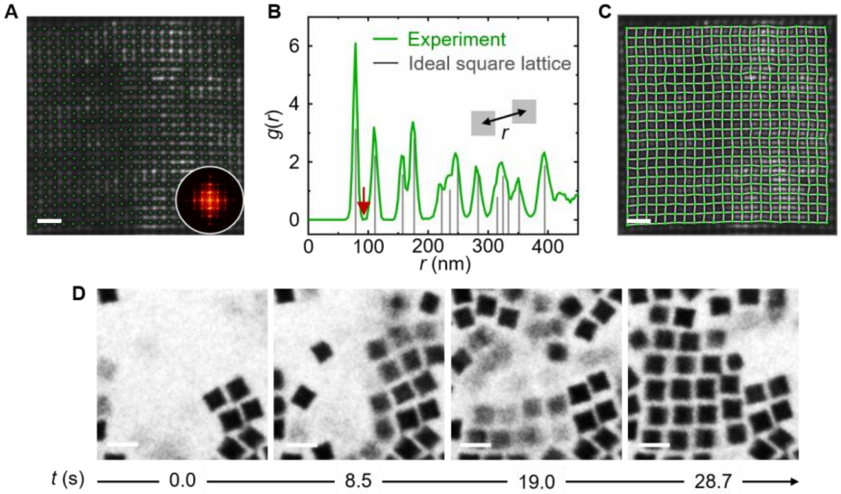

Figure 4.3. Analysis of the structuring order in the superlattices of gold concave nanocubes. (A) Liquid-phase TEM image showing a large-scale superlattice from gold concave nanocubes. The tracked positions of each concave nanocube were overlaid as green dots. Inset: Fourier transfer of the image. (B) Radial distribution functions of the assembled superlattice (green line) and an ideal square lattice (grey lines), from which a r_c (91.1 nm, red arrow) determined at the first minimum of $g(r)$ was used as the threshold for the nearest-neighbor bond. (C) Bond network of the superlattice. (D) Time-lapse liquid-phase TEM images showing the concave nanocube assembly into a square superlattice. Ionic strength: 15 mM. Scale bars: 200 nm in (A) and (C), 100 nm in (D).

During the growth process, incoming concave nanocubes preferentially fall into the kink sites on a growing crystalline layer to form a flat surface; sufficient diffusion prevails over the formation of corrugated terraces (**Figure 4.1, B to F**, I = 25 mM). This growth behavior is clearly captured in the surface profiles of the superlattice overlaid over time (**Figure 4.1C**) and time-lapse liquid-phase TEM images (**Figure 4.1E**). Further tracking of the superlattice surface shows a staged increase in the number of lateral layers (**Figure 4.1D**), a key signature of layer-by-layer growth mode. The orientation map[123] of the nanoparticles in the superlattice shows a high orientational order, highlighting the face-to-face alignment of neighboring concave nanocubes (**Figure 4.1F**). Notably, the binding energy from this face-to-face alignment serves as the thermodynamic driving force for an incoming building unit to position in the most-coordinated kink site,[58, 60] not a terrace or step site (**Figure 4.1B**). This binding energy is quantified by our MD simulation where we adopt a detailed coarse-grained model (with $\sim 4.6\times10^{6}$ gold atoms as the gold core and $\sim 1.6\times10^{3}$ grafted ligand chains) to take into account both the geometric details of concave nanocubes and the ligand entropic effects (**Figure 4.4**). As shown in **Figure 4.1A**, the binding energy (< 0, with magnitude ε) per face-to-face contact (i.e., one coordination), estimated as the minimum of E_{tot} along center-to-center distance d, at $I = 25$ mM is $-4.5\ k_{\mathrm{B}}T$. This binding strength is sufficient to favor positioning in the kink sites and thus leads to smooth crystal surfaces at thermodynamic equilibrium condition.

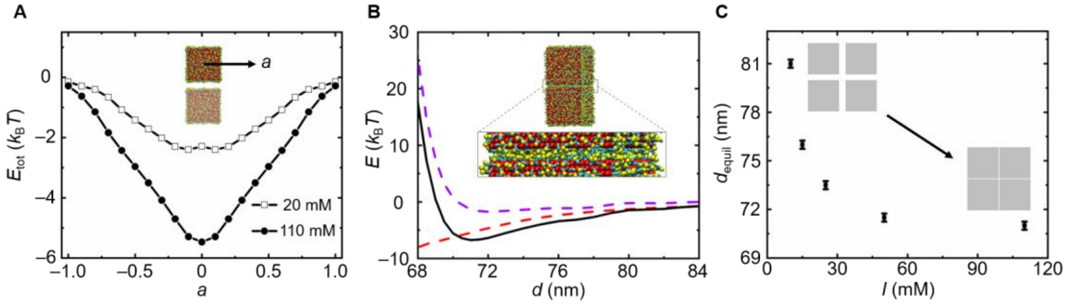

Figure 4.4. Coarse-grained simulation model of the pairwise interaction energy of gold concave nanocubes. (A) Total pairwise interaction energy E_{tot} between two concave nanocubes as a function of the relative horizontal offset a (see the inset schematic) at the respective lattice spacing d_{equil} at ionic strengths of 20 and 110 mM. The energy minimums locate around $a = 0$, indicating that the face-to-face configuration with no offsets is energetically preferred. (B) Energy components of two concave nanocubes approaching face-to-face at $I = 110$ mM versus interparticle center-to-center distance d, as computed from molecular dynamics simulation. Purple line: E_{steric}; Red line: $E_{\mathrm{vdW}} + E_{\mathrm{el}}$; Black line: E_{tot}. The inset snapshot from our simulation shows the overlap between ligands of two concave nanocubes as they approach, resulting in the steric repulsion. (C) Predicted lattice spacing (d_{equil}) as a function of ionic strength (I) computed from simulations, showing that d_{equil} decreases with increased ionic strengths (see the inset schematics).

Next, detailed analysis of the kinetic driving force for the layer-by-layer growth elucidates how the growth laws depend on the building unit size. During crystal growth, incoming flux can directly deposit to the kink sites, or fall into step or terrace sites which are local energy minima with partially coordinated neighbors.[60, 161, 171] In the latter scenario, successful arrival at the kink sites requires hopping over the in-plane or step–edge energy barriers (ΔE^{in} and ΔE^{SE}, respectively, **Figure 4.5A–B**) via thermally agitated diffusions. As a result, one established parameter governing this effect is D/F with D being the surface diffusion rate and F being the flux, which measures the extent of surface sites explored by the deposited building unit before it meets another particle, a partially grown layer or the edge of a step.[171] Qualitatively, a small D/F predicts kinetically roughened growth because the building unit diffuses too slowly to reach at the kink site before the deposition of another unit, while a large D/F leads to sufficient diffusion over flux and achieves a layer-by-layer growth. The surface diffusion rate D can be estimated as $D = D_0 \exp\left(-\Delta E^{\mathrm{in}}/k_{\mathrm{B}}T\right)$, where D_0 is the intrinsic diffusion rate of a building unit over a crystal surface with no diffusion barriers. However, it remains elusive to what extent growth laws are size scalable with different length scales. While D_0 has an inverse dependence on the building block size based on Stokes–Einstein relationship, it takes our generic analytical model to show that the building unit interaction range (relative to particle size) Δ shapes the energy landscape of the crystal surface as well as the depth of ΔE^{in} (**Figure 4.5B**). As shown in **Figure 4.5B**, the energy landscape of a crystal surface varies from highly wavy shape with a large ΔE^{in} (green, Δ=0.01; e.g., micron-size colloids), slightly wavy shape with a small ΔE^{in} (light blue, Δ=0.12), to smooth shape with an ignorable ΔE^{in} (dark blue, Δ=0.41). This trend can be explained by the physical picture that binding interactions beyond nearest neighbors become increasingly important as Δ increases.[170] Particularly, nanoparticles cover a wide spectrum of interaction ranges (e.g., Δ

from < 0.12 for concave shapes to 0.41 for planar shapes) by varying their shape and surface chemistry.[11] Combining the size dependence of D_0 and ΔE^{in}, we recognize that atoms and nanoparticles possess a sufficiently large diffusion rate D and thus a large D/F by assuming a stable practical range of F across different length scales, and thereby easily fall into layer-by-layer growth mode. Indeed, by experimentally tracking surface diffusing nanoparticles in our system, we measure that the diffusion rate D is 132.0 d_{equil}^2/s (d_{equil}: the equilibrium lattice spacing; **Figures 4.5C and 4.6**), which turns out to be about 4 orders of magnitude larger than a typical surface diffusion rate of micron-sized colloids reported in earlier experiments (~0.01 d_{equil}^2/s).[167, 178] The slower diffusion of micron-sized colloids make it harder for them to achieve the layer-by-layer growth and easier to fall into kinetically roughened growth, consistent with the missing of reports of layer-by-layer growth mode or faceted crystals formed at the microscale.[2, 123, 172]

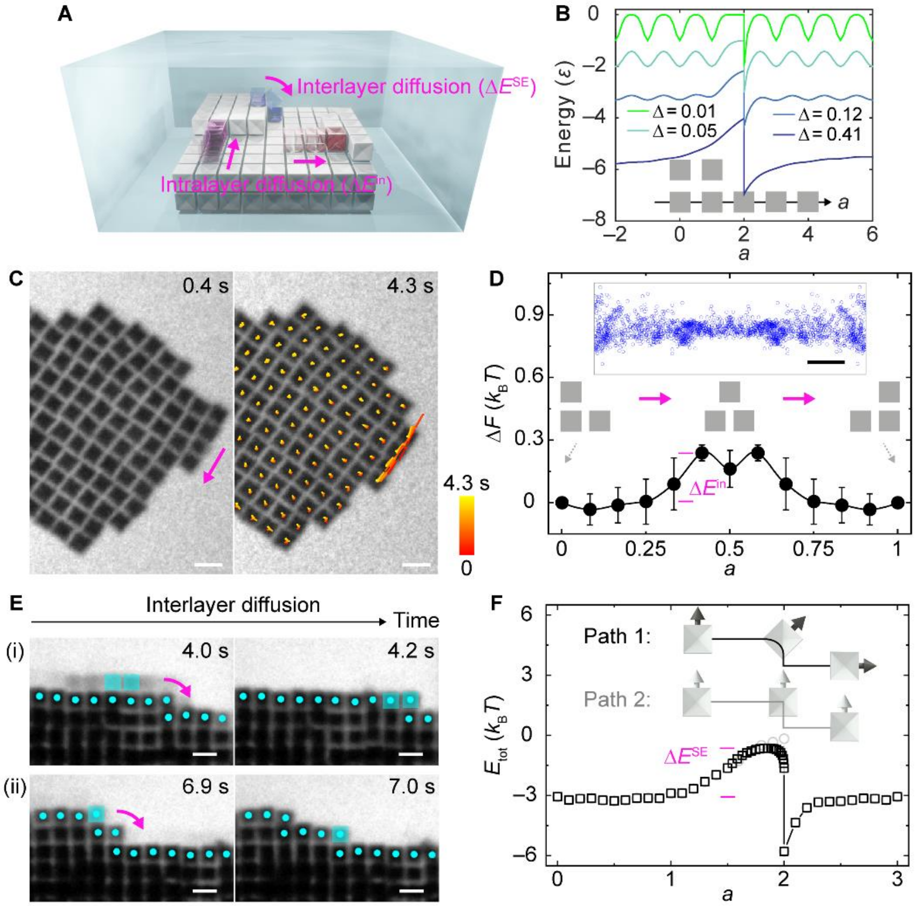

Figure 4.5. Surface diffusions and the corresponding energy landscape. (A) Schematic showing the intralayer and interlayer diffusion processes. (B) Energy landscapes experienced by a particle moving across a step edge for different interaction ranges Δ. For easy comparison, the curves with Δ=0.05 and Δ=0.12 are displaced vertically by $-\varepsilon$ and -2ε, respectively. (C) Time-lapse liquid-phase TEM images showing intralayer diffusion. The right TEM image is overlaid with trajectories. Dose rate 17.9 $e^{-}Å^{-2}s^{-1}$. (D) Relative free energy ΔF (reference state chosen at a = 0 and 1) at the superlattice surface measured from experiments. The error bars are from averaging measurements of three independent movies. Inset: Scatter plot of surface particle positions relative to the center of a nanocube pair underneath. (E) Time-lapse liquid-phase TEM images of two representative interlayer diffusion events. The particles labeled as cyan squares are undergoing interlayer diffusion across the underlying layer. (F) Energy landscape experienced by a concave nanocube diffusing between layers along two possible paths as depicted. Energies are computed from simulations at I = 25 mM. Scale bars: 100 nm in (C) and (E), 30 nm in (D).

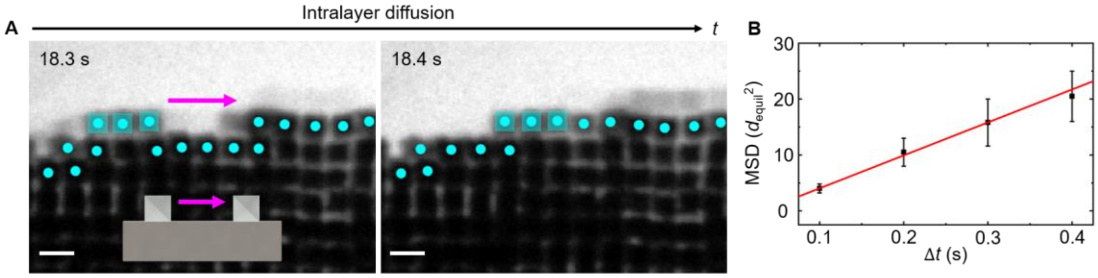

Figure 4.6. Intralayer diffusion in the layer-by-layer growth of gold concave nanocubes. (A) Time-lapse liquid-phase TEM images showing a typical intralayer diffusion from ledge to kink sites in the layer-by-layer growth (pink arrow). Scale bars: 100 nm. (B) MSD versus *t* plot. The error bars represent standard errors from particle diffusion statistics. Ionic strength: 25 mM.

While our analytical model captures a generic effect of building-unit size on the shape of energy landscapes, we further map, for the first time, the practical energy landscape for our system from both particle diffusion trajectories in experiments and energy calculation in MD simulations. Such experimental quantifications are made only possible by the liquid-phase TEM. From the particle coordinates of surface particles relative to a concave nanocube pair underneath (**Figures 4.5C–D and 4.7**, I = 110 mM), we derive the energy landscape by assuming a Boltzmann distribution of the particle positions. As shown in **Figure 4.5D**, the global energy minimum is located around perfect face-to-face alignment, consistent with the overall simple cubic symmetry. The value of ΔE^{in}, measured as the barrier between local minima, is as small as ~0.2 k_BT, on the same order of magnitude with that obtained from MD simulations (~0.1 k_BT). The interlayer diffusion, where particle climb over a step edge from a terrace to a kink site, is considered as another key factor for the layer-by-layer growth.[180] This process is observed to happen efficiently in our system (typically within 0.1–0.2 s, either one or multiple nanoparticles diffusing together, **Figures 4.5E and 4.8**), which assists the layer-filling process in the vertical direction.

The associated step–edge barrier ΔE^{SE} is computed as ~2.4 $k_{\mathrm{B}}T$ at I = 25 mM by MD simulations (**Figure 4.5F**), which is considerably smaller than the value for atomic systems (from 0.2–0.5 eV, or equivalently 8–20 $k_{\mathrm{B}}T$).[180] These values match with our framework on the building unit size-dependent kinetic driving force for layer-by-layer growth (**Figures 4.5B**). In comparison, interlayer exchange is largely suppressed in micron-sized colloidal systems by the step–edge barrier of a diffusive origin,[167] which prevents particles from descending from the top of a surface layer to merge with the growing layer.

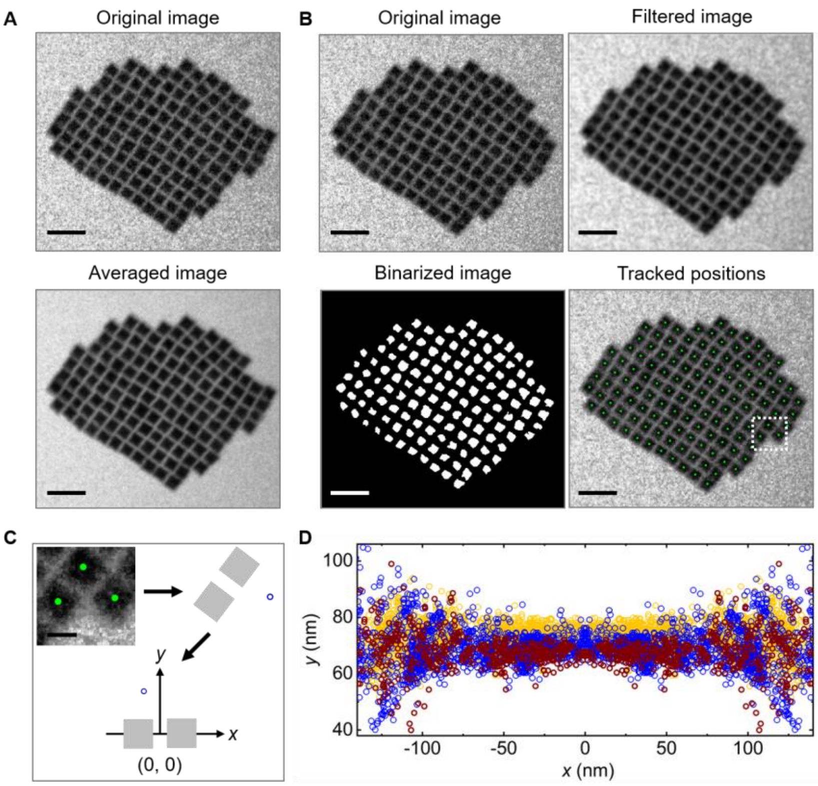

Figure 4.7. Image processing and single particle tracking. (A) The raw liquid-phase TEM image (top) and the image after average (bottom). (B) The tracking workflow to determine the positions of concave nanocubes in liquid-phase TEM movies. In the lower right image, the tracked positions were overlaid as green dots. (C) Flowchart of intralayer diffusion using an example of the boxed region in the bottom right image in (B). The surface particle was re-positioned into the relative position coordinate. (D) Scatter plot of surface particle positions relative to the center of the nanocube pair underneath. Each color represents one dataset of an independent liquid-phase TEM movie. Ionic strength: 80–110 mM. Scale bars: 200 nm in (A) and (B), 50 nm in (C).

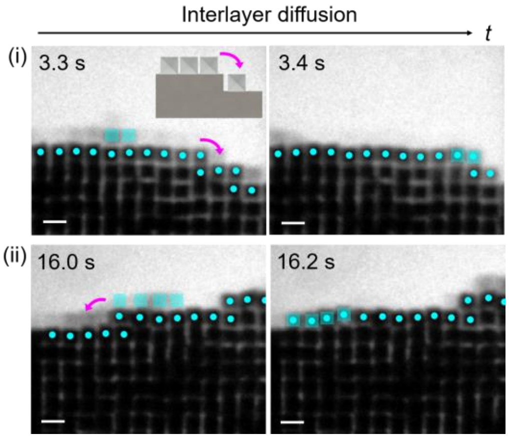

Figure 4.8. Time-lapse liquid-phase TEM images of interlayer diffusion events in the layer-by-layer growth of gold concave nanocubes. Pink arrows highlight the exchange directions. Ionic strength: 25 mM. Scale bars: 100 nm.

The above framework explains the robustness of layer-by-layer growth for our nanoscopic building units, following which we tune the binding energy to alter the surface structures, potentially impacting their coupled properties for applications.[4] Particularly, we trigger a thermodynamic roughening transition by lowering the inter-particle binding strength via varying the ionic strength, leading to a roughened superlattice growth with corner and edge sites (**Figure 4.9A**). As shown in **Figure 4.9B**, the magnitude of the binding energy per contact (ε) decreases as the ionic strength I decreases ($\varepsilon = 4.5\ k_B T$ for layer-by-layer growth at $I = 25$ mM; $\varepsilon = 2.8\ k_B T$ for $I = 15$ mM) predicted from our MD simulations. Experimentally, we observe at $I = 15$ mM, the superlattice surface, although maintaining the same simple cubic symmetry, becomes highly roughened (**Figure 4.9C**). The roughness of the crystal surface increases from ~ 0.9 d_{equil} (layer-by-layer growth) to ~3.6 d_{equil} here (**Figure 4.10**). This observation is reminiscent of the roughening transition occurring in atomic metal and alloy films[60] initiated upon elevation of temperature to weaken inter-atom interactions. Notably, the single-particle motions in the superlattices also exhibit distinct behaviors in different growth modes. The velocity field of concave nanocubes in this roughened growth mode exhibits extended domains with large translational motions (**Figures 4.9D–E, 4.11**), different from that in the layer-by-layer growth mode with sparse, small vibrations (**Figure 4.9F–G**). Both the orientational and magnitude correlation of the velocity field in the roughened growth (**Figure 4.9D**) decay much slower than that in the layer-by-layer growth (**Figure 4.9F**), indicating the collective/correlated motions of the lattice sites. This could be attributed to the weakened nanoparticle interactions in the roughened growth, which serves effectively as "elastic springs" restraining the deviation of particles from the lattice sites.

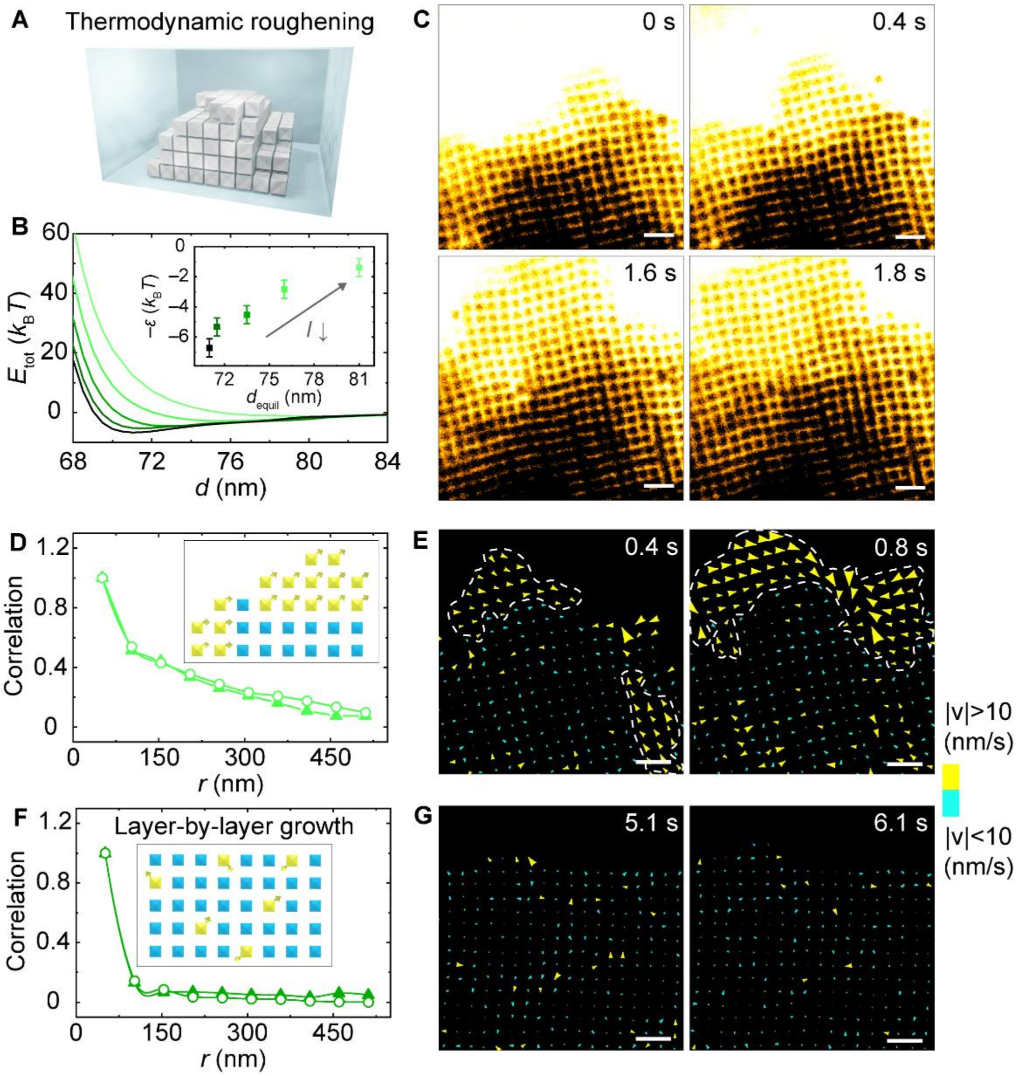

Figure 4.9. Thermodynamic roughening transition in the growth of the superlattice. (A) Schematic showing a thermodynamic roughened surface of a simple cubic lattice. (B) Total pairwise energy E_{tot} versus particle center-to-center distance d computed from simulations at different ionic strengths I (from dark to light green: 110 mM, 50 mM, 25 mM, 15 mM, and 10 mM). Inset: Pairwise binding energy $-\varepsilon$ versus the predicted lattice constant d_{equil}. (C) Time-lapse liquid-phase TEM images of a simple cubic superlattice growing with roughened surface, at I = 15 mM. Dose rate 14.9 $e^{-}Å^{-2}s^{-1}$. The TEM images are colored according to image intensities to highlight different layers in the lattice. Correlation in the magnitude (triangles) and orientation (circles) in the velocity field of lattices with roughened surface (D) and smooth surface (F). Velocity fields of lattices with roughened surface (E) and smooth surface (G). Scale bars: 200 nm.

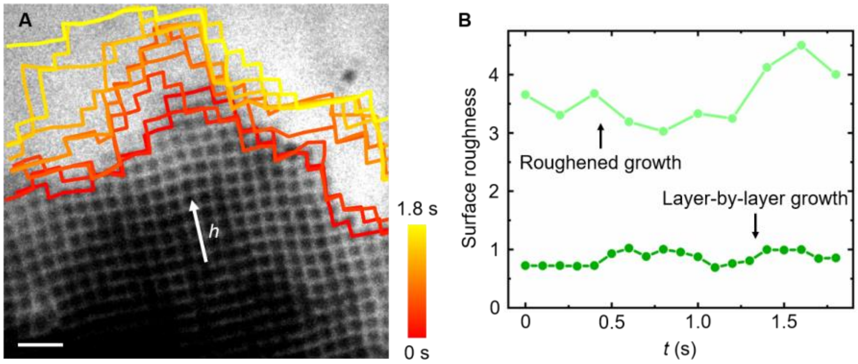

Figure 4.10. Surface roughness of the growing superlattices from gold concave nanocubes. (A) TEM image overlaid with tracked surface profile in the roughened growth. White arrow denotes the crystal growth direction. Ionic strength: 15 mM. Scale bar: 200 nm. (B) Surface roughness (defined as the standard deviation of the surface profile *h* in (A) normalized by d_{equil}) over time in the roughened growth (light green) and in the layer-by-layer growth (olive).

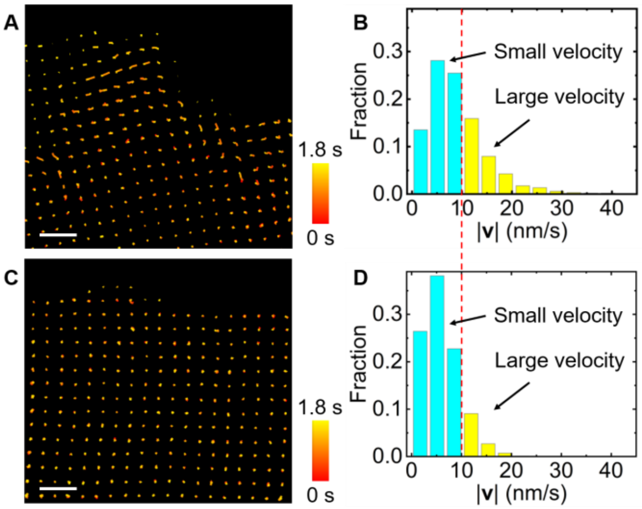

Figure 4.11. Velocity field of the growing superlattices from gold concave nanocubes. (A) Trajectories and velocity distribution (B) of the concave nanocubes in the roughened growth. (C) Trajectories and velocity distribution (D) of the concave nanocubes in the layer-by-layer growth. Scale bars: 200 nm.

Our bridging of the crystal growth laws across length scales (from atoms, nanoscale to micron-scale) fills the fundamental knowledge gap of the scalability. As a demonstration of the general applicability of our framework, we discover the layer-by-layer growth mode in nanoparticles of diverse symmetries and surface curvatures, from concave nanocubes we hitherto focus on, nanocubes (**Figure 4.12A–D**), to nanospheres (**Figure 4.12E–H**). This consistency provides a fundamental kinetic underpinning responsible for previous prevailing observation of faceted nanoparticle superlattices with smooth surfaces reported outside TEM.[4, 181-183] We foresee such understanding can enable engineering opportunities of crystal growth,[58, 60, 166, 184] such as modifiers to pin steps, to control supersaturation, to control stereochemical recognition, or even active modulators mimicking biological systems in shuttling reactants and products to desired locations by cellular machineries to impose influence on fluxes.

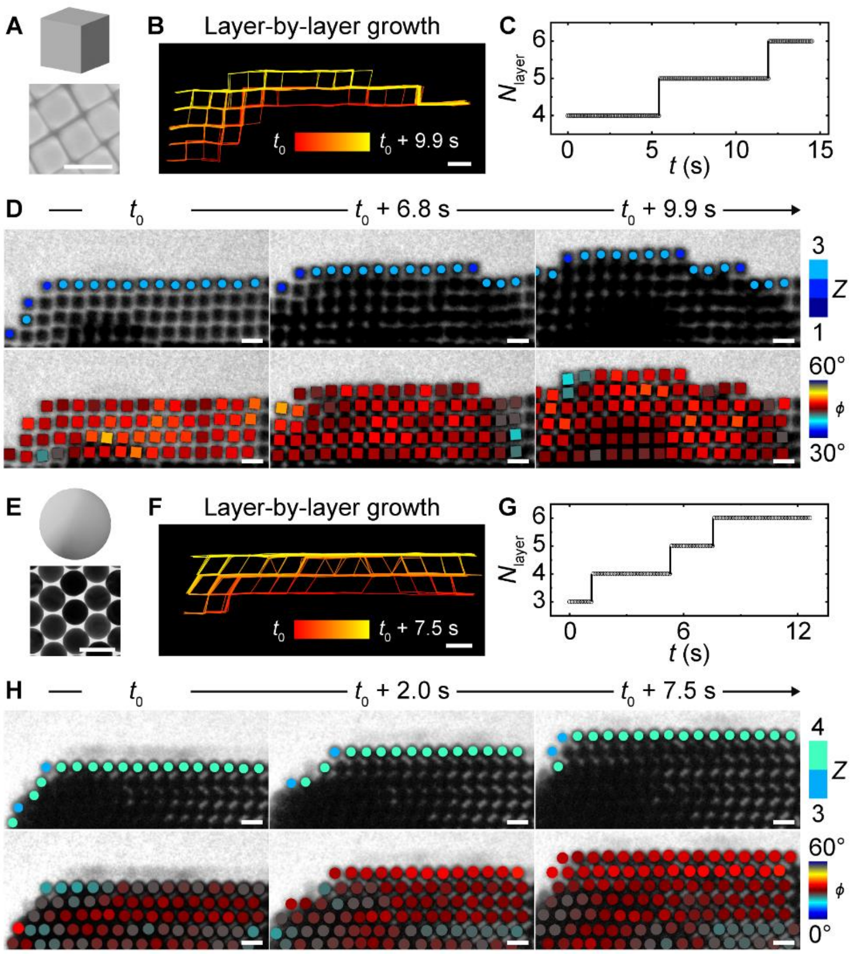

Figure 4.12. Generalization of layer-by-layer growth of nanoparticles with different shapes. (A) Schematic and SEM image of gold nanocubes with flat faces. (B) Interface profile of the superlattice in (D). (C) Staged growth of the number of layers N_{layer} over time t in (D). (D) Top: Time-lapse liquid-phase TEM images showing the layer-by-layer growth of superlattice from nanocubes. Particles in the advancing surface layer are labeled with dots color-coded by their coordination numbers. Dose rate 15.5 $e^{-}Å^{-2}s^{-1}$. Bottom: Voronoi cell partition and orientation maps of the nanocubes. Each Voronoi cell is colored according to the orientation ϕ_j of each nanocubes. (E) Schematic and TEM image of gold nanospheres. (F) Interface profile of the superlattice in (H). (G) Staged growth of the number of layers N_{layer} over time t in (H). (H) Top: Time-lapse liquid-phase TEM images showing the layer-by-layer growth of superlattice from nanospheres. Particles in the advancing surface layer are labeled with dots color-coded by their coordination numbers. Dose rate 17.6 $e^{-}Å^{-2}s^{-1}$. Bottom: Voronoi cell partition and orientation maps of the nanospheres. Each Voronoi cell is colored according to the orientation ϕ_j of each nanospheres. Scale bars: 100 nm.

Methods

Synthesis of Gold Nanorods. The gold concave nanocubes, nanocubes (the regular ones bounded with six {100} facets), and nanospheres were synthesized with our adaptions to a universal seeded growth.[46] The synthesis includes three steps: (i) preparation of gold nanorods, (ii) preparation of monodisperse spherical seeds from the gold nanorods by iterative etching and regrowth, and (iii) growth of the product nanoparticles from the monodisperse spherical seeds. The gold nanorods were synthesized following a literature method.[185] First, a seed solution was prepared by adding aqueous solutions of CTAB (100 mM, 5 mL) and $HAuCl_4$ (10 mM, 125 µL) in sequence to a 20 mL vial under 500 rpm stirring at room temperature. The stirring was then increased to 1150 rpm, followed by rapid injection of freshly prepared ice-cold $NaBH_4$ solution (10 mM, 300 µL). This ice-cold $NaBH_4$ solution was prepared by adding 1 mL of an aqueous solution of $NaBH_4$ (100 mM) into a 20 mL vial containing 9 mL water precooled in an ice bath, followed by vortex. The reaction solution was stirred at 1150 rpm for 1 min at room temperature and left undisturbed at 30 °C for 20–30 min to obtain seeds for use in the nanorod growth. Next, a gold nanorod growth solution was prepared by adding aqueous solutions of $HAuCl_4$ (10 mM, 20 mL), $AgNO_3$ (10 mM, 3.6 mL), L-ascorbic acid (100 mM, 2.28 mL), and 480 µL of the as-synthesized seed solution in sequence into a 1 L Erlenmeyer flask containing 400 mL aqueous solution of CTAB (100 mM) under 300–400 rpm stirring at 30 °C. The growth solution was stirred for another 1 min to promote mixing and then left undisturbed at 30 °C. After 2 h of growth, the solution turned dark brown, suggesting completion of the reaction. The gold nanorods were collected by transferring the growth solution into 12 centrifuge tubes (50 mL, Dow Corning), which were centrifuged twice (Eppendorf Centrifuge 5804; 8000 rpm, 15 min each) to remove residue reactants. After the first centrifugation, the supernatant was removed. The remaining sediment in each tube was redispersed in 50 mM CTAB and combined to 2 centrifuge tubes (20 mL solution each). After the second centrifugation, the supernatant was removed. The remaining sediment in each tube was redispersed in 50 mM CTAB and combined into one tube (10 mL) as the collected gold nanorod solution. This solution was diluted using 50 mM CTAB (~ 100 mL) to achieve a final gold nanorod concentration with an extinction intensity of 2 at the peak wavelength (704 nm) of the UV-Vis spectrum of the solution.

Monodisperse Spherical Seeds from Iterative Etching and Regrowth. The spherical seeds used to grow our final product gold nanoparticles of different shapes were synthesized via iterative reductive growth and oxidative etching to improve monodispersity.[46] In a typical synthesis, an aqueous solution of $HAuCl_4$ (10 mM, 928 µL) was added to the gold nanorod solution (103.1 mL) in a 250 mL Erlenmeyer flask under 200 rpm stirring at 40 °C. $AuCl_4^-$ and CTAB together can induce oxidative etching of gold nanorods into spherical seeds. The volumes of the $HAuCl_4$ and nanorod solutions added were optimized on a small-scale test reaction (using 0.5 mL nanorod solution) according to a literature.[46] The etching proceeded for 4 h under 200 rpm stirring at 40 °C, during which the color of the solution changed from brown to light pink. This solution was then transferred into 4 centrifuge tubes (50 mL), and centrifuged twice (11000 rpm, 45 min; 11000 rpm, 30 min) to collect the gold spherical seeds. After the first centrifugation, the supernatant was removed. The remaining sediment was redispersed in an aqueous solution of 100 mM CPC and combined to 2 centrifuge tubes (20 mL solution each). After the second centrifugation, the supernatant was removed. The remaining sediment was redispersed in 100 mM CPC (~ 17 mL) to achieve a gold spherical seed concentration with an extinction intensity of 1 at the peak wavelength (524 nm) in the UV-Vis spectrum of the solution, which we used in the next step. To further improve monodispersity, the gold spherical seeds underwent one subsequent round of reductive growth and oxidative etching. First, aqueous solutions of CPC (10 mM, 56.67 mL), $HAuCl_4$ (10 mM, 992 µL), L-ascorbic acid (100 mM, 12.75 mL), and 17 mL of the gold spherical seed solution obtained above were added in sequence to a 125 mL Erlenmeyer flask under 300 rpm stirring at 40 °C, to induce the growth of the spherical seeds into concave rhombic dodecahedron (CRD). This reaction proceeded for 15 min with no stirring, and the solution was then transferred into 4 centrifuge tubes (50 mL), and centrifuged twice (10000 rpm, 10 min each) to remove residue reactants and collect CRDs. After the first centrifugation, the supernatant was removed. The remaining sediment was redispersed in 50 mM CTAB and combined to 2 centrifuge tubes (20 mL solution each). After the second centrifugation, the supernatant was removed. The remaining sediment of CRDs was redispersed in 50 mM CTAB (~ 70 mL) to achieve a CRD concentration with an extinction intensity of 1 at the peak wavelength (539 nm) in the UV-Vis spectrum of the solution. Next, the CRDs underwent the oxidative etching. An aqueous solution of $HAuCl_4$ (10 mM, 426 µL) was added to the CRD solution obtained above (71.04 mL) in a 125 mL Erlenmeyer flask under 200 rpm stirring at 40 °C to etch CRDs into monodisperse spherical seeds. The etching proceeded for 4 h and the solution was then transferred into 4 centrifuge tubes (50 mL), and centrifuged twice (11000 rpm, 30 min each). After the first centrifugation, the supernatant was removed. The remaining sediment was redispersed in 100 mM CPC and combined to 2 centrifuge tubes (9 mL solution each). After the second centrifugation, the supernatant was removed. The remaining sediment was redispersed in 100 mM CPC (~ 10 mL) to achieve a gold spherical seed concentration with an extinction intensity of 1 at the peak wavelength (524 nm) in the UV-Vis spectrum of the solution. This solution serves as the highly monodisperse seeds (diameter: 24.4 ± 1.2 nm) that we used to grow the gold concave nanocubes, nanocubes and nanospheres.

Gold Concave Nanocubes Synthesized from Gold Spherical Seeds. The gold concave nanocubes were synthesized from the monodisperse gold spherical seeds.[46, 179] Aqueous solutions of CPC (100 mM, 5 mL), HCl (1 M, 250 µL, 99.999%, Alfa Aesar), $HAuCl_4$ (10 mM, 250 µL), $AgNO_3$ (10 mM, 62.5 µL), L-ascorbic acid (100 mM, 47.5 µL), and 620 µL of the gold spherical seed solution were added in sequence to a 20 mL vial with gentle shaking at room temperature. The volume of the spherical seed solution can be adjusted based on the targeted product particle size (more seeds leading to smaller product particles). The vial was loosely capped and left undisturbed for 2 h to grow the concave nanocubes. The solution was then transferred into one centrifuge tube (15 mL, Dow Corning), and centrifuged twice (3000 rpm, 5 min each) to collect the concave nanocubes. After the first centrifugation, the supernatant was removed. The remaining sediment was redispersed in 5 mL water. After the second centrifugation, the supernatant was removed. The remaining sediment (concave nanocubes) was redispersed in 50 mM CTAB (5 mL) for temporary storage and later ligand exchange. The UV-Vis spectrum of this solution shows an extinction peak at 637 nm (extinction intensity ~ 1.3 after half dilution). The gold concave nanocubes have an edge length L of 62.0 ± 4.6 nm from measuring 400 particles in the transmission electron microscopy (TEM) images.

Gold Nanocubes Synthesized from Gold Spherical Seeds. The gold nanocubes were synthesized from the monodisperse gold spherical seeds.[46, 179] Aqueous solutions of CPC (100 mM, 5 mL), KBr (100 mM, 500 µL), $HAuCl_4$ (10 mM, 100 µL), L-ascorbic acid (100 mM, 150 µL), and 70 µL of the gold spherical seed solution were added in sequence to a 20 mL vial with gentle shaking at room temperature. The vial was loosely capped and left undisturbed for 1 h to grow the nanocubes. The solution was then transferred into one centrifuge tube (15 mL), and centrifuged twice (5300 rpm, 5 min; 3750 rpm, 5 min) to collect the nanocubes. After the first centrifugation, the supernatant was removed. The remaining sediment was redispersed in 5 mL water. After the second centrifugation, the supernatant was removed. The remaining sediment (nanocubes) was either redispersed in 50 mM CTAB (5 mL) for temporary sample storage, or redispersed in water followed by immediate ligand exchange. The UV-Vis spectrum of the nanocubes stored in CTAB shows an extinction peak at 562 nm (extinction intensity ~ 0.6 after half dilution). The gold nanocubes have an edge length of 62.7 ± 5.4 nm as measured from the scanning electron microscopy (SEM) images.

Gold Nanospheres Synthesized from Gold Spherical Seeds. To synthesize the gold nanospheres used for liquid-phase TEM imaging, the monodisperse gold spherical seeds first underwent one more round of reductive growth and oxidative etching to achieve a gold spherical seed (of even higher monodispersity) concentration with an extinction intensity of 1 at the peak wavelength (524 nm) in the UV-Vis spectrum of the solution. This spherical seed solution was further used to grow into nanospheres, where aqueous solutions of CPC (10 mM, 80 mL), $HAuCl_4$ (10 mM, 1.4 mL), L-ascorbic acid (100 mM, 18 mL) and 4.3 mL of the gold spherical seed solution were added in sequence to a 125 mL Erlenmeyer flask under 300 rpm stirring at 40 °C. The growth was continued for 15 min without stirring and then transferred into 4 centrifuge tubes (50 mL), and centrifuged twice (4500 rpm, 10 min each) to remove residue reactants. After the first centrifugation, the supernatant was removed. The remaining sediment was redispersed in 50 mM CTAB and combined to 2 centrifuge tubes (25 mL solution each). After the second centrifugation, the supernatant was removed. The remaining sediment was redispersed in 50 mM CTAB to achieve an extinction intensity of 2 at 574 nm in the UV-Vis spectrum. Next, an aqueous solution of $HAuCl_4$ (10 mM, 138.9 µL) was added to this solution (46.29 mL) in a 125 mL Erlenmeyer flask under 200 rpm stirring at 40 °C to grow gold nanospheres. The reaction proceeded for 4 h.

The solution was then transferred into 2 centrifuge tubes (50 mL), and centrifuged twice (4500 rpm, 8 min each). After the first centrifugation, the supernatant was removed. The remaining sediment was redispersed in 100 mM CPC and combined to one centrifuge tube (25 mL). After the second centrifugation, the supernatant was removed. The remaining sediment was redispersed in 7.5 mL CPC solution (100 mM) for later usage. The UV-Vis spectrum of this nanosphere solution shows an extinction peak at 541 nm (extinction intensity ~ 1). The gold nanospheres have a diameter of 76.0 ± 2.2 nm as measured from the TEM images.

Thiol Modification of the Gold Concave Nanocubes, Nanocubes, and Nanospheres. All the gold nanoparticles (concave nanocubes, nanocubes, and nanospheres) underwent a ligand exchange with carboxylate-terminated thiols ($HS(CH_2)_{11}(OC_2H_4)_6OCH_2COOH$) to improve the nanoparticles' stability before liquid-phase TEM imaging, following literature procedures.[30, 137] For the concave nanocubes, 2.5 mL of the concave nanocube solution was diluted in 50 mM CTAB (5 mL). The solution (7.5 mL) was transferred into a centrifuge tube (15 mL) and centrifuged twice (3000 rpm, 8 min each) to lower the CTAB concentration. After the first centrifugation, the supernatant was removed, and the remaining solution with sediments (~ 20 μL) were redispersed in 5 mL water. After the second centrifugation, the supernatant was removed, and the remaining sediments (~ 20 μL) of the concave nanocubes were redispersed in water (3 mL, final CTAB concentration: 3 μM). Next, an aqueous solution of thiols (7.93 mM, 44.26 μL) was added to the concave nanocube solution. The 7.93 mM thiol solution was prepared by dissolving 5 μL thiol as received in 1 mL water. The mixture sat undisturbed for 30 min first and was then sonicated for 5 s and added with 0.344 mL 1 M phosphate buffer solution (PBS, pH = 8, composed of 70 mM sodium phosphate monobasic monohydrate and 930 mM sodium phosphate dibasic anhydrous) slowly by pipetting. The addition of PBS screens the electrostatic repulsion between charged thiols, facilitating their packing onto the concave nanocube surface and causing reversible assembly of the concave nanocubes for concentrating. The solution was left undisturbed overnight, after which sediments (assembled concave nanocubes) appeared on the bottom and the wall of the centrifuge tube while the upper solution turned colorless. We removed 1.0 mL of the upper solution. The remaining solution was mixed well by pipetting and left undisturbed for one day to accumulate more sediments for liquid-phase TEM. After that, we pipetted out ~ 24 μL sediments, which were redispersed in 200 μL water into a green solution indicative of dispersed concave nanocubes. This green solution was left undisturbed for a few more days, during which time the concave nanocubes concentrated to the tube bottom due to gravitation. Next, ~ 184 μL of the colorless upper solution was removed to further concentrate the concave nanocubes. This final concentrated solution of dispersed gold concave nanocubes (solution 1) was used in liquid-phase TEM imaging. We find solution 1 stable for liquid-phase TEM experiments for one year. The final PBS concentration of solution 1 is ~ 10 mM. For the nanocubes, the nanocubes after the second centrifugation was redispersed in 6 mL water to achieve an extinction intensity ~ 1 at 562 nm of the UV-Vis spectrum. Then ~ 3.05 mL of this diluted solution was transferred into a centrifuge tube (15 mL) for ligand exchange. An aqueous solution of thiols (7.93 mM, 44.26 μL) was added to the tube. The mixture sat undisturbed for 30 min first, sonicated for 5 s, and 0.344 mL of 1 M PBS (pH = 8) was added slowly by pipetting. The solution was left undisturbed overnight to accumulate sediments. After overnight, 2.0 mL of the upper solution was removed, and ~ 12 μL black sediments were pipetted out and redispersed in 100 μL water into a red solution indicative of dispersed nanocubes. This red solution was was left undisturbed for a few days, during which time the dispersed nanocubes concentrated to the tube bottom. Next, ~ 60 μL of the colorless upper solution was removed. This final concentrated solution of dispersed gold nanocubes (solution 2) was used in liquid-phase TEM imaging. The final PBS concentration of solution 2 is ~ 10 mM. For the nanospheres, 7.5 mL of the nanosphere solution was centrifuged twice (4400 rpm, 8 min each) to lower the CPC concentration. After the first centrifugation, the supernatant was removed, and the remaining solution with sediments (~ 100 μL) was redispersed in 4.9 mL water. After the second centrifugation, the supernatant was removed, and the remaining sediments of gold nanospheres (~ 50 μL) were redispersed in 3 mL water for ligand exchange. Next, an aqueous solution of thiols (7.93 mM, 44.26 μL) was added into the nanosphere solution. The mixture sat undisturbed for 30 min first, sonicated for 5 s, and 0.344 mL of 1 M PBS (pH = 8) was added slowly by pipetting. The solution was left undisturbed for two days. After that, all the upper solution was gently removed, the remaining solution (~ 28 μL) was diluted in 400 μL water into a red solution indicative of dispersed nanospheres. The solution was left undisturbed for a few days, during which time the dispersed nanospheres concentrated to the tube bottom. Next, ~ 376 μL of the colorless upper solution was removed. This final concentrated solution of dispersed gold nanospheres (solution 3) was used in liquid-phase TEM imaging. The final concentration of PBS in solution 3 is ~ 7 mM.

Liquid-Phase TEM Imaging. The liquid-phase TEM imaging was performed using a Hitachi 9500 TEM with a LaB_6 emitter at 200 kV and an electrochemical liquid flow TEM holder (Hummingbird Scientific). The SiN_x microchips used in our experiments were purchased from Hummingbird Scientific (250 nm spacer bottom microchip: 50 μm × 200 μm × 50 nm; rectangular top microchip: 30 μm × 650 μm × 50 nm). Right before the microchip assembly, the flow tubing was wet with water, and the microchips were treated with oxygen plasma (Harrick Plasma Cleaner PDC-23G) at low RF level for 27–29 s to clean their surfaces and render them hydrophilic. The liquid-phase TEM movies were captured with a Gatan Orius fiber-optically coupled CCD camera with an exposure time of 0.1–0.2 s. Mostly a spot size of Micro1 was used for direct imaging. The frame rate for capturing the movies was set as 5–10 frames per second (fps). The electron beam dose rate was controlled by manipulating the electron beam size, magnification, and the first condenser lens (C1). The dose rate was calculated from total pixel intensity of an acquired image with samples out following:

$$\text{Dose rate } (e^{-}\text{Å}^{-2}\text{s}^{-1}) = \frac{\text{Total pixel intensity}}{\text{Acquisition area} \times \text{Exposure time}} \times (1/\text{conversion factor})$$

The conversion factor was measured as 9.38 count per e^{-} using a Faraday cup.

Liquid-Phase TEM Imaging of Gold Concave Nanocubes. Right before loading the liquid sample to a microchip, solution 1 was concentrated for growing large-scale superlattices. Specifically, 1.36 μL PBS solution (150 mM, pH = 8) was added to 5 μL of solution 1 (final PBS concentration: 40 mM), which screens interparticle electrostatic repulsion and induces the assembly of the concave nanocubes. Next, ~ 0.1 μL of the particle solution was immediately pipetted onto the bottom SiN_x microchip and covered by the top SiN_x microchip to prepare the liquid chamber. After the microchip assembly, 40 mM PBS solution was flowed into the liquid chamber for 2 h at a speed of 5 μL/min. This step ensures an accurate PBS concentration (40 mM) in the sample to account for possible solvent evaporation during microchip assembly. Following the concave nanocube loading method detailed above and a flow of 40 mM PBS for 2 h, the growth of superlattices can be triggered by flowing water into the liquid chamber (5 μL/min) during TEM imaging. In this process, the lowered ionic strength due to water flow can disassemble the pre-assembled concave nanocubes into dispersed ones, while within the illuminated region, ions generated from radiolysis increase the ionic strength[30] to concentrate the dispersed concave nanocubes for crystallization.[17, 186] The superlattice growth started after ~ 10 min of water flow. The water flow was stopped when the superlattice growth was observed. This procedure works robustly to induce superlattice growth lasting 5–25 min in independent experiments, demonstrating a wide ionic strength window for the superlattice growth. Note that when the ionic strength is too high (e.g., 8 min after water flow), dendrite growth (**Figure 4.13**) from irreversible attachments of the concave nanocubes was observed, due to strong interparticle attraction at high ionic strength. When the ionic strength is too low (e.g., ~ 40 min after water flow), we observed the adsorption of concave nanocubes onto the SiN_x microchip due to strong particle–substrate adhesion. We attribute this strong adhesion at low ionic strength to the electrostatic attraction between negatively charged concave nanocubes and positively charged SiN_x surface,[5] which was otherwise screened when the PBS concentration was high. After more than 40 min water flow, the concave nanocubes became adsorbed and stuck to the substrate, which can be reagitated to induce the superlattice growth by flowing 40 mM PBS solution (5 μL/min). The PBS flow screens the particle–substrate adhesion to release the adsorbed concave nanocubes back to solution. The increased ionic strength also screens the interparticle electrostatic repulsion so that the particles assemble into superlattices. The superlattice growth started after ~ 10 min of flowing PBS solution, both within and out of the beam illuminated region. The PBS flow was stopped when we captured the movies. For analyzing the intralayer diffusion, we chose to study the equilibrated superlattice formed at a well-defined ionic strength I ($I = 110$ mM) right after we loaded the concave nanocubes and flowed the 40 mM PBS solution for 2 h. At this stage, for prolong imaging (> 6 s), ions accumulated from radiolysis of water[30] can cause a lattice retraction (**Figure 4.14**), and we only used the data before the retraction for the intralayer diffusion analysis. A dose rate of 3.6–17.9 e^{-} $Å^{-2}s^{-1}$ was used to image the intralayer diffusion. We measured the lattice spacing of the grown superlattice based on the TEM images obtained at $I = 110$ mM as 70.8 ± 0.8 nm, which was used to validate our molecular dynamics simulations (**Table 4.1**) relating I with d_{equil}, the lattice spacing predicted from the simulations, i.e., the equilibrium center-to-center distance, where the pairwise interparticle interaction reaches minimum.

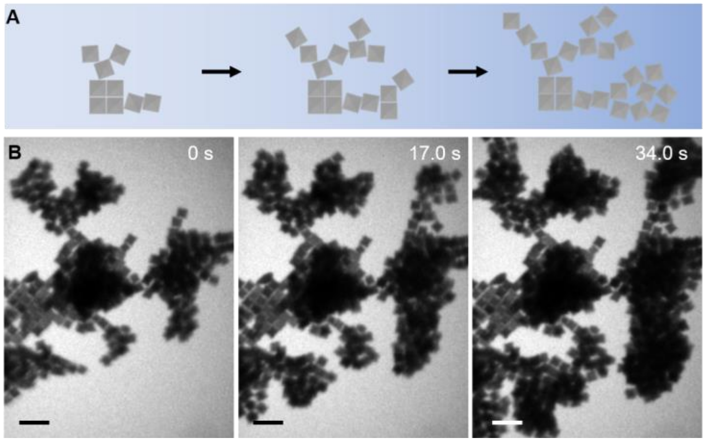

Figure 4.13. Irreversible attachments of the gold concave nanocubes at high ionic strengths. Schematics (A) and time-lapse liquid-phase TEM images (B) showing the formation of irregular aggregates at the early stage during water flow (high ionic strength). Scale bars: 200 nm.

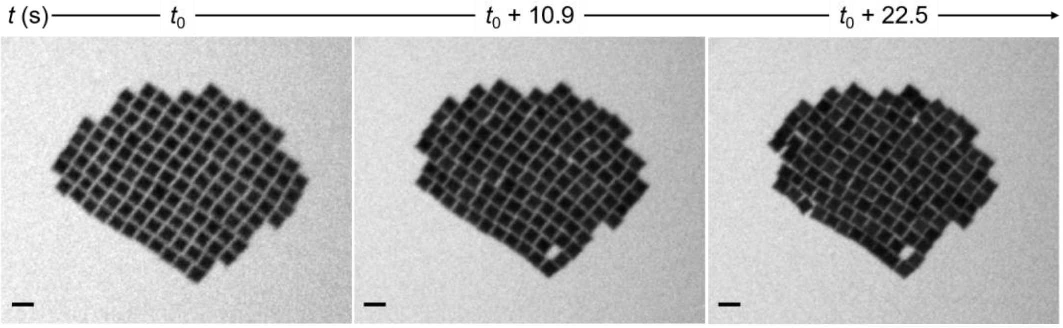

Figure 4.14. Electron beam-induced lattice contraction. Time-lapse liquid-phase TEM images showing the superlattice contraction after long-time electron beam illumination. Ionic strength: 80–110 mM. Scale bars: 100 nm.

Table 4.1. Lattice spacing d_{equil} measured from liquid-phase TEM and the corresponding effective ionic strengths by matching the experimentally measured d_{equil} with simulation results.

Conditions	d_{equil} measured from experiments (nm)	Effective ionic strength from calculations (mM)
Intralayer diffusion	70.8 ± 0.8	80 – 110
Layer-by-layer growth	73.7 ± 1.2	25 ± 5
2D square lattice	75.4 ± 1.7	15 ± 5
3D cubic lattice	75.4 ± 0.7	15 ± 5
Roughening transition	75.6 ± 0.9	15 ± 5

Liquid-Phase TEM Imaging of Gold Nanocubes. For gold nanocubes, right before liquid-phase TEM imaging, 1.36 μL PBS solution (150 mM, pH = 8) was added to 5 μL of solution 2. Next ~ 0.1 μL of this solution was immediately pipetted onto the bottom SiN_x microchip and covered by a top SiN_x microchip. After the microchip assembly, 40 mM PBS solution was flowed through the liquid flow holder for 2 h (5 μL/min). The layer-by-layer growth of the superlattices was triggered by flowing water into the liquid chamber (5 μL/min) during TEM imaging. The superlattice growth started after ~ 25 min of water flow. A dose rate of 15.5 $e^{-}Å^{-2}s^{-1}$ was used to image the superlattice growth.

Liquid-Phase TEM Imaging of Gold Nanospheres. For gold nanospheres, right before liquid-phase TEM imaging, 0.19 μL PBS solution (1 M, pH = 8) was added to 1.8 μL of solution 3. Next ~ 0.1 μL of this solution was pipetted onto the bottom SiN_x microchip and covered by a top SiN_x microchip. After the microchip assembly, 100 mM PBS solution was flowed through the liquid flow holder for 2 h (5 μL/min). The layer-by-layer growth of superlattices was triggered by flowing water into the liquid chamber (5 μL/min) during TEM imaging. The superlattice growth started after ~ 20 min of water flow. A dose rate of 17.6 e^{-}Å^{-2}s^{-1} was used to image the superlattice growth.

Other Experimental Characterizations of the Nanoparticles. A Hitachi S-4800 SEM and a JEOL 2100 TEM were used for characterization of the size and morphology of the nanoparticles and superlattices in the dry state. Nanobeam diffraction and tilt series of TEM images of the single concave nanocube were obtained using single-tilt holder on the JEOL 2100 TEM. UV-Vis spectra were measured using a Scinco S-4100 PDA spectrophotometer with a quartz cuvette (path length = 1 cm). The surface charge density (ρ_s) of the thiol coated nanoparticles was derived from their mobility (μ) under electric field measured by a Malvern zetasizer,[30] following $\rho_s = \mu\nu\kappa$, where ν is the dynamic viscosity of the medium and κ is the inverse of the Debye length. The surface charge densities of the nanoparticles are –0.012 C/m^2 (–0.075 e/nm^2) for the concave nanocubes, –0.014 C/m^2 for the nanocubes, and –0.008 C/m^2 for the nanospheres.

Coarse-Grained (CG) Model for the Gold Concave Nanocubes. To compute the pairwise interaction of two concave nanocubes, we constructed a CG model in which each gold concave nanocube core is discretized as a mesh of beads (red), placed on a three-dimensional (3D) simple cubic lattice with a lattice spacing of σ_{gold} = 0.332 nm (diameter of a gold atom). The concaveness (α = 16°) of the concave nanocube was considered in the meshing. Each charged ligand coated on the gold surface was characterized by the bead–spring model with 5 beads of size σ_{lig} = 1.25 nm connected by harmonic springs. The number and size of the beads were determined using the ideal chain model by considering the Kuhn lengths (~ 1.25 nm) of the polymer segments.[187] The head bead (green) of the ligand chain is rigidly attached on the gold surface and the tail bead (yellow) carries a unit negative charge (–e). The ligand density ρ_s was set to be –0.075 e/nm^2, as measured in our experiment. The beads making up the gold core have a bead–bead van der Waals interaction $u_{\mathrm{vdW}}(r_{\mathrm{b-b}})$, and the tail beads of the ligands interact via a screened Coulomb potential $u_{\mathrm{el}}(r_{\mathrm{b-b}})$ which we modeled following Debye–Hückel approximation, where $r_{\mathrm{b-b}}$ denotes the distance between the pairs of interacting beads. The van der Waals interactions between ligands and between ligands and gold atoms are negligible owing to the very small Hamaker constants for hydrocarbon/hydrocarbon and gold/hydrocarbon across water.[158] The interactions $u_{\mathrm{vdW}}(r_{\mathrm{b-b}})$ and $u_{\mathrm{el}}(r_{\mathrm{b-b}})$ are given by

$$u_{\mathrm{vdW}}(r_{\mathrm{b-b}}) = -\frac{H{\sigma_{\mathrm{gold}}}^{6}}{\pi^{2} r_{\mathrm{b-b}}^{6}},$$

$$u_{\mathrm{el}}(r_{\mathrm{b-b}}) = \frac{e^{2}}{4\pi\varepsilon_{0}\varepsilon_{\mathrm{r}} r_{\mathrm{b-b}}} e^{-\kappa r_{\mathrm{b-b}}} = \frac{l_{B}}{r_{\mathrm{b-b}}} e^{-\kappa r_{\mathrm{b-b}}} k_{\mathrm{B}}T \, ,$$

where $H = 28.9\ k_{\mathrm{B}}T$ is the Hamaker constant for gold/gold in water, ε_{0} the vacuum permittivity, ε_{r} the relative permittivity of water, κ^{-1} the Debye length following $\kappa^{-1} = 0.304/\sqrt{I(\mathrm{M})}$ nm (with ionic strength I in unit of M) for aqueous solutions at room temperature, $l_{\mathrm{B}} = 0.7$ nm the Bjerrum length of water at 25 °C. Note that cutoff value of 70 nm bead–bead distance was chosen in the van der Waals interaction computation for computation efficiency and the truncation error was tested to be less than 0.2 $k_{\mathrm{B}}T$ for interparticle interaction energy (**Table 4.2**). A shift-truncated Lennard-Jones potential $u_{\mathrm{LJ}}(r_{\mathrm{b-b}})$ was applied to all the beads to model the excluded-volume interactions:

$$u_{\mathrm{LJ}}(r_{\mathrm{b-b}}) = \begin{cases} 4\varepsilon\left[\left(\frac{\sigma}{r_{\mathrm{b-b}}}\right)^{12} - \left(\frac{\sigma}{r_{\mathrm{b-b}}}\right)^{6}\right] + \epsilon, & (r_{\mathrm{b-b}} \le 2^{1/6}\sigma) \\ 0, & (r_{\mathrm{b-b}} > 2^{1/6}\sigma) \end{cases},$$

where the energy scale $\varepsilon = k_{\mathrm{B}}T$, $\sigma = \sigma_{\mathrm{gold}}$, σ_{lig}, $(\sigma_{\mathrm{gold}} + \sigma_{\mathrm{lig}})/2$ for gold–gold, ligand–ligand, gold–ligand bead pairs, respectively. The bonds between neighboring beads along a ligand chain were modeled with a harmonic potential:

$$u_{\mathrm{bond}}(r_{\mathrm{b-b}}) = K(r_{\mathrm{b-b}} - \sigma_{\mathrm{lig}})^2,$$

where $K = 25\ k_{\mathrm{B}}T/\mathrm{nm}^2$ is the spring constant and σ_{lig} sets the native spring length. All simulation parameters are summarized in **Table 4.3**. It is noteworthy that both the geometrical details (e.g., concaveness) of the concave nanocube and the discreteness of ligand molecules (e.g., steric effects) can significantly affect the magnitude and range of the effective interparticle interaction at this nanoscale. Therefore, including these features in the modeling is crucial in order to provide quantitative predictions of the energy landscape and the lattice spacing of the superlattices. For the same reason, the hard-core models[3] which have been widely used in simulating anisotropic nanoparticles are not feasible here.

Table 4.2. Interparticle van der Waals interaction energies (in unit of $k_{\mathrm{B}}T$) at different interparticle center-to-center distance d computed using different bead–bead cutoff distances.

	d = 68.0 nm	d = 70.0 nm	d = 71.0 nm	d = 74.0 nm
Cutoff = 35 nm	–10.01	–5.47	–4.14	–1.88
Cutoff = 70 nm (chosen)	–11.97	–7.24	–5.82	–3.28
Cutoff = 80 nm	–12.05	–7.32	–5.90	–3.36
Cutoff = 100 nm	–12.10	–7.37	–5.95	–3.41

Table 4.3. The parameters used in the molecular dynamics simulations.

Parameter	Description	Value
σ_{gold}	Diameter of gold atoms	0.332 nm
H	Hamaker constant (gold-gold across water)	28.9 k_BT
L	Concave nanocube edge length	62.0 nm
α	Concave nanocube concaveness	16°
σ_{lig}	Diameter of a bead in the bead–spring model for ligands	1.25 nm
	Number of beads per ligand	5
K	Spring constant in the bead–spring model for ligands	25 k_BT/nm^2
l_{B}	Bjerrum length	0.7 nm
ρ_{s}	Charge density of a concave nanocube	–0.075 e/nm^2
T	Temperature	298 K

Molecular Dynamics Simulations of the Gold Concave Nanocubes. Molecular dynamics simulations were conducted for the concave nanocubes coated with ligands in the *NVT* ensemble. All simulations were performed at 298 K using a Langevin thermostat at different ionic strengths from 15 mM to 110 mM, within which the Debye–Hückel approximation is valid. All systems were simulated with a 0.01-fs time step for 2.5 ns during equilibration and a 0.05-fs time step for 500 ns during production. Ten independent runs were conducted for each condition to obtain ensemble averages. To calculate the total pairwise interaction energy E_{tot} of two concave nanocubes, one important component of E_{tot} we considered is the entropic steric repulsion E_{steric} between the ligands, which occurs as the ligands of two approaching concave nanocubes start to overlap. To measure E_{tot} as a function of the interparticle center-to-center distance d (when the two concave nanocubes are oriented in parallel), we ran multiple simulations with the two concave nanocubes positioned at different values of d. In each simulation, both the position and orientation of two concave nanocube cores are fixed, while the ligand chains are free to move and relax. We measured the ensemble-averaged total force between the concave nanocubes at each given d. Total energy profile $E_{\text{tot}}(d)$ was then computed through integration of the force profile. Since the ensemble-averaged potential energy $E_{\text{vdW}} + E_{\text{el}}$ as a function of d is straightforward to extract from the simulations, E_{steric} was obtained from $E_{\text{steric}} = E_{\text{tot}} – E_{\text{vdW}} – E_{\text{el}}$ for discussions in **Figure 4.1A** and **Figure 4.4**. Note that E_{steric} consists of two parts: the ensemble-averaged excluded-volume interaction energy and the entropic contribution from ligand molecules ($–TS_{\text{lig}}$, S_{lig}: ligand entropy; T: temperature). After obtaining the profile of E_{tot} versus d, the equilibrium interparticle center-to-center distance (d_{equil}) was identified as the distance d at the minimum of E_{tot}, which is our prediction for the lattice spacing. The energy of adsorption per face-to-face contact (E_{ads}) is approximated by the minimum of E_{tot} by assuming the interactions with second nearest neighbors are negligible. A similar approach was adopted to measure the energy landscape experienced by a tracer concave nanocube on top of the superlattice during the interlayer exchange (**Figure 4.5F**). At $I = 25$ mM (i.e., the layer-by-layer growth condition), the predicted lattice spacing d_{equil} is 73.5 nm (determined in simulations as noted above, matching well with 73.7 nm measured in experiments) and the ligands on the neighboring concave nanocubes are barely touching ($d_{\text{equil}} > L + 2l_{\text{max}} = 73.25$ nm with $l_{\text{max}} = 5.625$ nm as the length of a fully extended ligand molecule). Therefore, E_{steric} can be ignored and E_{tot} reduces to the ensemble-averaged $E_{\text{vdW}} + E_{\text{el}}$, which was computed between the tracer concave nanocube and the concave nanocubes underneath in the superlattice. Similar to our simulations of two concave nanocubes, the position and orientation of all the concave nanocubes are fixed, while the ligand chains are free to relax. We ran simulations with the tracer concave nanocube sitting at different horizontal lattice coordinates *a* (*a* = *a'*/d_{equil} where *a'* is the horizontal displacement of the tracer concave nanocube with respect to the nearest underlying concave nanocube, see **Figure 4.5B**) while keeping the configuration of the underlying lattice unchanged. We selected two typical paths of the tracer concave nanocube (inset of **Figure 4.5F**). Path 1 involves a 90° rotation of the tracer concave nanocube at the step edge, which lowers the step–edge barrier for the interlayer exchange. Conversely, path 2 involves no rotation where the tracer concave nanocube vertically drops along the step, resulting in a larger step–edge barrier. Note that we assume the vertical distance between the tracer concave nanocube and the concave nanocube layer underneath is 73.5 nm irrespective of *a*, since the energy landscape near a flat lattice surface is insensitive with *a* (cf. in-plane energy landscape part of **Figure 4.5F**).

Analytical Models. To simulate the system with different interaction ranges Δ, we need to obtain the corresponding values of ΔE^{in}, E^{b} and ΔE^{SE} resulting from the energy landscape for each Δ. Thus, we built up a simple analytical model where the pairwise interaction between particles follows the functional form

$$E(n,r) = \begin{cases} -\dfrac{\epsilon}{(r/\sigma)^n} \ (r \geq \sigma) \\ +\infty \ (r < \sigma) \end{cases},$$

with a tunable attraction part plus a hard repulsion, where σ denotes the particle size and our length unit, ϵ is the energy minimum at contact and our energy unit, and *n* determines the attraction range. Here the interaction range Δ is defined as $\Delta = \left(2^{1/n} - 1\right)\sigma$, such that the pairwise energy is lower than $-\epsilon/2$ within the distance $[\sigma, \Delta + \sigma]$. The energy landscape can be mapped out by moving a tracer particle on top of a partially filled lattice and recording the energy value from direct summation. Key energetic parameters ΔE^{in}, E^{b} and ΔE^{SE} can thus be extracted from the potential landscape. To simulate micron-sized colloids with a very small interaction range (e.g., $\Delta \leq 0.05$), an additional entropic step–edge barrier was also included in ΔE^{SE}. Here this entropic barrier is of the magnitude of $\ln 2 \cdot k_{\mathrm{B}}T$ as the step–edge diffusion path is twice longer than the in-plane path.[167]

Analysis of Interparticle Interaction and Equilibrium Spacing from Simulations. Molecular dynamics simulation elucidates that the face-to-face alignment of the concave nanocubes is energetically favored and that the lattice spacing (d_{equil}) can be well-predicted. As shown in **Figure 4.4A**, the face-to-face alignment of zero offset ($a = 0$) is energetically favored over a wide range of ionic strengths, consistent with the experiments. At I = 15–50 mM, d_{equil} measured from simulations is mostly contributed by the balance between E_{el} and E_{vdW}, following expectations of DLVO theory[91] (**Figure 4.1A**). For higher ionic strengths such as I = 110 mM, E_{el} is weakened by counter-ion screening and E_{steric} overwhelms E_{el} to counteract E_{vdW} (**Figure 4.4B**), resulting in a minimum of E_{tot} at d_{equil} = 71.0 nm. This value of d_{equil} matches with the lattice spacing (70.8 ± 0.8 nm) measured from the liquid-phase TEM images of the superlattices at I = 110 mM. This agreement confirms the increasing importance of the discreteness (e.g., entropic effects of ligands) at the nanoscale and necessity of including it in the modeling.[11] The lattice spacing predicted by our simulations (d_{equil}) was plotted as a function of I (**Figure 4.4C**), from which we derived the effective ionic strength in our liquid-phase TEM experiments based on the experimentally measured values of d_{equil} (**Table 4.1**).

Evaluation of pH Effect on the Surface Charge Density of the Gold Concave Nanocubes. The surface charge density of the gold concave nanocubes depends on the deprotonation of the carboxylate thiols on the particle surface. To calculate the deprotonation percentage at a given pH, we used the Henderson–Hasselbalch equation: $\mathrm{pH} = \mathrm{p}K_\mathrm{a} + \log([\mathrm{A}^-]/[\mathrm{HA}])$, where $[\mathrm{A}^-]$ and [HA] are the molar concentrations of $–\mathrm{COO}^-$ and –COOH groups. The $\mathrm{p}K_\mathrm{a}$ of the carboxylate–thiols is between 3.5 and 3.7 (provided by the manufacturer), and we used 3.5 in our calculation. From this equation, over 99% of carboxylate thiols are deprotonated at a pH higher than 5.5. In addition, the concave nanocubes are in 40 mM PBS (pH = 8) solution, which buffers the H^+ possibly generated from radiolysis of water during TEM imaging ($\mathrm{H_2PO_4^-} \rightleftharpoons \mathrm{H}^+ + \mathrm{HPO_4^{2-}}$, $\mathrm{p}K_\mathrm{a1} = 7.21$). In fact, the amount of additional H^+ needed to decrease the pH below 5.5 is at least 37 mM, which is two orders of magnitude higher than an overestimated H^+ generated from 200 $\mathrm{e^-Å^{-2}s^{-1}}$ dose rate in pure water[188] (overestimated due to our experimental dose rates < 30 $\mathrm{e^-Å^{-2}s^{-1}}$).

TEM Imaging Processing and Single Concave Nanocube Tracking. For all the TEM and SEM images presented in this work, we adjusted brightness and contrast using ImageJ. For the layer-by-layer growth movie of concave nanocubes and nanospheres and the associated TEM images, we slightly adjusted the gray scale colormap to highlight the individual nanoparticles in the lattice using Matlab. The TEM images in **Figure 4.5C** were processed by averaging the neighboring frames (9 frames for the 0.4 s image and 6 images for the 4.3 s image) to lower the background noise (**Figure 4.7A**). The TEM images in **Figure 4.14** were processed using Kalman Stack Filter in ImageJ to lower the background noise (Plugins→Stacks→ Kalman Stack Filter, Acquisition noise variance estimate: 0.05, Bias to be placed on the prediction: 0.80). A customized Matlab code was used to track the motions of the concave nanocubes in **Figure 4.5C**, with the workflow detailed in **Figure 4.7B**. Using one frame as an example, we first denoised the TEM image using the built-in function of imgaussfilt.m in Matlab and binarized it, followed by hole-filling of the binarized image (imfill.m in Matlab) to single out white features. Out of these features, only those with areas of 100–1200 pixel^2 (1 pixel = 1.7 nm) were identified as concave nanocubes. The features at the image boundary were eliminated using the imclearborder.m function in Matlab. The positions of the concave nanocubes were determined as the centroids of the features. Occasionally multiple concave nanocubes were recognized as one feature due to motion blurring, or the contour of individual concave nanocube was not recognized accurately due to image intensity fluctuation, which we manually corrected. For the concave nanocube tracking presented in **Figure 4.9G**, we first conducted Fourier transform of the images and adjusted the threshold to keep only the high values. Next, we inversed the Fourier transform using ImageJ and used the inversed images for particle tracking. We then denoised the TEM image using the built-in function of imgaussfilt.m in Matlab, and binarized the images using a series of threshold values. Then we used built-in function of imfindcircles.m in Matlab (with threshold and sensitivity set to 0.20 and 0.65, respectively) to identify the concave nanocubes from the processed images and track the position of each concave nanocube from the centroids of the fitted circles. When the centroid positions of two concave nanocubes are closer than 51.1 nm, we only kept one tracked position on the filtered images and deleted the other positions. For the concave nanocube tracking presented in **Figure 4.9E**, after inversing the Fourier transform, we further conducted a background subtraction to the inversed images and used the background subtracted images for particle tracking. We then denoised the TEM image using the built-in function of imgaussfilt.m in Matlab, and binarized the images using a series of threshold values. Then we used built-in functions of watershed.m and regionprops.m in Matlab to identify the concave nanocubes from the processed images and track the position of each concave nanocube from the centroids of the identified regions. When the centroid positions of two concave nanocubes are closer than 51.1 nm, we only kept one tracked position on the filtered images and deleted the other positions.

Analysis of the Structural Order and Particle Orientations in the Superlattices. To analyze the structural order of the superlattice, we first tracked the particle positions, from which we computed the radial distribution function $g(r)$ of the superlattice[117] as a function of r, the interparticle center-to-center distance of two particles regardless of their configuration (**Figure 4.3B**). We followed the previous literature[160] to perform periodic boundary correction to account for the limited viewing area. From the $g(r)$ versus r curve, a r_c at the first minimum of $g(r)$ was used to determine the threshold for the nearest-neighbor bond length. Only the particles with $r < r_c$ were recognized as linked *via* a nearest neighbor bond. The orientation (ϕ_j) of each particle (**Figures 4.1F, 4.12D and 4.12H**) was calculated following the form[123] of $\phi_j = \frac{1}{4}\arg\left(\frac{1}{Z_j}\sum_{k=1}^{Z_j}\exp^{i4\theta_{jk}}\right)$ for concave nanocubes (**Figure 4.1F**) and nanocubes (**Figure 4.12D**), or $\phi_j = \frac{1}{6}\arg\left(\frac{1}{Z_j}\sum_{k=1}^{Z_j}\exp^{i6\theta_{jk}}\right)$ for nanospheres (**Figure 4.12H**). Here, θ_{jk} is the orientation of the bond connecting particle j to its kth nearest neighbor, and Z_j is the number of nearest neighbors of particle j.

Analysis of the Intralayer Diffusion. To analyze the intralayer diffusion, the same tracking procedure was applied to extract the concave nanocube positions in **Figure 4.5C**. The trajectories of the concave nanocubes (**Figure 4.5C**) were obtained by linking their positions across frames following a literature algorithm.[189] The intralayer diffusion barrier was calculated from the positions of the *surface* concave nanocubes undergoing intralayer diffusions relative to a concave nanocube pair underneath. Specifically, the relative position coordinate was defined by linking the centers of the two concave nanocubes in the pair as the x axis with $x = 0$ positioned in the middle, and the vertical direction as y axis where the y coordinates of the surface particles stay positive (**Figure 4.7C**). Based on this relative position coordinate, we obtained the relative positions of surface concave nanocubes as shown in the scatter plot (**Figure 4.7D**). Lastly, we applied a Boltzmann distribution argument to calculate the relative free energy of the surface particles at different horizontal lattice coordinates a (statistics collapsed to $-0.5 < a < 0.5$) (**Figure 4.5D**). The free energy difference was then divided by 4 since four concave nanocubes were diffusing together in all the movies analyzed (**Figure 4.5C**).

Estimation of Intralayer Diffusion Rate. First, the intralayer diffusion rate of three concave nanocubes diffusing as a whole ($D^{\text{3cubes}} = 29.5\ d_{\text{equil}}^2/\text{s}$) was obtained from the linear fitting of the mean-squared displacement (MSD) versus time t plot (**Figure 4.6B**). To convert D^{3cubes} to the single-particle intralayer diffusion rate D^{intra}, we assume an Arrhenius-like expression of the diffusion rate, where $D^{\text{intra}} = D_0 \exp\left(-\Delta E^{\text{in}}/k_{\text{B}}T\right)$ and $D^{\text{3cubes}} = D_0^{\text{3cubes}} \exp\left(-3\Delta E^{\text{in}}/k_{\text{B}}T\right)$ with D_0 (or D_0^{3cubes}) being the intrinsic diffusion rate without any diffusion barriers and ΔE^{in} being the in-plane diffusion barrier for a single nanocube. To relate D_0^{3cubes} with D_0, we approximate the shape of the three concave nanocube entity by a cylinder. Based on Einstein relation, the intrinsic diffusion rate D of a cylinder in the low-Reynolds number (Re) fluid[190] (Re in our system is estimated as 10^{-3} to 10^{-9} depending on the velocity of the concave nanocube) is expressed as $D = k_{\text{B}}T/\xi$, with ξ being the drag coefficient. Since ξ is proportional to the length of the cylinder (i.e., the number of the constituent concave nanocubes), D_0^{3cubes} relates to D_0 by $D_0^{\text{3cubes}} = D_0/3$. Therefore, we obtain $D^{\text{intra}} = 3D^{\text{3cubes}} \exp\left(2\Delta E^{\text{in}}/k_{\text{B}}T\right)$. Plugging the value of ΔE^{in} ($\sim 0.2 k_{\text{B}}T$, measured at ionic strength 110 mM) into the previous expression, we have $D^{\text{intra}} = 132.0\ d_{\text{equil}}^2/\text{s}$.

Analysis of the Velocity Field in the Layer-By-Layer Growth and Roughened Growth. To analyze the velocity field, we first calculated the trajectories of the concave nanocubes (**Figure 4.11**) by linking their positions across frames. We also conducted a drifting correction to the trajectories by subtracting the average trajectory of all the particles in the frame. To obtain the velocity map shown in **Figure 4.9, E and G**, the displacements of the concave nanocubes between frames were first calculated and divided by the time interval of 1 s. The velocity field was then divided into two types based on their magnitude: Fast velocities ($|\mathbf{v}|>10$ nm/s) are colored by yellow, and small velocities ($|\mathbf{v}|<10$ nm/s) are colored by cyan. The threshold value (10 nm/s) was chosen according to the velocity distributions in **Figure 4.11, B and D**. We also calculated the orientational ($g_{\mathrm{ori}}(r)$) and magnitude correlation ($g_{\mathrm{mag}}(r)$) in the velocity fields (**Figure 4.9, D and F**). The orientational correlation is defined as $g_{\mathrm{ori}}(r) = \left\langle \cos\left(\theta_i - \theta_j\right) \right\rangle_{r<|\mathbf{r}_i-\mathbf{r}_j|<r+\Delta r}$, where θ_i is the angle between the velocity vector of concave nanocube *i* and the *x* axis. The magnitude correlation is defined as $g_{\mathrm{mag}}(r) = \frac{\langle m_i m_j \rangle - \langle m_i \rangle \langle m_j \rangle}{\sqrt{\left(\langle m_i^2 \rangle - \langle m_i \rangle^2\right)\left(\langle m_j^2 \rangle - \langle m_j \rangle^2\right)}}$, where m_i is the magnitude of the velocity vector of concave nanocube i, and concave nanocube *i* and *j* satisfy $r < \left|\mathbf{r}_i - \mathbf{r}_j\right| < r + \Delta r$.

Notes to Chapter 4

This chapter is adapted from the manuscript “Universal layer-by-layer growth mode in nanoparticle superlattices”, to be submitted.

CHAPTER 5: CONCLUSIONS AND FUTURE DIRECTIONS

Conclusions

With the combination of colloidal particle synthesis and direct imaging using optical microscopy and liquid-phase TEM, the relationship between colloidal particle building block and their self-assembly behaviors is being established experimentally, in real time and real space. We have discovered unconventional crystallization pathways from both the anisometric colloids and the nanoparticles. My studies not only fill in the gap of nanoparticle crystallization pathways and dynamic phase behaviors in solution, which has been missing for a long time due to technical limitations. They also provide experimental inputs to verify and guide computer simulations and serve as model systems for atomic phase dynamics. With the understanding of the dynamic colloidal assembly process, a better design and engineering of the colloidal particle assembly is achieved, which opens doors for fabricating functional materials with desired properties from the bottom-up.

The nanoparticles I synthesized have a lot of unique physical and chemical properties and are widely used in applications such as catalysis, display, surface-enhanced Raman spectroscopy (**Figure 5.1**), etc.[4] Their well-established surface chemistry enables readily accessible surface functionalization with hydrophobic/hydrophilic ligands, polymers, silica coating, with excellent compatibility with various solutions as functional additives.[4] Using abundant thermal energy at a greatly reduced energy cost, the self-assembled structures/materials have collective/coupled properties that cannot be achieved by individual particles,[4] with broad applications in filtration, drug delivery, coatings, etc. The self-assembled structures can also serve as material templates for further material processing, such as fabricating hierarchical/porous electrode materials for batteries. Mapping of the interparticle interactions and understanding of the energetic and kinetic contributions from direct imaging[5] enable reverse engineering of structure- and property-reconfigurable materials on demand, and metamaterials with novel properties not found in Nature (**Figure 5.1**).

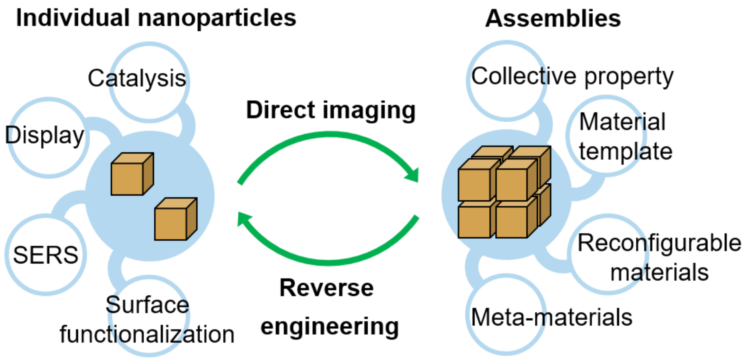

Figure 5.1. Broad applications of my research.

The liquid-phase TEM technique has tremendous advantages in directly imaging nanoscale solution-phase dynamics which previously have been experimentally inaccessible, such as nanomaterial growth and sintering, monitoring polymerization reactions and physical behaviors of polymers, mechanical transformation, and thin-film deposition.[49, 175] Its capabilities of flow, modulating temperature, electrical biasing, enable to study materials' *in situ* response to external stimuli such as pH, ionic concentration, shear flow, temperature, electrical biasing, at the nanoscale.

Future Directions

As discussed above, liquid-phase TEM is a powerful tool for probing the kinetics and energetics of NP self-assembly. However, many aspects remain to be examined, and we highlight a few below. First, more types of NPs need to be brought in for liquid-phase TEM self-assembly studies. While NPs with simple compositions, shapes, and kinetics have so far received the most attention, these particles are only a small subset of an ever-growing catalog of NP "elements".[4]

NPs can have diverse shapes, interior compositions, and surface ligand compositions. We foresee that synergy between NP synthesis and liquid-phase TEM studies will lead to exploration of how these features encode a broad range of interactions and functions. One can also extend beyond single-component NPs and investigate hybrid NPs and binary mixtures, pushing towards hierarchical interactions and multiplexed functions.

Second, we expect that crosstalk between liquid-phase TEM studies and statistical mechanics will mutually benefit both fields. Self-assembly studies will require statistical mechanical frameworks to translate new knowledge of fundamental interactions, fluctuations, and motions at the nanoscale into free energy landscapes, phase behavior, and the self-assembly design rules needed to optimize architecture-dependent properties and applications. Liquid-phase TEM studies will reciprocate by providing quantitative measurements of nanoscale interactions and motions that have, until recently, been an experimental and theoretical challenge.

Third, we see great potential in developing multimodal imaging techniques for studying nanoscale self-assembly dynamics, by interfacing liquid-phase TEM with methods such as element/oxidative states mapping (electron energy loss spectroscopy, energy-dispersive X-ray spectroscopy), 3D structural elucidation (tomography, diffraction), and optical microscopy. In this way, the understanding obtained will span length scales seamlessly, from atomic and single-NP levels all the way to the microscale.

Fourth, recent breakthroughs in active micron-scale colloids driven by external energy have demonstrated foundationally new self-organization and phase behaviors depending on steady-state, not thermodynamic equilibrium;[24-28] we see great promise in designing and imaging nanoscale active matter, where NPs fluctuate spatiotemporally under chemical or electrical cues and stabilize in time-varying patterns. This strategy to arrange NPs may lead to structures much more closely resembling living systems, which are often out of equilibrium.

Last but not least, we expect more experiments will eventually develop a quantitative understanding of general electron beam effects (e.g. radiolysis, ligand chemistry, NP diffusion, NP-substrate interactions), enabling direct knowledge transfer from liquid-phase TEM to conditions outside, for practical applications. In sum, new NP systems, advanced particle tracking algorithms, ultra-fast and ultra-sensitive detectors, new understanding of beam effects, and new theories for nanoscale interactions can all iteratively benefit studies on NP self-assemblies.

Notes to Chapter 5

Part of this chapter is adapted from the paper "Luo, B., Smith, J.W., Ou, Z. & Chen, Q. Quantifying the self-assembly behavior of anisotropic nanoparticles using liquid-phase transmission electron microscopy. *Acc. Chem. Res.* **50**, 1125-1133 (2017)",[5] Copyright © 2017, American Chemical Society.

REFERENCES

1. Glotzer, S.C. & Solomon, M.J. Anisotropy of building blocks and their assembly into complex structures. *Nat. Mater.* **6**, 557-562 (2007).
2. Li, B., Zhou, D. & Han, Y. Assembly and phase transitions of colloidal crystals. *Nat. Rev. Mater.* **1**, 15011 (2016).
3. Damasceno, P.F., Engel, M. & Glotzer, S.C. Predictive self-assembly of polyhedra into complex structures. *Science* **337**, 453-457 (2012).
4. Boles, M.A., Engel, M. & Talapin, D.V. Self-assembly of colloidal nanocrystals: From intricate structures to functional materials. *Chem. Rev.* **116**, 11220-11289 (2016).
5. Luo, B., Smith, J.W., Ou, Z. & Chen, Q. Quantifying the self-assembly behavior of anisotropic nanoparticles using liquid-phase transmission electron microscopy. *Acc. Chem. Res.* **50**, 1125-1133 (2017).
6. Bishop, K.J.M., Wilmer, C.E., Soh, S. & Grzybowski, B.A. Nanoscale forces and their uses in self-assembly. *Small* **5**, 1600-1630 (2009).
7. Min, Y., Akbulut, M., Kristiansen, K., Golan, Y. & Israelachvili, J. The role of interparticle and external forces in nanoparticle assembly. *Nat. Mater.* **7**, 527-538 (2008).
8. Xia, Y., Xiong, Y., Lim, B. & Skrabalak, S.E. Shape-controlled synthesis of metal nanocrystals: Simple chemistry meets complex physics? *Angew. Chem., Int. Ed.* **48**, 60-103 (2009).
9. Daniel, M.-C. & Astruc, D. Gold nanoparticles: Assembly, supramolecular chemistry, quantum-size-related properties, and applications toward biology, catalysis, and nanotechnology. *Chem. Rev.* **104**, 293-346 (2004).
10. Zhao, K., Bruinsma, R. & Mason, T.G. Entropic crystal–crystal transitions of Brownian squares. *Proc. Natl. Acad. Sci. U. S. A.* **108**, 2684-2687 (2011).
11. Silvera Batista, C.A., Larson, R.G. & Kotov, N.A. Nonadditivity of nanoparticle interactions. *Science* **350**, 1242477 (2015).
12. Cheng, W. et al. Probing in real time the soft crystallization of DNA-capped nanoparticles. *Angew. Chem., Int. Ed.* **49**, 380-384 (2010).
13. Young, K.L. et al. Assembly of reconfigurable one-dimensional colloidal superlattices due to a synergy of fundamental nanoscale forces. *Proc. Natl. Acad. Sci. U. S. A.* **109**, 2240-2245 (2012).
14. Durand, A., Papai, G. & Schultz, P. Structure, assembly and dynamics of macromolecular complexes by single particle cryo-electron microscopy. *J. Nanobiotechnol.* **11**, S4 (2013).
15. Frank, J. Story in a sample – the potential (and limitations) of cryo-electron microscopy applied to molecular machines. *Biopolymers* **99**, 832-836 (2013).
16. Sinkovits, D.W. & Luijten, E. Nanoparticle-controlled aggregation of colloidal tetrapods. *Nano Lett.* **12**, 1743-1748 (2012).
17. Park, J. et al. Direct observation of nanoparticle superlattice formation by using liquid cell transmission electron microscopy. *ACS Nano* **6**, 2078-2085 (2012).
18. Liu, Y., Lin, X.-M., Sun, Y. & Rajh, T. In situ visualization of self-assembly of charged gold nanoparticles. *J. Am. Chem. Soc.* **135**, 3764-3767 (2013).
19. Woehl, T.J. & Prozorov, T. The mechanisms for nanoparticle surface diffusion and chain self-assembly determined from real-time nanoscale kinetics in liquid. *J. Phys. Chem. C* **119**, 21261-21269 (2015).

20. Powers, A.S. et al. Tracking nanoparticle diffusion and interaction during self-assembly in a liquid cell. *Nano Lett.* **17**, 15-20 (2017).
21. Keskin, S. et al. Visualization of multimerization and self-assembly of DNA-functionalized gold nanoparticles using in-liquid transmission electron microscopy. *J. Phys. Chem. Lett.* **6**, 4487-4492 (2015).
22. Lin, G., Chee, S.W., Raj, S., Král, P. & Mirsaidov, U. Linker-mediated self-assembly dynamics of charged nanoparticles. *ACS Nano* **10**, 7443-7450 (2016).
23. van Anders, G., Klotsa, D., Ahmed, N.K., Engel, M. & Glotzer, S.C. Understanding shape entropy through local dense packing. *Proc. Natl. Acad. Sci. U. S. A.* **111**, E4812-E4821 (2014).
24. Bechinger, C. et al. Active particles in complex and crowded environments. *Rev. Mod. Phys.* **88**, 045006 (2016).
25. Marchetti, M.C. et al. Hydrodynamics of soft active matter. *Rev. Mod. Phys.* **85**, 1143-1189 (2013).
26. Yan, J. et al. Reconfiguring active particles by electrostatic imbalance. *Nat. Mater.* **15**, 1095-1099 (2016).
27. Ebbens, S.J. & Howse, J.R. In pursuit of propulsion at the nanoscale. *Soft Matter* **6**, 726-738 (2010).
28. Ramaswamy, S. The mechanics and statistics of active matter. *Annu. Rev. Condens. Matter Phys.* **1**, 323-345 (2010).
29. Lee, W.C., Kim, B.H., Choi, S., Takeuchi, S. & Park, J. Liquid cell electron microscopy of nanoparticle self-assembly driven by solvent drying. *J. Phys. Chem. Lett.* **8**, 647-654 (2017).
30. Kim, J., Jones, M.R., Ou, Z. & Chen, Q. In situ electron microscopy imaging and quantitative structural modulation of nanoparticle superlattices. *ACS Nano* **10**, 9801-9808 (2016).
31. Chen, Q. et al. Interaction potentials of anisotropic nanocrystals from the trajectory sampling of particle motion using in situ liquid phase transmission electron microscopy. *ACS Cent. Sci.* **1**, 33-39 (2015).
32. Park, J. et al. 3D structure of individual nanocrystals in solution by electron microscopy. *Science* **349**, 290-295 (2015).
33. Verch, A., Pfaff, M. & de Jonge, N. Exceptionally slow movement of gold nanoparticles at a solid/liquid interface investigated by scanning transmission electron microscopy. *Langmuir* **31**, 6956-6964 (2015).
34. Chen, Q. et al. 3D motion of DNA-Au nanoconjugates in graphene liquid cell electron microscopy. *Nano Lett.* **13**, 4556-4561 (2013).
35. Sun, Y. & Xia, Y. Shape-controlled synthesis of gold and silver nanoparticles. *Science* **298**, 2176-2179 (2002).
36. van Anders, G., Ahmed, N.K., Smith, R., Engel, M. & Glotzer, S.C. Entropically patchy particles: Engineering valence through shape entropy. *ACS Nano* **8**, 931-940 (2014).
37. Choueiri, R.M. et al. Surface patterning of nanoparticles with polymer patches. *Nature* **538**, 79-83 (2016).
38. Choi, J.J. et al. Controlling nanocrystal superlattice symmetry and shape-anisotropic interactions through variable ligand surface coverage. *J. Am. Chem. Soc.* **133**, 3131-3138 (2011).

39. Walker, D.A., Leitsch, E.K., Nap, R.J., Szleifer, I. & Grzybowski, B.A. Geometric curvature controls the chemical patchiness and self-assembly of nanoparticles. *Nat. Nanotechnol.* **8**, 676-681 (2013).
40. Vignaud, T., Blanchoin, L. & Théry, M. Directed cytoskeleton self-organization. *Trends Cell Biol.* **22**, 671-682 (2012).
41. Sutter, E. et al. In situ microscopy of the self-assembly of branched nanocrystals in solution. *Nat. Commun.* **7**, 11213 (2016).
42. Ye, X., Zheng, C., Chen, J., Gao, Y. & Murray, C.B. Using binary surfactant mixtures to simultaneously improve the dimensional tunability and monodispersity in the seeded growth of gold nanorods. *Nano Lett.* **13**, 765-771 (2013).
43. Tan, S.F., Anand, U. & Mirsaidov, U. Interactions and attachment pathways between functionalized gold nanorods. *ACS Nano* **11**, 1633-1640 (2017).
44. Grunbaum, B. & Shephard, G.C. in Tilings and Patterns, Edn. 2nd 1-14 (W. H. Freeman, New York; 2016).
45. Haji-Akbari, A. et al. Disordered, quasicrystalline and crystalline phases of densely packed tetrahedra. *Nature* **462**, 773-777 (2009).
46. O'Brien, M.N., Jones, M.R., Brown, K.A. & Mirkin, C.A. Universal noble metal nanoparticle seeds realized through iterative reductive growth and oxidative dissolution reactions. *J. Am. Chem. Soc.* **136**, 7603-7606 (2014).
47. Zhang, Q., Hu, Y., Guo, S., Goebl, J. & Yin, Y. Seeded growth of uniform Ag nanoplates with high aspect ratio and widely tunable surface plasmon bands. *Nano Lett.* **10**, 5037-5042 (2010).
48. Kim, J. et al. Reconfigurable polymer shells on shape-anisotropic gold nanoparticle cores. *Macromol. Rapid Commun.* **39**, 1800101 (2018).
49. Liao, H.-G. & Zheng, H. Liquid cell transmission electron microscopy. *Annu. Rev. Phys. Chem.* **67**, 719-747 (2016).
50. Luo, B. et al. Hierarchical self-assembly of 3D lattices from polydisperse anisometric colloids. *Nat. Commun.* **10**, 1815 (2019).
51. Luo, B. et al. Polymerization-like co-assembly of silver nanoplates and patchy spheres. *ACS Nano* **11**, 7626-7633 (2017).
52. McManus, J.J., Charbonneau, P., Zaccarelli, E. & Asherie, N. The physics of protein self-assembly. *Curr. Opin. Colloid Interface Sci.* **22**, 73-79 (2016).
53. Li, W. et al. Strings and stripes formed by a protein system interacting via a single-patch attraction. *Soft Matter* **12**, 9330-9333 (2016).
54. Lomakin, A., Asherie, N. & Benedek, G.B. Aeolotopic interactions of globular proteins. *Proc. Natl. Acad. Sci. U. S. A.* **96**, 9465-9468 (1999).
55. Nogales, E., Whittaker, M., Milligan, R.A. & Downing, K.H. High-resolution model of the microtubule. *Cell* **96**, 79-88 (1999).
56. Ju, G. et al. Coherent X-ray spectroscopy reveals the persistence of island arrangements during layer-by-layer growth. *Nat. Phys.* **15**, 589-594 (2019).
57. Tersoff, J., Denier van der Gon, A.W. & Tromp, R.M. Critical island size for layer-by-layer growth. *Phys. Rev. Lett.* **72**, 266-269 (1994).
58. Rashkovich, L.N., De Yoreo, J.J., Orme, C.A. & Chernov, A.A. In situ atomic force microscopy of layer-by-layer crystal growth and key growth concepts. *Crystallogr. Rep.* **51**, 1063-1074 (2006).

59. Kunkel, R., Poelsema, B., Verheij, L.K. & Comsa, G. Reentrant layer-by-layer growth during molecular-beam epitaxy of metal-on-metal substrates. *Phys. Rev. Lett.* **65**, 733-736 (1990).
60. Voronkov, V.V. in Growth of Crystals: Volume 10. (ed. N.N. Sheftal') 1-17 (Springer US, Boston, MA; 1976).
61. Buehler, M.J. Nature designs tough collagen: Explaining the nanostructure of collagen fibrils. *Proc. Natl. Acad. Sci. U. S. A.* **103**, 12285-12290 (2006).
62. Minary-Jolandan, M. & Yu, M.-F. Nanomechanical heterogeneity in the gap and overlap regions of type I collagen fibrils with implications for bone heterogeneity. *Biomacromolecules* **10**, 2565-2570 (2009).
63. Bornhoeft, L.R. et al. Teslaphoresis of carbon nanotubes. *ACS Nano* **10**, 4873-4881 (2016).
64. Fan, S. et al. Self-oriented regular arrays of carbon nanotubes and their field emission properties. *Science* **283**, 512-514 (1999).
65. Yu, M.-F. et al. Strength and breaking mechanism of multiwalled carbon nanotubes under tensile load. *Science* **287**, 637-640 (2000).
66. Zhang, Y. et al. Self-assembly of ultrathin gold nanowires and single walled carbon nanotubes as a highly sensitive substrate for surface enhanced Raman spectroscopy. *New J. Chem.* **40**, 7286-7289 (2016).
67. Chen, Y. et al. Assembly of ultrathin gold nanowires: From polymer analogue to colloidal block. *ACS Nano* **11**, 2756-2763 (2017).
68. He, Y., Chen, Y., Xu, Q., Xu, J. & Weng, J. Assembly of ultrathin gold nanowires into honeycomb macroporous pattern films with high transparency and conductivity. *ACS Appl. Mater. Interfaces* **9**, 7826-7833 (2017).
69. Li, B. et al. Stress-induced phase transformation and optical coupling of silver nanoparticle superlattices into mechanically stable nanowires. *Nat. Commun.* **5**, 4179 (2014).
70. Gao, B., Rozin, M.J. & Tao, A.R. Plasmonic Nanocomposites: Polymer-guided strategies for assembling metal nanoparticles. *Nanoscale* **5**, 5677-5691 (2013).
71. Vutukuri, H.R., Badaire, S., de Winter, D.A.M., Imhof, A. & van Blaaderen, A. Directed self-assembly of micron-sized gold nanoplatelets into oriented flexible stacks with tunable interplate distance. *Nano Lett.* **15**, 5617-5623 (2015).
72. Bai, F. et al. Pressure-tuned structure and property of optically active nanocrystals. *Adv. Mater.* **28**, 1989-1993 (2016).
73. Odian, G. in Principles of Polymerization, Edn. 4th 40-44 (John Wiley & Sons, Inc., Hoboken; 2004).
74. Byrom, J., Han, P., Savory, M. & Biswal, S.L. Directing assembly of DNA-coated colloids with magnetic fields to generate rigid, semiflexible, and flexible chains. *Langmuir* **30**, 9045-9052 (2014).
75. Li, D., Banon, S. & Biswal, S.L. Bending dynamics of DNA-linked colloidal particle chains. *Soft Matter* **6**, 4197-4204 (2010).
76. Wang, Y. et al. Patchy particle self-assembly via metal coordination. *J. Am. Chem. Soc.* **135**, 14064-14067 (2013).
77. Domínguez-García, P., Melle, S. & Rubio, M.A. Morphology of anisotropic chains in a magneto-rheological fluid during aggregation and disaggregation processes. *J. Colloid Interface Sci.* **333**, 221-229 (2009).

78. Furst, E.M. & Gast, A.P. Dynamics and lateral interactions of dipolar chains. *Phys. Rev. E* **62**, 6916-6925 (2000).
79. Silva, A.S., Bond, R., Plouraboué, F. & Wirtz, D. Fluctuation dynamics of a single magnetic chain. *Phys. Rev. E* **54**, 5502-5510 (1996).
80. Chen, Q. et al. Supracolloidal reaction kinetics of Janus spheres. *Science* **331**, 199-202 (2011).
81. Chen, Q. et al. Triblock colloids for directed self-assembly. *J. Am. Chem. Soc.* **133**, 7725-7727 (2011).
82. Demortière, A. et al. Self-assembled tunable networks of sticky colloidal particles. *Nat. Commun.* **5**, 3117 (2014).
83. Groschel, A.H. et al. Guided hierarchical co-assembly of soft patchy nanoparticles. *Nature* **503**, 247-251 (2013).
84. Kuroki, H. et al. Tunable ultrathin membranes with nonvolatile pore shape memory. *ACS Appl. Mater. Interfaces* **7**, 10401-10406 (2015).
85. Rybtchinski, B. Adaptive Supramolecular nanomaterials based on strong noncovalent interactions. *ACS Nano* **5**, 6791-6818 (2011).
86. Smith, A.M. et al. Quantitative analysis of thiolated ligand exchange on gold nanoparticles monitored by 1H NMR spectroscopy. *Anal. Chem.* **87**, 2771-2778 (2015).
87. Parsons, J.D. Nematic ordering in a system of rods. *Phys. Rev. A* **19**, 1225-1230 (1979).
88. Usov, I. & Mezzenga, R. FiberApp: An open-source software for tracking and analyzing polymers, filaments, biomacromolecules, and fibrous objects. *Macromolecules* **48**, 1269-1280 (2015).
89. Tigges, T. & Walther, A. Hierarchical self-assembly of 3D-printed lock-and-key colloids through shape recognition. *Angew. Chem., Int. Ed.* **55**, 11261-11265 (2016).
90. Liu, K. et al. Step-growth polymerization of inorganic nanoparticles. *Science* **329**, 197-200 (2010).
91. Israelachvili, J.N. Intermolecular and Surface Forces. (Academic press, 2011).
92. Sacanna, S., Irvine, W.T.M., Chaikin, P.M. & Pine, D.J. Lock and key colloids. *Nature* **464**, 575-578 (2010).
93. Klinkova, A., Thérien-Aubin, H., Choueiri, R.M., Rubinstein, M. & Kumacheva, E. Colloidal analogs of molecular chain stoppers. *Proc. Natl. Acad. Sci. U. S. A.* **110**, 18775-18779 (2013).
94. Rosen, D.A. & Tao, A.R. Modeling the optical properties of bowtie antenna generated by self-assembled Ag triangular nanoprisms. *ACS Appl. Mater. Interfaces* **6**, 4134-4142 (2014).
95. Liu, K. et al. In situ plasmonic counter for polymerization of chains of gold nanorods in solution. *ACS Nano* **7**, 5901-5910 (2013).
96. Lee, S., Lee, J., Hwang, S.H., Yun, J. & Jang, J. Enhanced electroresponsive performance of double-shell SiO_2/TiO_2 hollow nanoparticles. *ACS Nano* **9**, 4939-4949 (2015).
97. Schwarz, G., Maisch, S., Ullrich, S., Wagenhöfer, J. & Kurth, D.G. Electrorheological fluids based on metallo-supramolecular polyelectrolyte–silicate composites. *ACS Appl. Mater. Interfaces* **5**, 4031-4034 (2013).
98. Cheng, Y. et al. Facile approach to large-scale synthesis of 1D calcium and titanium precipitate (CTP) with high electrorheological activity. *ACS Appl. Mater. Interfaces* **2**, 621-625 (2010).

99. Carlson, J.D. & Jolly, M.R. MR fluid, foam and elastomer devices. *Mechatronics* **10**, 555-569 (2000).
100. Jolly, M.R., Bender, J.W. & Carlson, J.D. Properties and applications of commercial magnetorheological fluids. *J. Intell. Mater. Syst. Struct.* **10**, 5-13 (1999).
101. Mao, X., Chen, Q. & Granick, S. Entropy favours open colloidal lattices. *Nat. Mater.* **12**, 217-222 (2013).
102. Winder, S.J. & Ayscough, K.R. Actin-binding proteins. *J. Cell Sci.* **118**, 651-654 (2005).
103. Delandre, C., Amikura, R. & Moore, A.W. Microtubule nucleation and organization in dendrites. *Cell Cycle* **15**, 1685-1692 (2016).
104. Wiese, C. & Zheng, Y. Microtubule nucleation: γ-tubulin and beyond. *J. Cell Sci.* **119**, 4143-4153 (2006).
105. Jorgenson, T.D., Mohammed, A.M., Agrawal, D.K. & Schulman, R. Self-assembly of hierarchical DNA nanotube architectures with well-defined geometries. *ACS Nano* **11**, 1927-1936 (2017).
106. Chakrabarty, R., Mukherjee, P.S. & Stang, P.J. Supramolecular coordination: Self-assembly of finite two- and three-dimensional ensembles. *Chem. Rev.* **111**, 6810-6918 (2011).
107. Mohammed, A.M. et al. Self-assembly of precisely defined DNA nanotube superstructures using DNA origami seeds. *Nanoscale* **9**, 522-526 (2017).
108. Morrow, J.S. et al. in Comprehensive Physiology (John Wiley & Sons, Inc., 2010).
109. Albers, S.-V. & Meyer, B.H. The archaeal cell envelope. *Nat. Rev. Microbiol.* **9**, 414-426 (2011).
110. Schnablegger, H. & Singh, Y. The SAXS Guide. *The SAXS Guide, 3rd Ed.* **Anton Paar GmbH**, pp 25-26 (2013).
111. Liu, J.-W., Liang, H.-W. & Yu, S.-H. Macroscopic-scale assembled nanowire thin films and their functionalities. *Chem. Rev.* **112**, 4770-4799 (2012).
112. Schmidt, V., Wittemann Joerg, V., Senz, S. & Gösele, U. Silicon nanowires: A review on aspects of their growth and their electrical properties. *Adv. Mater.* **21**, 2681-2702 (2009).
113. Vold, M.J. Van der Waals' attraction between anisometric particles. *J. Colloid Sci.* **9**, 451-459 (1954).
114. Gudiksen, M.S., Lauhon, L.J., Wang, J., Smith, D.C. & Lieber, C.M. Growth of nanowire superlattice structures for nanoscale photonics and electronics. *Nature* **415**, 617-620 (2002).
115. Li, D. et al. Thermal conductivity of individual silicon nanowires. *Appl. Phys. Lett.* **83**, 2934-2936 (2003).
116. Hsiao, L.C. et al. Metastable orientational order of colloidal discoids. *Nat. Commun.* **6**, 8507 (2015).
117. Liu, B. et al. Switching plastic crystals of colloidal rods with electric fields. *Nat. Commun.* **5**, 3092 (2014).
118. Meijer, J.-M. et al. Observation of solid–solid transitions in 3D crystals of colloidal superballs. *Nat. Commun.* **8**, 14352 (2017).
119. Gong, Z., Hueckel, T., Yi, G.-R. & Sacanna, S. Patchy particles made by colloidal fusion. *Nature* **550**, 234-238 (2017).
120. Macfarlane, R.J. et al. Assembly and organization processes in DNA-directed colloidal crystallization. *Proc. Natl. Acad. Sci. U. S. A.* **106**, 10493-10498 (2009).

121. Li, B. et al. Superfast assembly and synthesis of gold nanostructures using nanosecond low-temperature compression via magnetic pulsed power. *Nat. Commun.* **8**, 14778 (2017).
122. Chen, W. et al. Large-area nanoimprinted colloidal Au nanocrystal-based nanoantennas for ultrathin polarizing plasmonic metasurfaces. *Nano Lett.* **15**, 5254-5260 (2015).
123. Rossi, L. et al. Cubic crystals from cubic colloids. *Soft Matter* **7**, 4139-4142 (2011).
124. Trau, M., Saville, D.A. & Aksay, I.A. Field-induced layering of colloidal crystals. *Science* **272**, 706-709 (1996).
125. van der Kooij, F.M. & Lekkerkerker, H.N.W. Liquid-crystal phase transitions in suspensions of plate-like particles. *Philos. Trans. R. Soc., A* **359**, 985-995 (2001).
126. van der Kooij, F.M., Kassapidou, K. & Lekkerkerker, H.N.W. Liquid crystal phase transitions in suspensions of polydisperse plate-like particles. *Nature* **406**, 868-871 (2000).
127. Brown, A.B.D., Ferrero, C., Narayanan, T. & Rennie, A.R. Phase separation and structure in a concentrated colloidal dispersion of uniform plates. *Eur. Phys. J. B* **11**, 481-489 (1999).
128. Petukhov, A.V. et al. Observation of a hexatic columnar liquid crystal of polydisperse colloidal disks. *Phys. Rev. Lett.* **95**, 077801 (2005).
129. Saunders, A.E., Ghezelbash, A., Smilgies, D.-M., Sigman, M.B. & Korgel, B.A. Columnar self-assembly of colloidal nanodisks. *Nano Lett.* **6**, 2959-2963 (2006).
130. Zhang, H.-T., Wu, G. & Chen, X.-H. Large-scale synthesis and self-assembly of monodisperse hexagon Cu_2S nanoplates. *Langmuir* **21**, 4281-4282 (2005).
131. Dong, A., Chen, J., Vora, P.M., Kikkawa, J.M. & Murray, C.B. Binary nanocrystal superlattice membranes self-assembled at the liquid–air interface. *Nature* **466**, 474-477 (2010).
132. Singh, G. et al. Self-assembly of magnetite nanocubes into helical superstructures. *Science* **345**, 1149-1153 (2014).
133. Tan, S.F., Chee, S.W., Lin, G. & Mirsaidov, U. Direct observation of interactions between nanoparticles and nanoparticle self-assembly in solution. *Acc. Chem. Res.* **50**, 1303-1312 (2017).
134. Yaghi, O.M. et al. Reticular synthesis and the design of new materials. *Nature* **423**, 705-714 (2003).
135. Lofton, C. & Sigmund, W. Mechanisms controlling crystal habits of gold and silver colloids. *Adv. Funct. Mater.* **15**, 1197-1208 (2005).
136. Raşa, M. & Philipse, A.P. Evidence for a macroscopic electric field in the sedimentation profiles of charged colloids. *Nature* **429**, 857-860 (2004).
137. Kim, J., Ou, Z., Jones, M.R., Song, X. & Chen, Q. Imaging the polymerization of multivalent nanoparticles in solution. *Nat. Commun.* **8**, 761 (2017).
138. Gregory, J. Approximate expressions for retarded van der waals interaction. *J. Colloid Interface Sci.* **83**, 138-145 (1981).
139. Hwang, J., Kim, J. & Sung, B.J. Dynamics of highly polydisperse colloidal suspensions as a model system for bacterial cytoplasm. *Phys. Rev. E* **94**, 022614 (2016).
140. Xia, Y. et al. Self-assembly of self-limiting monodisperse supraparticles from polydisperse nanoparticles. *Nat. Nanotechnol.* **6**, 580-587 (2011).
141. Fraser, D.P., Zuckermann, M.J. & Mouritsen, O.G. Simulation technique for hard-disk models in two dimensions. *Phys. Rev. A* **42**, 3186-3195 (1990).

142. Zhang, T.H. & Liu, X.Y. How does a transient amorphous precursor template crystallization. *J. Am. Chem. Soc.* **129**, 13520-13526 (2007).
143. Gasser, U., Weeks, E.R., Schofield, A., Pusey, P.N. & Weitz, D.A. Real-space imaging of nucleation and growth in colloidal crystallization. *Science* **292**, 258-262 (2001).
144. Cantini, E. et al. Electrically responsive surfaces: Experimental and theoretical investigations. *Acc. Chem. Res.* **49**, 1223-1231 (2016).
145. Tan, L.H. et al. Mechanistic insight into DNA-guided control of nanoparticle morphologies. *J. Am. Chem. Soc.* **137**, 14456-14464 (2015).
146. Liu, N., Hentschel, M., Weiss, T., Alivisatos, A.P. & Giessen, H. Three-dimensional plasmon rulers. *Science* **332**, 1407-1410 (2011).
147. Agarwal, U. & Escobedo, F.A. Mesophase behaviour of polyhedral particles. *Nat. Mater.* **10**, 230-235 (2011).
148. Veerman, J.A.C. & Frenkel, D. Phase behavior of disklike hard-core mesogens. *Phys. Rev. A* **45**, 5632-5648 (1992).
149. Zhang, S.-D., Reynolds, P.A. & van Duijneveldt, J.S. Phase behavior of mixtures of colloidal platelets and nonadsorbing polymers. *J. Chem. Phys.* **117**, 9947-9958 (2002).
150. Sato, K., Itoh, Y. & Aida, T. Columnarly assembled liquid-crystalline peptidic macrocycles unidirectionally orientable over a large area by an electric field. *J. Am. Chem. Soc.* **133**, 13767-13769 (2011).
151. Koo, B.T., Dichtel, W.R. & Clancy, P. A classification scheme for the stacking of two-dimensional boronate ester-linked covalent organic frameworks. *J. Mater. Chem.* **22**, 17460-17469 (2012).
152. Balagurusamy, V.S.K. et al. Quasi-one dimensional electrical conductivity and thermoelectric power studies on a discotic liquid crystal. *Pramana* **53**, 3-11 (1999).
153. Parsegian, V.A. & Weiss, G.H. Spectroscopic parameters for computation of van der waals forces. *J. Colloid Interface Sci.* **81**, 285-289 (1981).
154. van Tassel, J. & Randall, C.A. Potential for integration of electrophoretic deposition into electronic device manufacture; demonstrations using silver/palladium. *J. Mater. Sci.* **39**, 867-879 (2004).
155. Anandarajah, A. & Chen, J. Single correction function for computing retarded van der Waals attraction. *J. Colloid Interface Sci.* **176**, 293-300 (1995).
156. Grahame, D.C. The electrical double layer and the theory of electrocapillarity. *Chem. Rev.* **41**, 441-501 (1947).
157. Sander, R. Compilation of Henry's law constants (version 4.0) for water as solvent. *Atmos. Chem. Phys.* **15**, 4399-4981 (2015).
158. Parsegian, V.A. Van der Waals Forces: A Handbook for Biologists, Chemists, Engineers, and Physicists. (Cambridge University Press, 2005).
159. Hara, R., Fukuoka, T., Takahashi, R., Utsumi, Y. & Yamaguchi, A. Surface-enhanced Raman spectroscopy using a coffee-ring-type three-dimensional silver nanostructure. *RSC Adv.* **5**, 1378-1384 (2015).
160. Frenkel, D. & Smit, B. Understanding Molecular Simulation: From Algorithms to Applications, Vol. 1. (Academic press, 2001).
161. Zhang, Z. & Lagally, M.G. Atomistic processes in the early stages of thin-film growth. *Science* **276**, 377-383 (1997).
162. Goodman, C.H.L. Crystal Growth. (Springer, 1974).

163. Li, D. et al. Direction-specific interactions control crystal growth by oriented attachment. *Science* **336**, 1014-1018 (2012).
164. Einstein, T.L. & Stasevich, T.J. Epitaxial growth writ large. *Science* **327**, 423-424 (2010).
165. Liao, H.-G. et al. Facet development during platinum nanocube growth. *Science* **345**, 916-919 (2014).
166. De Yoreo, J.J. & Vekilov, P.G. Principles of crystal nucleation and growth. *Rev. Mineral. Geochem.* **54**, 57-93 (2003).
167. Ganapathy, R., Buckley, M.R., Gerbode, S.J. & Cohen, I. Direct measurements of island growth and step-edge barriers in colloidal epitaxy. *Science* **327**, 445-448 (2010).
168. Heijna, M.C.R., Enckevort, W.J.P.v. & Vlieg, E. Growth inhibition of protein crystals: A study of lysozyme polymorphs. *Cryst. Growth Des.* **8**, 270-274 (2008).
169. Liu, Y., Wang, X. & Ching, C.B. Toward further understanding of lysozyme crystallization: Phase diagram, protein−protein interaction, nucleation kinetics, and growth kinetics. *Cryst. Growth Des.* **10**, 548-558 (2010).
170. Kleppmann, N., Schreiber, F. & Klapp, S.H.L. Limits of size scalability of diffusion and growth: Atoms versus molecules versus colloids. *Phys. Rev. E* **95**, 020801 (2017).
171. Brune, H. Microscopic view of epitaxial metal growth: Nucleation and aggregation. *Surf. Sci. Rep.* **31**, 125-229 (1998).
172. Xie, R. & Liu, X.-Y. Controllable epitaxial crystallization and reversible oriented patterning of two-dimensional colloidal crystals. *J. Am. Chem. Soc.* **131**, 4976-4982 (2009).
173. Aarts, D.G.A.L., Schmidt, M. & Lekkerkerker, H.N.W. Direct visual observation of thermal capillary waves. *Science* **304**, 847-850 (2004).
174. Ou, Z., Wang, Z., Luo, B., Luijten, E. & Chen, Q. Kinetic pathways of crystallization at the nanoscale. *Nat. Mater.* (2019).
175. Ross, F.M. Opportunities and challenges in liquid cell electron microscopy. *Science* **350**, aaa9886 (2015).
176. Kim, J. et al. Polymorphic assembly from beveled gold triangular nanoprisms. *Nano. Lett.* **17**, 3270-3275 (2017).
177. Lin, H. et al. Clathrate colloidal crystals. *Science* **355**, 931-935 (2017).
178. Hwang, H., Weitz, D.A. & Spaepen, F. Direct observation of crystallization and melting with colloids. *Proc. Natl. Acad. Sci. U. S. A.* **116**, 1180-1184 (2019).
179. Zhang, J. et al. Concave cubic gold nanocrystals with high-index facets. *J. Am. Chem. Soc.* **132**, 14012-14014 (2010).
180. Zhang, Z., Detch, J. & Metiu, H. Surface roughness in thin-film growth: The effect of mass transport between layers. *Phys. Rev. B* **48**, 4972-4975 (1993).
181. Auyeung, E. et al. DNA-mediated nanoparticle crystallization into Wulff polyhedra. *Nature* **505**, 73-77 (2013).
182. Seo, S.E., Girard, M., Olvera de la Cruz, M. & Mirkin, C.A. Non-equilibrium anisotropic colloidal single crystal growth with DNA. *Nat. Commun.* **9**, 4558 (2018).
183. Seo, S.E., Girard, M., de la Cruz, M.O. & Mirkin, C.A. The importance of salt-enhanced electrostatic repulsion in colloidal crystal engineering with DNA. *ACS Cent. Sci.* **5**, 186-191 (2019).
184. Harmand, J.-C. et al. Atomic step flow on a nanofacet. *Phys. Rev. Lett.* **121**, 166101 (2018).

185. Nikoobakht, B. & El-Sayed, M.A. Preparation and growth mechanism of gold nanorods (NRs) using seed-mediated growth method. *Chem. Mater.* **15**, 1957-1962 (2003).
186. Ramos, L., Lubensky, T.C., Dan, N., Nelson, P. & Weitz, D.A. Surfactant-mediated two-dimensional crystallization of colloidal crystals. *Science* **286**, 2325-2328 (1999).
187. Rubinstein, M. & Colby, R.H. Polymer Physics, Vol. 23. (Oxford university press New York, 2003).
188. Schneider, N.M. et al. Electron–water interactions and implications for liquid cell electron microscopy. *J. Phys. Chem. C* **118**, 22373-22382 (2014).
189. Crocker, J.C. & Grier, D.G. Methods of digital video microscopy for colloidal studies. *J. Colloid. Interface Sci.* **179**, 298-310 (1996).
190. Huner, B. & Hussey, R.G. Cylinder drag at low Reynolds number. *Phys. Fluids* **20**, 1211-1218 (1977).